APOGEE Chemical Abundance Patterns of the Massive Milky Way Satellites

Sten Hasselquist[1,38], Christian R. Hayes[2], Jianhui Lian[1], David H. Weinberg[3,4], Gail Zasowski[1], Danny Horta[5], Rachael Beaton[6], Diane K. Feuillet[7], Elisa R. Garro[8], Carme Gallart[9,10], Verne V. Smith[11], Jon A. Holtzman[12], Dante Minniti[8,13], Ivan Lacerna[14,15], Matthew Shetrone[16], Henrik Jönsson[17], Maria-Rosa L. Cioni[18], Sean P. Fillingham[2], Katia Cunha[19,20], Robert O'Connell[21], José G. Fernández-Trincado[22,14], Ricardo R. Muñoz[23], Ricardo Schiavon[5], Andres Almeida[24], Borja Anguiano[21], Timothy C. Beers[25], Dmitry Bizyaev[26,27], Joel R. Brownstein[1], Roger E. Cohen[28], Peter Frinchaboy[29], D. A. García-Hernández[9,10], Doug Geisler[30,24,31], Richard R. Lane[32,22], Steven R. Majewski[21], David L. Nidever[33], Christian Nitschelm[34], Joshua Povick[33], Adrian Price-Whelan[35], Alexandre Roman-Lopes[31,16], Margarita Rosado[36], Jennifer Sobeck[2], Guy Stringfellow[37], Octavio Valenzuela[36], Sandro Villanova[30], and Fiorenzo Vincenzo[3]

[1] Department of Physics & Astronomy, University of Utah, Salt Lake City, UT 84112, USA; stenhasselquist@astro.utah.edu
[2] Department of Astronomy, University of Washington, Seattle, WA 98195, USA
[3] Department of Astronomy, The Ohio State University, 140 W. 18th Ave., Columbus, OH 43210, USA
[4] Department of Astronomy and Center for Cosmology and AstroParticle Physics, The Ohio State University, 140 W. 18th Ave, Columbus, OH 43210, USA
[5] Astrophysics Research Institute, Liverpool John Moores University, IC2, Liverpool Science Park, 146 Brownlow Hill, Liverpool L3 5RF, UK
[6] Department of Astrophysical Sciences, Princeton University, 4 Ivy Lane, Princeton, NJ 08544, USA
[7] Lund Observatory, Department of Astronomy and Theoretical Physics, Box 43, SE-221 00 Lund, Sweden
[8] Departamento de Ciencias Físicas, Facultad de Ciencias Exactas, Universidad Andres Bello, Fernández Concha 700, Las Condes, Santiago, Chile
[9] Instituto de Astrofísica de Canarias (IAC), E-38205 La Laguna, Tenerife, Spain
[10] Universidad de La Laguna (ULL), Departamento de Astrofísica, E-38206 La Laguna, Tenerife, Spain
[11] National Optical Astronomy Observatory, 950 North Cherry Ave, Tucson, AZ 85719, USA
[12] Department of Astronomy, New Mexico State University, Las Cruces, NM 88003, USA
[13] Vatican Observatory, Vatican City State, V-00120, Italy
[14] Instituto de Astronomía y Ciencias Planetarias, Universidad de Atacama, Copayapu 485, Copiapó, Chile
[15] Millennium Institute of Astrophysics, Nuncio Monsenor Sotero Sanz 100, Of. 104, Providencia, Santiago, Chile
[16] Lick Observatory, USA
[17] Materials Science and Applied Mathematics, Malmö University, SE-205 06 Malmö, Sweden
[18] Leibniz-Institut für Astrophysik Potsdam, An der Sternwarte 16, D-14482 Potsdam, Germany
[19] Steward Observatory, The University of Arizona, Tucson, AZ 85719, USA
[20] Observatório Nacional, 20921-400 So Cristóvao, Rio de Janeiro, RJ, Brazil
[21] Department of Astronomy, University of Virginia, Charlottesville, VA 22904, USA
[22] Instituto de Astronomía, Universidad Católica del Norte, Av. Angamos 0610, Antofagasta, Chile
[23] Departamento de Astronomía, Universidad de Chile, Camino El Observatorio 1515, Las Condes, Santiago, Chile
[24] Instituto de Investigación Multidisciplinario en Ciencia y Tecnología, Universidad de La Serena, Avenida Raúl Bitrán S/N, La Serena, Chile
[25] Department of Physics and JINA Center for the Evolution of the Elements, University of Notre Dame, Notre Dame, IN 46556, USA
[26] Apache Point Observatory and New Mexico State University, Sunspot, NM 88349, USA
[27] Sternberg Astronomical Institute, Moscow State University, Moscow, 119992, Russia
[28] Space Telescope Science Institute, 3700 San Martin Drive, Baltimore, MD 21218, USA
[29] Department of Physics & Astronomy, Texas Christian University, Fort Worth, TX 76129, USA
[30] Departamento de Astronomía, Casilla 160-C, Universidad de Concepcion, Chile
[31] Departamento de Física y Astronomía, Facultad de Ciencias, Universidad de La Serena. Av. Juan Cisternas 1200, La Serena, Chile
[32] Centro de Investigación en Astronomía, Universidad Bernardo O'Higgins, Avenida Viel 1497, Santiago, Chile
[33] Department of Physics, Montana State University, P.O. Box 173840, Bozeman, MT 59717-3840, USA; dnidever@montana.edu
[34] Centro de Astronomía (CITEVA), Universidad de Antofagasta, Avenida Angamos 601, Antofagasta 1270300, Chile
[35] Center for Computational Astrophysics, Flatiron Institute, 162 5th Ave., New York, NY 10010, USA
[36] Instituto de Astronomía, Universidad Nacional Autónoma de México, A.P. 70-264, 04510, Mexico, D.F., Mexico
[37] Center for Astrophysics and Space Astronomy, Department of Astrophysical and Planetary Sciences, University of Colorado, Boulder, CO 80309

Abstract

The SDSS-IV Apache Point Observatory Galactic Evolution Experiment (APOGEE) survey has obtained high-resolution spectra for thousands of red giant stars distributed among the massive satellite galaxies of the Milky Way (MW): the Large and Small Magellanic Clouds (LMC/SMC), the Sagittarius Dwarf Galaxy (Sgr), Fornax (Fnx), and the now fully disrupted Gaia Sausage/Enceladus (GSE) system. We present and analyze the APOGEE chemical abundance patterns of each galaxy to draw robust conclusions about their star formation histories, by quantifying the relative abundance trends of multiple elements (C, N, O, Mg, Al, Si, Ca, Fe, Ni, and Ce), as well as by fitting chemical evolution models to the [α/Fe]–[Fe/H] abundance plane for each galaxy. Results show that the chemical signatures of the starburst in the Magellanic Clouds (MCs) observed by Nidever et al. in the α-element abundances extend to C+N, Al, and Ni, with the major burst in the SMC occurring some 3–4 Gyr before the burst in the LMC. We find that Sgr and Fnx also exhibit chemical abundance patterns suggestive of secondary star formation epochs, but these events were weaker and earlier (∼5–7 Gyr ago) than those observed in the MCs. There is no chemical evidence of a second starburst in GSE, but this galaxy shows the strongest initial star formation as compared to the other four galaxies. All dwarf galaxies had greater relative contributions of AGB stars to their

---

[38] NSF Astronomy and Astrophysics Postdoctoral Fellow.

enrichment than the MW. Comparing and contrasting these chemical patterns highlight the importance of galaxy environment on its chemical evolution.

Unified Astronomy Thesaurus concepts: Dwarf galaxies (416); Galaxies (573); Sagittarius dwarf spheroidal galaxy (1423); Large Magellanic Cloud (903); Magellanic Clouds (990); Small Magellanic Cloud (1468); Fornax dwarf spheroidal galaxy (548); Galaxy chemical evolution (580); Chemical enrichment (225); Chemical abundances (224); Abundance ratios (11); Galaxy abundances (574)

Supporting material: machine-readable table

1. Introduction

Galaxies are ubiquitous structures in the universe. While we have made tremendous strides in describing and understanding the patterns seen in galaxies on global or coarsely resolved scales (e.g., mass–metallicity relation, galaxy color–magnitude diagram), our understanding of how these patterns reflect finer details of formation and evolution is severely limited. This is largely due to the fact that only a few galaxies outside of our own Milky Way (MW) can be studied at the spatial resolution of individual stars, which is required to precisely analyze the galactic star formation histories (SFHs). Fortunately, the Local Group consists of three main massive galaxies (MW, M31, and M33) along with their vast populations of dwarf galaxies, which themselves span a large range in mass, morphology, and environment (e.g., Hodge 1971, 1989; Mateo 1998; Tolstoy et al. 2009; McConnachie 2012; Ibata et al. 2013; Weisz et al. 2014; Simon 2019). In principle, detailed SFHs built from photometric or even spectroscopic observations can be constructed for each of these galaxies, allowing for an understanding of the effects that halo mass, formation environment, and interaction history have on a galaxy's SFH.

In practice, the large distance to these galaxies combined with their often large angular size means that fully spatially resolved SFH studies remain observationally costly. Moreover, systematic differences between methods of determining SFHs can complicate comparisons across multiple galaxies. Weisz et al. (2014) performed an SFH analysis of 40 Local Group dwarf galaxies using photometry from the Hubble Space Telescope, deriving SFHs from the color–magnitude diagram (CMD). Although these data did consist of photometry of varying depths (see, e.g., Ruiz-Lara et al. 2018 for effects of photometric depth on SFH determination), the data were all analyzed in a uniform way, and the authors were able to draw reasonably robust conclusions on mass/environmental effects on galaxy evolution. In particular, they found that in comparison to the more massive galaxies, less massive dwarf galaxies generally formed a larger fraction of their stars in the first 2–3 Gyr of their existence.

The authors also found measurable scatter in SFHs at fixed mass, suggesting that where the galaxy formed in relation to other galaxies (i.e., its formation environment) likely has a strong effect on evolution (see Gallart et al. 2015). Many other works find similar SFH scatter at fixed mass (e.g., Mateo 1998; Grebel 1999), with some galaxies such as Carina experiencing distinct bursts (e.g., de Boer et al. 2014; Santana et al. 2016). Simulations have proven valuable for understanding exactly how environment affects SFH (e.g., Wetzel et al. 2016; Revaz & Jablonka 2018; Miyoshi & Chiba 2020), but the extent to which external effects dominate effects from a galaxy's intrinsic properties is still largely unknown (e.g., Kirby et al. 2011, 2013; Hendricks et al. 2014; Escala et al. 2018; Wheeler et al. 2019).

While photometric studies have done much to characterize the star formation rate of Local Group galaxies as a function of time, additional details can be probed with spectroscopic observations from which detailed chemical abundance patterns of individual stars can be obtained. Early star formation efficiencies (SFEs) can be estimated from the "knee" in the α-element abundance trend (e.g., Tinsley 1979; Shetrone et al. 2003; Kobayashi et al. 2006; Nidever et al. 2014; Kirby et al. 2020), which has revealed that there is likely a dependence on both galaxy mass and environment for star formation history (e.g., Nidever et al. 2020). Additional star formation details, such as variations in the initial mass function (IMF; e.g., McWilliam et al. 2013; Hasselquist et al. 2017; Carlin et al. 2018) or amount of pollution from asymptotic giant branch (AGB) stars (e.g., Bonifacio et al. 2000; Venn et al. 2004; Sbordone et al. 2007; Hansen et al. 2018; Skúladóttir et al. 2019; Reichert et al. 2020; Fernández-Trincado et al. 2020) can be probed by close examination of the abundance patterns of hydrostatic/explosive element abundance ratios and r-/s-process element contributions, respectively. However, the extent to which the abundance patterns can be precisely mapped to parameters that govern star formation (e.g., inflow/outflow, IMF) largely depends on the accuracy of yield tables, which are uncertain for some elements, as well as inherent degeneracies in the predicted model abundance tracks. Moreover, spectroscopic surveys are observationally expensive, and the analysis techniques to extract abundances are susceptible to a range of systematic uncertainties (e.g., using 3D and/or NLTE atmospheres versus 1D plane-parallel ones). Historically, this has meant that comparative spectroscopic SFH studies have required using heterogeneous data from multiple literature sources.

Fortunately, the SDSS-III/IV Apache Point Observatory Galactic Evolution Experiment (APOGEE; Majewski et al. 2017) has obtained spectra of stars beyond just the MW, including the five most massive MW satellites: the Large Magellanic Cloud (LMC), Small Magellanic Cloud (SMC), Sagittarius Dwarf Galaxy (Sgr), Fornax (Fnx), and the Gaia Sausage/Enceladus (GSE). The latter is no longer a coherent structure separated from the MW, but its distinct remnant orbit structure means its stars can be relatively easily selected out from the MW (e.g., Belokurov et al. 2018; Deason et al. 2018; Helmi et al. 2018; Myeong et al. 2018; Gallart et al. 2019; Mackereth et al. 2019; Feuillet et al. 2020; Horta et al. 2021), thus serving as a distinct dwarf galaxy for the purposes of this work. These galaxies span two orders of magnitude in mass, and represent a wide range of formation environments, with GSE having merged early with the MW (e.g., Gallart et al. 2019; Mackereth et al. 2019), Sgr in the process of merging (e.g., Ibata et al. 2001; Majewski et al. 2003; Belokurov et al. 2006; Ruiz-Lara et al. 2020a), Fnx in relative isolation now but with some signatures of major mergers in recent times (e.g., Amorisco & Evans 2012; del Pino et al. 2015, 2017), and the Magellanic Clouds (MCs) falling into the MW for the first time (e.g., Besla et al. 2007; Kallivayalil et al. 2013) while clearly

Table 1
Galaxy Selection

System	Center (α, δ)	D$_{proj}$	V_{helio} (km s^{-1})	μ_α (mas yr^{-1})	μ_δ (mas yr^{-1})	Photometry	N_*	Section
LMC	(80°894, −69°756)	<12°	161 < V_{helio} < 370	1.01 < μ_α < 2.62	−1.15 < μ_δ < 1.70	($J − K_s$) <1.3; RGB[a]	3909	3.1;A.1
SMC	(13°187, −72°829)	<8°	66 < V_{helio} < 235	0.05 < μ_α < 1.51	−1.57 < μ_δ < −0.94	($J − K_s$) <1.3; RGB	1,146	3.1;A.1
GSE[b]	...	...	...	...	...	...	972	3.2;A.2
Sgr[c]	...	...	...	...	...	...	946	3.3;A.3
Fnx	(39°748, −34°376)	<0°9[d]	17 < V_{helio} < 89	0.17 < μ_α < 0.60	−0.71 < μ_δ < −0.05	...	192	3.4;A.4

Notes.
[a] RGB tip, described in Appendix A.1.
[b] Primarily orbital selections.
[c] Primarily kinematic selections in Sgr coordinate frame.
[d] Single APOGEE plug plate.

interacting with each other (e.g., Harris & Zaritsky 2009; Nidever et al. 2010; Besla et al. 2016). Using APOGEE observations, we can now perform a detailed, homogeneous comparison of the SFHs of these galaxies from the *spectroscopic* perspective.

In this work we present the detailed chemical abundance patterns of 10 elements for each of these five galaxies. We quantify the relative differences in the median abundance patterns of these galaxies, allowing for more robust conclusions about their relative SFEs and SFHs, and more generally about the nucleosynthesis of different elements in these disparate galaxies. We then use two chemical evolution models to interpret these differences as actual physical differences in SFH parameters. Our observations and data reduction are described in Section 2, and the sample selection is described in Section 3. Chemical abundance results are shown and compared in Section 4. We fit chemical evolution models to the abundance results in Section 5, and these results are discussed and compared to previous star formation history studies in Section 6. Our conclusions are presented in Section 7.

2. Observations and Data Reduction/Analysis

Observations were taken as part of APOGEE (Majewski et al. 2017), part of the third and fourth iteration of the Sloan Digital Sky Survey (SDSS-III and SDSS-IV; Eisenstein et al. 2011 and Blanton et al. 2017, respectively). The APOGEE instruments are high-resolution ($R \sim 22{,}000$), near-infrared (*H*-band) spectrographs (Wilson et al. 2019) observing from both the Northern Hemisphere at Apache Point Observatory (APO) using the SDSS 2.5 m telescope (Gunn et al. 2006), and the Southern Hemisphere at Las Campanas Observatory using the 2.5 m du Pont telescope (Bowen & Vaughan 1973). To date, the dual APOGEE instruments have observed some 700,000 stars across the MW and nearby systems, targeting these stars with selections described in Zasowski et al. (2013) and Zasowski et al. (2017), with updates to the targeting plan described in Santana et al. (2021) and Beaton et al. (2021).

We use APOGEE results from the 17th Data Release of SDSS (DR17; K. Masters et al. 2021, in preparation). Spectra are reduced as described in Nidever et al. (2015) (with updates described in J. Holtzman et al. 2021, in preparation) and analyzed using the APOGEE Stellar Parameters and Chemical Abundance Pipeline (ASPCAP; García Pérez et al. 2016), which uses the FERRE code (Allende Prieto et al. 2006) to interpolate in a grid of model synthetic spectra (Zamora et al. 2015) to find the best-fit stellar parameters and abundances. Updates to the DR17 chemical abundance analysis include

Table 2
Galaxy Selection

APOGEE ID	System
2M03141881-7642442	LMC
2M03173277-7702254	LMC
2M03174293-7712511	LMC
...[a]	

Note.
[a] full version online.

(This table is available in its entirety in machine-readable form.)

cerium abundances using lines characterized in Cunha et al. (2017), as well as NLTE corrections for Na, Mg, K, and Ca (Osorio et al. 2020). Validation of the APOGEE abundance results can be found in Jönsson et al. (2018), Nidever et al. (2020), and J. Holtzman et al. (2021, in preparation).

3. Sample Selection

In this work we analyze five dwarf galaxy stellar samples (LMC, SMC, GSE, Sgr, and Fnx) along with a comparison MW sample, for a total of six stellar samples. For each sample, we start with the following cuts:

1. Median S/N per pixel >70 (except for Fnx, see Appendix A.4) to ensure precise abundances.
2. No STAR_BAD bit set in the ASPCAPFLAG[39] to remove problematic/suspect abundance determinations.
3. [Fe/H] < 0.0 to remove obvious MW contamination from the dwarf galaxy samples.
4. Remove duplicate observations of a single target that have bit 4 of EXTRATARG set.[40]

Sample selection is then made through a mix of spatial, kinematic, and simple chemical selection criteria. We briefly describe the selection for each sample below, but refer the reader to Appendix A for more detailed plots and descriptions.

The criteria used to select each sample are summarized in Table 1, and the APOGEE IDs for each sample are in Table 2. To reproduce the results of this paper, one can match Table 2 to the APOGEE allStar catalog.[41] Figure 1 shows the spatial

---

[39] See DR17 web documentation.
[40] See DR17 web documentation for a full description of this flag. https://www.sdss.org/dr16/algorithms/bitmasks/#APOGEE_EXTRATARG
[41] https://data.sdss.org/datamodel/files/APOGEE_ASPCAP/APRED_VERS/ASPCAP_VERS/allStar.html
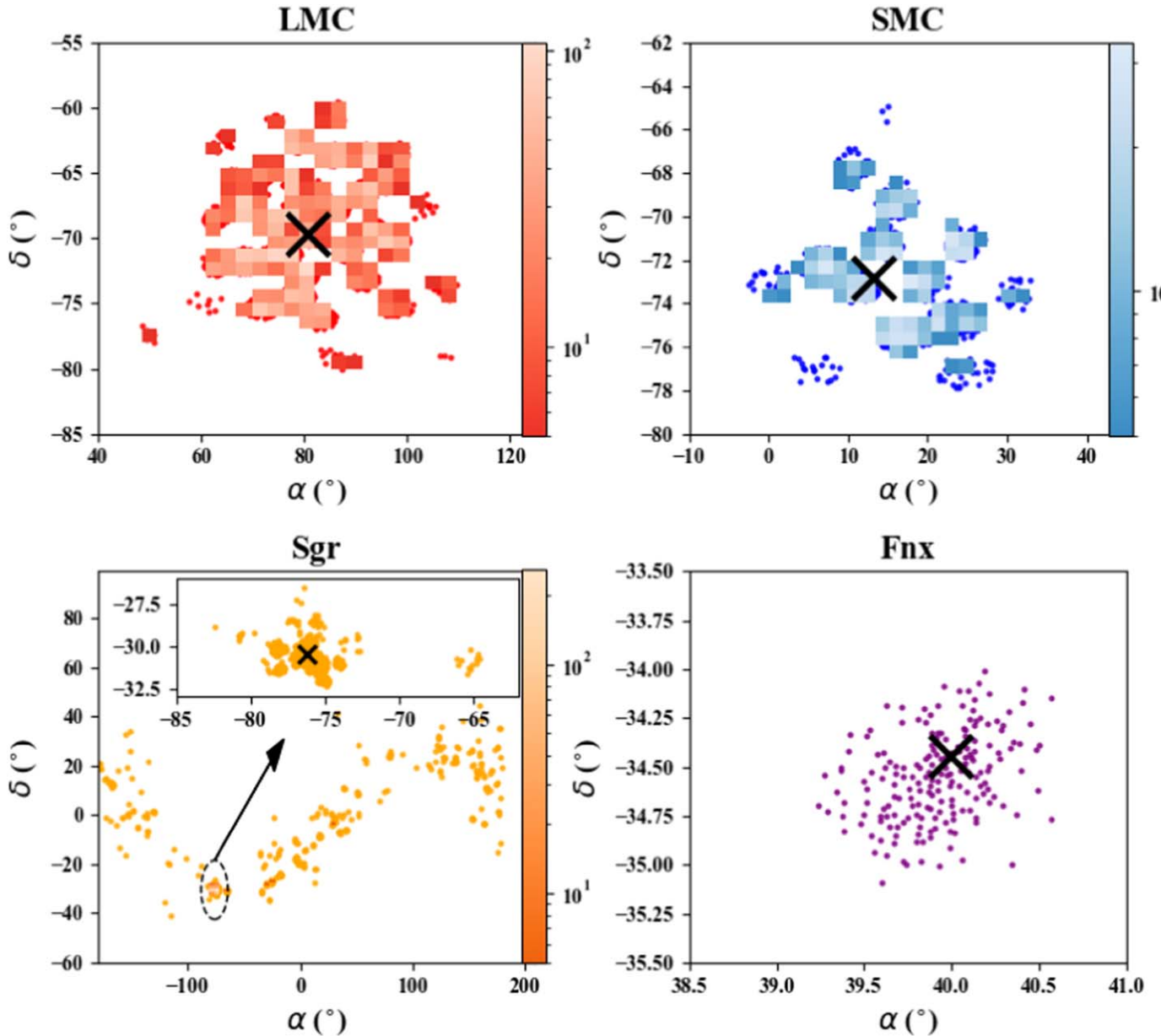
Figure 1. Right ascension (α) and decl. (δ) maps of four galaxies: LMC (red, upper left), SMC (blue, upper right), Sgr (orange, lower left), Fnx (purple, lower right). Spatial density bins are plotted except where the bin count is below five stars. Black crosses mark the photometric centers of these galaxies, and are noted in Table 1. The dashed circle in the lower-left panel highlights the Sgr "main body" region, the coverage of which is shown in the inset. About two-thirds of our Sgr targets reside in this main body region.

distribution of each galaxy. The APOGEE observations cover much of the spatial extent of these galaxies, including nearly continuous coverage of the Sgr main body (or core) and stream.

3.1. Magellanic Clouds

The MCs have been extensively observed by APOGEE-2S, with many programs targeting stars across a wide range of evolutionary types (see Nidever et al. 2020 and Santana et al. 2021), including red giant branch (RGB) stars, oxygen-rich asymptotic giant branch (O-AGB) stars, C-rich AGB stars (C-AGB), and massive ($M \gtrsim 3\,M_\odot$) red supergiant (RSG) stars. To select our MC sample we use a combination of spatial, kinematical, color, magnitude, and metallicity cuts, described in detail in Appendix A.1. Because only the RGB stars have well-vetted stellar parameters and abundances from APOGEE,

we remove the O-AGB, C-AGB, and RSG stars by only selecting stars that are below the RGB tip (as defined by Hoyt et al. 2018). However, because the stars above the RGB tip are generally the more massive stars in the MCs, removing these stars means that we are biasing our sample against the youngest (age $\lesssim 1$ Gyr) MC stars. These cuts result in samples of $\sim$3900 stars for the LMC and $\sim$1100 stars for the SMC. This sample is largely comprised of RGB stars, but likely still contains AGB stars that are below the RGB tip. These stars span a large spatial extent of the MCs, as shown in the top row of Figure 1.

The $\log(g)$–$T_{\rm eff}$ distribution of these stars is shown in the left two panels of Figure 3. While most of the MC stars that pass these cuts have $\log(g)$ and $T_{\rm eff}$ consistent with being upper giant branch stars, the LMC contains three groups of stars that have different stellar parameters than the majority of the sample: (1) the clump of $\log(g) < 0$ stars in the LMC panel of Figure 3, (2)
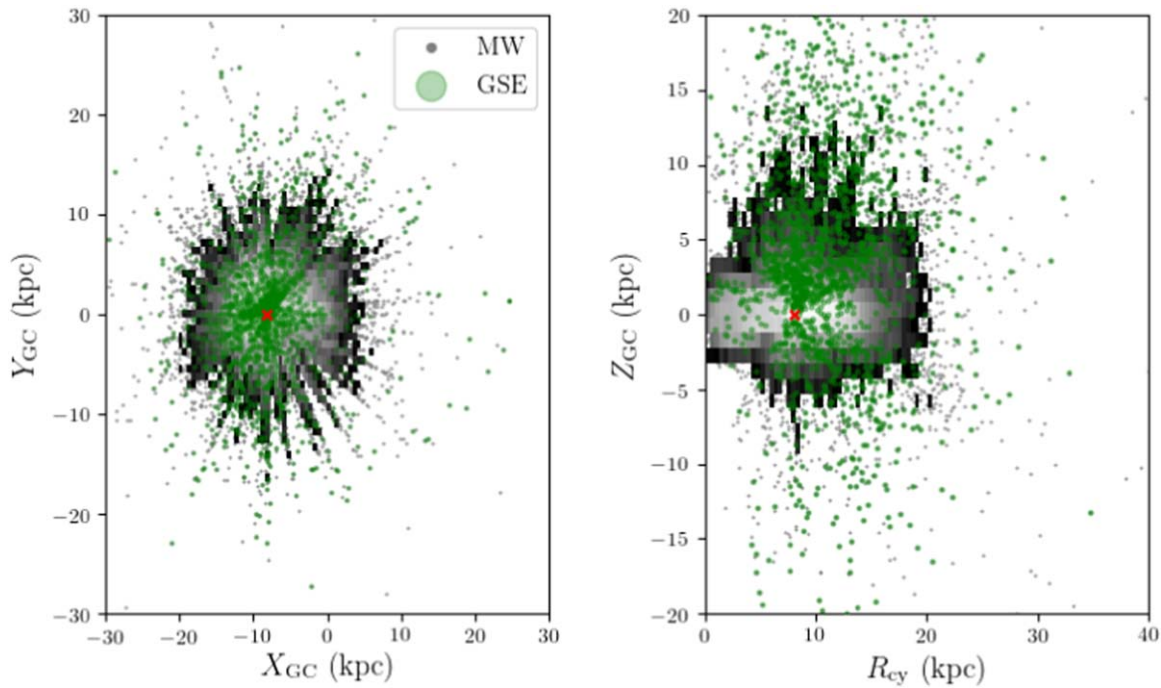
Figure 2. Map of the GSE members (green) studied in this work using astroNN distances (Leung & Bovy 2019). Left: rectangular X and Y Galactic coordinates, where the position of the Sun is notated by a red cross. Right: vertical height above/below the plane plotted as a function of Galactic cylindrical radius. The gray-scale density map shows the location of APOGEE MW stars.

the cool, higher gravity stars ($\log(g) > 1.5$ and $T_{\rm eff} < 4200$ K, and (3) stars at $T_{\rm eff} > 5000$ K. After analyzing these stars and comparing them to other surveys, we have determined that they are (1) thermally pulsating asymptotic giant branch stars (TP-AGB), enhanced in C+N, (2) likely mass-transfer binaries, enhanced in [Ce/Fe], and (3) identified as Delta Cep pulsators by Soszynski et al. (2008). We do not explicitly remove these stars, and present their chemical results in Section 5.3.

3.2. Gaia Sausage/Enceladus

In this work, we treat the accreted halo stars, defined below, as originating from one progenitor, the GSE, that has since merged with the MW. However, when treating the GSE as one entity, we assume that we have selected stars in a way that is not chemically biased. A compact remnant for GSE has not yet been confirmed. Should this remnant exist and be absent from our selection, then it is possible we are missing the most chemically evolved GSE stars in our sample. Furthermore, like other studies, we are assuming the stars come from one progenitor rather than multiple. We are also only explicitly removing stars in known globular clusters, but should GSE contain dissolved globular cluster (GC) stars, then we might expect our sample to contain stars that show GC-like abundance pattern variations. However, these stars are likely to comprise only a small fraction of our GSE sample, and will not significantly impact our interpretations of the median abundance trends.

There is now a wide range of literature that shows how GSE stars can be selected by applying various kinematical and dynamical selection criteria. In this work, we follow Feuillet et al. (2020) and select stars in $\sqrt{J_R}-L_z$ space, with these quantities provided in the astroNN[42] APOGEE DR17 value-

added catalog (Leung & Bovy 2019). These selections result in some contamination from the high-α MW disk, so we perform a chemical cut in [(C+N)/Fe] for stars with [Fe/H] > -1.05 to remove the obvious high-α MW stars, which are $\sim$0.2–0.3 dex enhanced in [(C+N)/Fe] as compared to GSE. Selecting GSE members is described in more detail in Appendix A.2, and our final sample consists of $\sim$1000 stars. Figure 2 shows that our GSE sample studied here primarily comes from stars near the solar radius, at $\pm$5 kpc from the plane of the MW, although some stars do come from much further away. To make these maps we use distances from DR17 astroNN (Leung & Bovy 2019).

3.3. Sagittarius

To select Sgr members, we take a similar approach to that of Hayes et al. (2020). We first only consider stars with [Fe/H] < 0.0, a heliocentric distance greater than 10 kpc, and within $\pm 30°$ of the plane of the Sgr stream (Majewski et al. 2003). Then, we make an initial selection in the $V_{\rm zs}$–$L_{\rm zs}$ plane, where $V_{\rm zs}$ and $L_{\rm zs}$ are the vertical velocity and angular momenta in the Sagittarius Galactocentric coordinate system, as derived and described in Majewski et al. (2003). We then make further selections in the $\phi_{\rm vel,s}$–Λ_s plane—where $\phi_{\rm vel,s}$ is the velocity direction in the X and Y directions of the Sgr coordinate system and Λ_s is the longitude along the Sgr stream (Majewski et al. 2003; Hayes et al. 2020)—to remove stars that are moving perpendicular to the stream. We describe the selection process in more detail in Appendix A.3. The final Sgr sample consists of $\sim$1000 stars, about two-thirds of which are in the main body of Sgr (within 12° of the center of Sgr). See Appendix A.3 for details on the coverage of the Sgr main body.

3.4. Fornax

The APOGEE Fnx field was designed specifically to observe likely members based on radial velocities (RVs), proper

----

[42] https://www.sdss.org/dr16/data_access/value-added-catalogs/?vac_id=the-astronn-catalog-of-abundances,-distances,-and-ages-for-apogee-dr16-stars
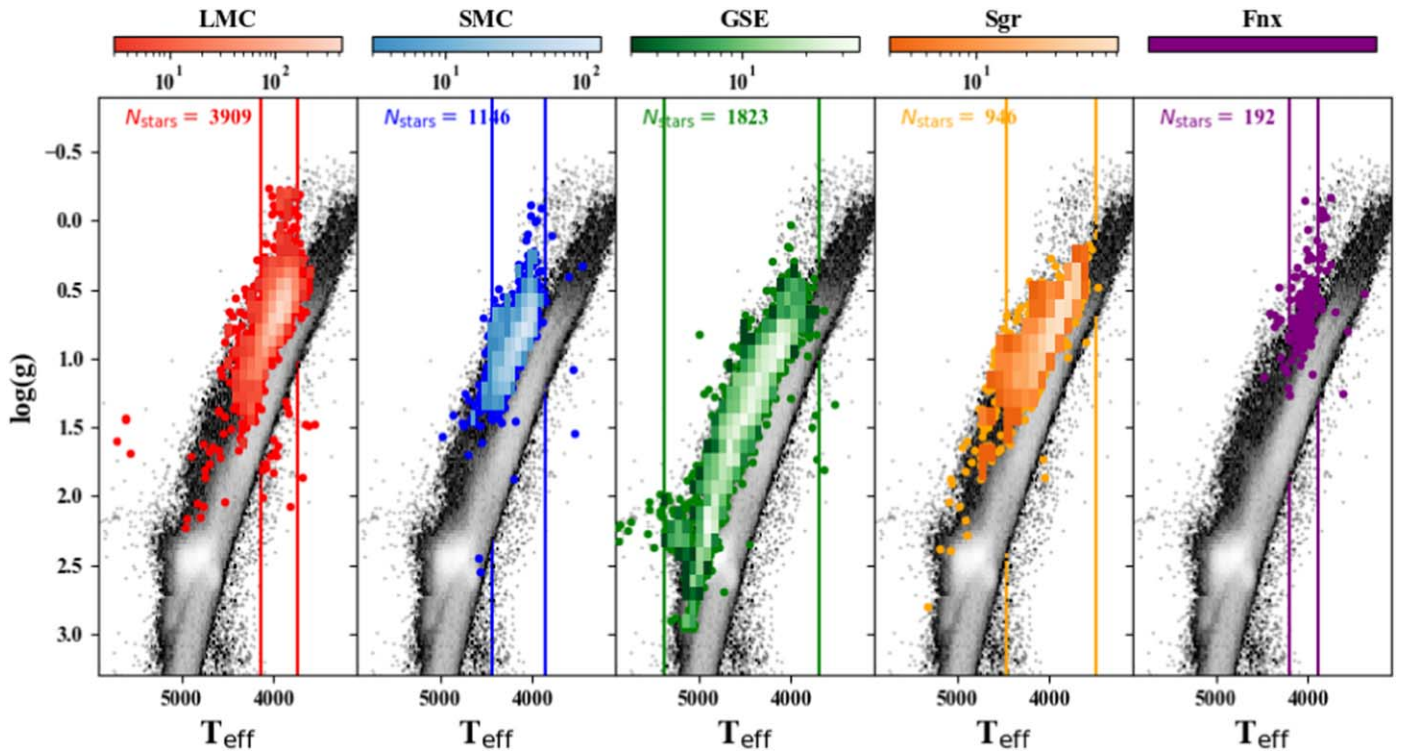
Figure 3. Hertzsprung–Russell diagram for the five different galaxy samples (monochromatic density maps and circles where bins contain fewer than five stars) plotted with the Hertzsprung–Russell diagram of the T_{eff}-matched MW stars (gray-scale density). Horizontal lines indicate the 2σ T_{eff} range adopted to select out the MW comparison samples.

motions, and/or CMD (see Zasowski et al. 2017 and Santana et al. 2021). Therefore, most targets in this field are likely Fnx members, but we reanalyze the APOGEE RVs and Gaia proper motions to remove any contamination. We adopt a lower cut of S/N >40 for the Fnx sample to include a meaningful number of stars to compare to the other galaxies. This lower S/N cut means that the individual abundance uncertainties are generally larger for Fnx stars than the stars in other galaxies. The final selection cuts we used are shown in Table 1, and the process is described in more detail in Appendix A.4.

3.5. MW Comparison Sample

While the APOGEE pipeline has had several improvements to eliminate T_{eff} and $\log(g)$ systematics in abundance determination (Jönsson et al. 2020), recent work by Griffith et al. (2021) shows that some elemental abundances still exhibit some small systematic trends in abundance with T_{eff} and $\log(g)$ (e.g., Al and Si). Thus, to minimize these effects on our interpretations of the abundance trends, we compare each galaxy to an MW sample of roughly similar stellar parameters. For each galaxy, we select a T_{eff} range corresponding to $\pm2\sigma$ from the median T_{eff} values of each galaxy, as shown in Figure 3.

For the MCs, Sgr, and Fnx, we are primarily analyzing the abundance patterns of luminous giants ($\log(g) \lesssim 1.5$). While we do not make specific spatial selections for the MW stars, the MW comparison sample for the MCs, Sgr, and Fnx, covers much of the MW disk and bulge region. The GSE sample spans much of the giant branch ($0.5 < \log(g) < 3.0$), so the MW comparison sample contains a larger fraction of intrinsically less-luminous stars, resulting in an MW sample that is primarily located spatially within 1–2 kpc from the Sun. Weinberg et al. (2019) show that the median trends of

APOGEE elemental abundance ratios are nearly independent of location in the disk, provided one separates the low-α and high-α populations, so we do not expect geometrical selection effects within the MW to have an effect on our comparison.

4. Chemical Abundance Results

In this section, we present the elemental abundances for C+N, the α-elements (O, Mg, Si, Ca), Al, Ni, and Ce. We select these elements because they are among the most precise APOGEE abundances across the full parameter space covered here, and are among the most accurate when comparing to optical studies (see, e.g., Jönsson et al. 2018, 2020). We combine C and N because stars will change their [C/Fe] and [N/Fe] abundances during dredge-up ascending to and along the giant branch, but these processes occur in such a way that the [(C+N)/Fe] abundance is largely constant before and after these mixing processes (see, e.g., Gratton et al. 2000). We compare the abundance patterns of each galaxy to the abundance pattern of the MW in this section, as well as compare the abundance patterns of the dwarf galaxies to each other.

Throughout these sections, we describe various aspects of the abundance patterns of each galaxy, linking certain features to physical drivers of SFH, such as an early SFE or the presence/strength of a secondary starburst. We provide an example schematic diagram of how we interpret abundance patterns in Figure 4. In the top row of Figure 4 we show flexCE (described in detail in Andrews et al. 2017, Section 5.1, and Appendix B) chemical evolution model tracks (left) with mock observations of the tracks (right) to show what the abundance patterns of two galaxies (labeled as "Dwarf Galaxy Model" and "MW Model" in Figure 4) with different initial SFEs look like in the [Si/Fe]–[Fe/H] abundance space. The combination of the SFE
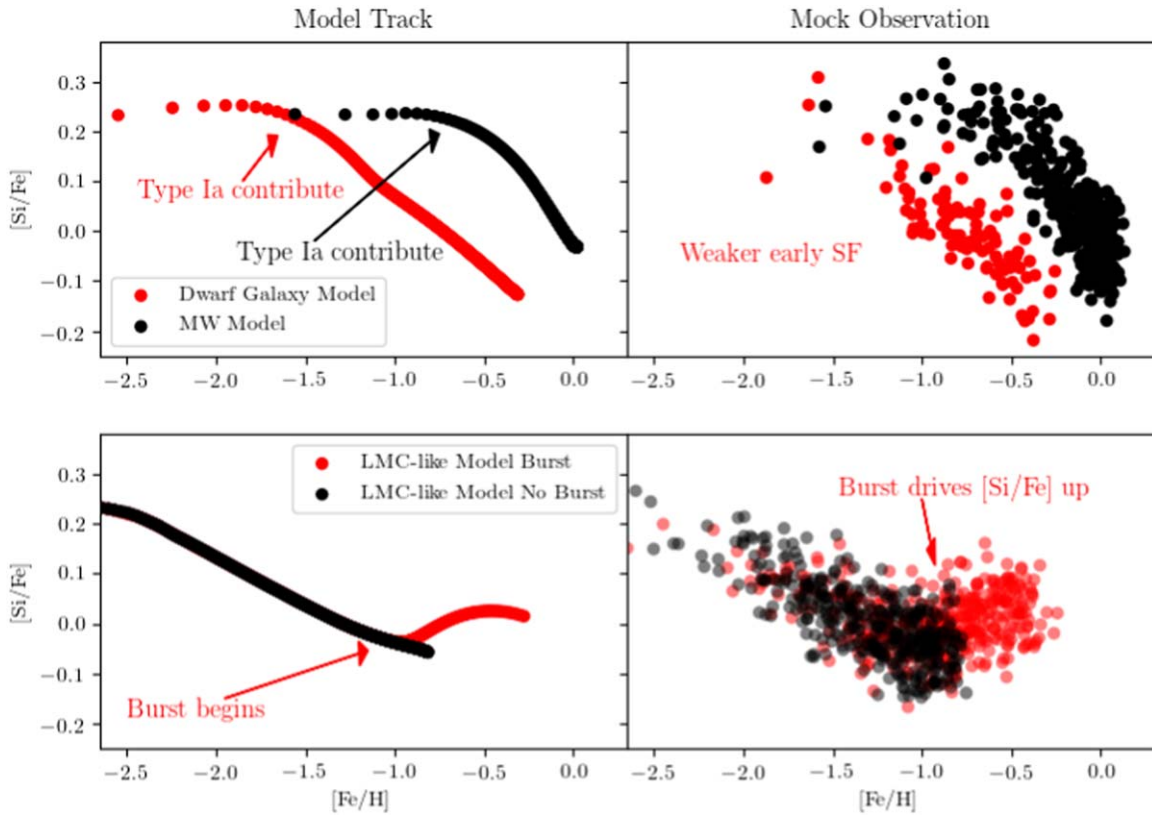
Figure 4. Chemical evolution model tracks of the [Si/Fe]–[Fe/H] abundance plane (left column) along with mock observations sampled from these tracks with 0.05 dex abundance uncertainties (right column). The top row compares two galaxy model tracks with different early star formation efficiencies, and the bottom row compares two galaxy model tracks with identical early star formation efficiencies, but one with a secondary burst of star formation.

(SFE $\equiv \dot{M}_*/M_{\rm gas}$) and the gas supply ($M_{\rm gas}(t)$) determines the star formation rate (SFR $(t) = \dot{M}_*(t)$). The gas supply in turn depends on the gas accretion history, and is further regulated by star formation and outflows (which deplete $M_{\rm gas}$) and recycling from evolved stars (which replenishes $M_{\rm gas}$).

The top row of Figure 4 shows that the [Si/Fe]–[Fe/H] abundance pattern of the lower SFE dwarf galaxy model (red) begins to decrease with increasing [Fe/H] at much lower [Fe/H] values than the higher SFE MW model (black). In both galaxies, the [Si/Fe] abundance decreases after Type Ia SNe begin to substantially contribute to the chemical evolution of these galaxies, which is thought to occur some time after star formation begins (see, e.g., Tinsley 1979). Type Ia SNe produce Fe without producing much Si (which is primarily produced in Type II SNe), resulting in a decrease of the [Si/Fe] abundance as the Type Ia/Type II SNe ratio increases. Because the delay time at which Type Ia SNe begin to contribute to the chemical enrichment of these galaxies is assumed to be the same, the metallicity at which [Si/Fe] begins to decrease (sometimes referred to as the α-element abundance "knee") probes the early SFE of a galaxy, with more metal-poor knees indicating a galaxy experienced fewer Type II SNe events contributing to its enrichment before the delayed Ia SNe started to contribute. Therefore, from these abundance patterns, we would conclude that the dwarf galaxy experienced lower efficiency SF at early times than the MW.

The bottom row of Figure 4 compares two dwarf galaxies with the same early SFE, but the red track emphasizes how a starburst influences the [Si/Fe]–[Fe/H] track. The red model track was used in Nidever et al. (2020) to explain the rising

[α/Fe] abundance pattern observed in the APOGEE LMC data. We would therefore conclude that the red dwarf galaxy experienced some secondary star formation epoch whereas the black dwarf galaxy did not. In this example, the starburst is induced by temporarily increasing the SFE while maintaining the same gas accretion history (see Section 5.1). Many more examples of the influence of star formation and outflow parameters on evolutionary tracks can be found in Andrews et al. (2017) and Weinberg et al. (2017), and a systematic exploration of chemical evolution tracks with starbursts can be found in Johnson & Weinberg (2020).

APOGEE abundance results of each dwarf galaxy as compared to their respective MW comparison samples are shown in Figures 5 and 6. Figure 5 shows the "traditional" abundance patterns using Fe as the reference element ([X/Fe]–[Fe/H]), whereas Figure 6 shows the abundance patterns using Mg as a reference element ([X/Mg]–[Mg/H]) to analyze abundance patterns as a function of Type II SNe ejecta alone, following Weinberg et al. (2019). Each row of these Figures shows a different elemental abundance ratio ([X/Fe] or [X/Mg]) plotted against a "metallicity indicator," represented by [Fe/H] or [Mg/H]. Each column shows how a given dwarf galaxy's abundances compare to that of its respective MW comparison sample. The MW comparison samples are nearly identical for the LMC, SMC, Sgr, and Fnx panels, but the MW comparison sample for GSE contains a much larger fraction of lower luminosity stars. The chemical abundance pattern for each sample is plotted as a density map except for where the pixel contains fewer than five stars, where the individual measurements are displayed as circles instead.
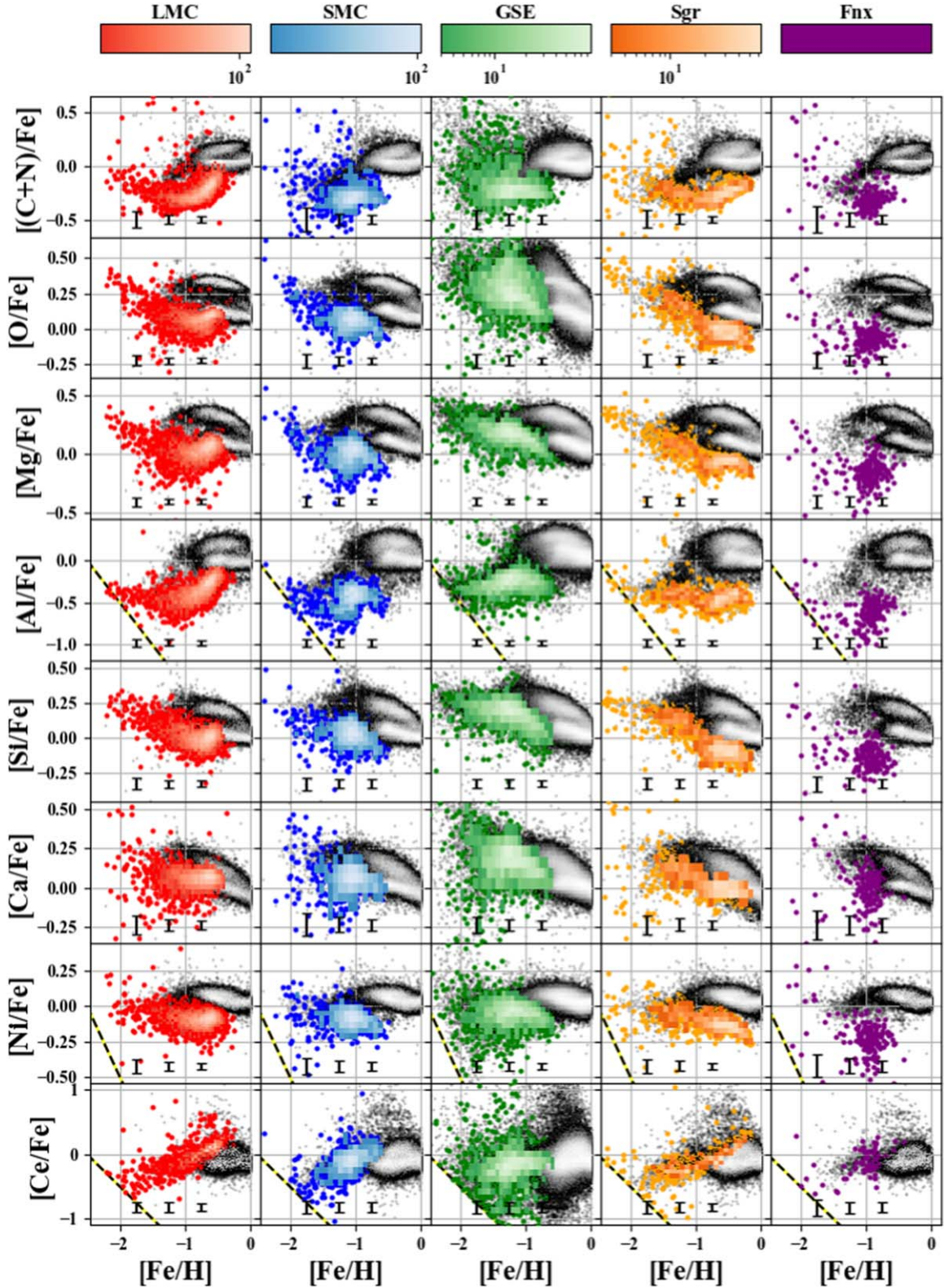
Figure 5. Chemical abundance patterns of select elements for each of the dwarf galaxies as compared to the MW. Overplotted for each galaxy are 2D density histograms except for bins where the density falls below five stars. The dashed black line in the [Al/Fe], [Ni/Fe], and [Ce/Fe] panels indicate the grid edges, below which the APOGEE spectra grids do not extend. Representative median individual uncertainties in the abundances for each dwarf galaxy are shown in black at the bottom of each panel.

To compare the chemical tracks of the dwarf galaxies with each other, we also show the median abundance tracks for the dwarf galaxies all in one panel per chemical element in Figure 7, with [X/Fe]–[Fe/H] plotted on the left column and [X/Mg]–

[Mg/H] plotted on the right column. Running medians are calculated in bins of 30 stars. Because GSE sampled a much larger section of the giant branch than the other dwarf galaxies, we only include stars with $3600\,\mathrm{K} < T_{\mathrm{eff}} < 4200\,\mathrm{K}$ to make for a
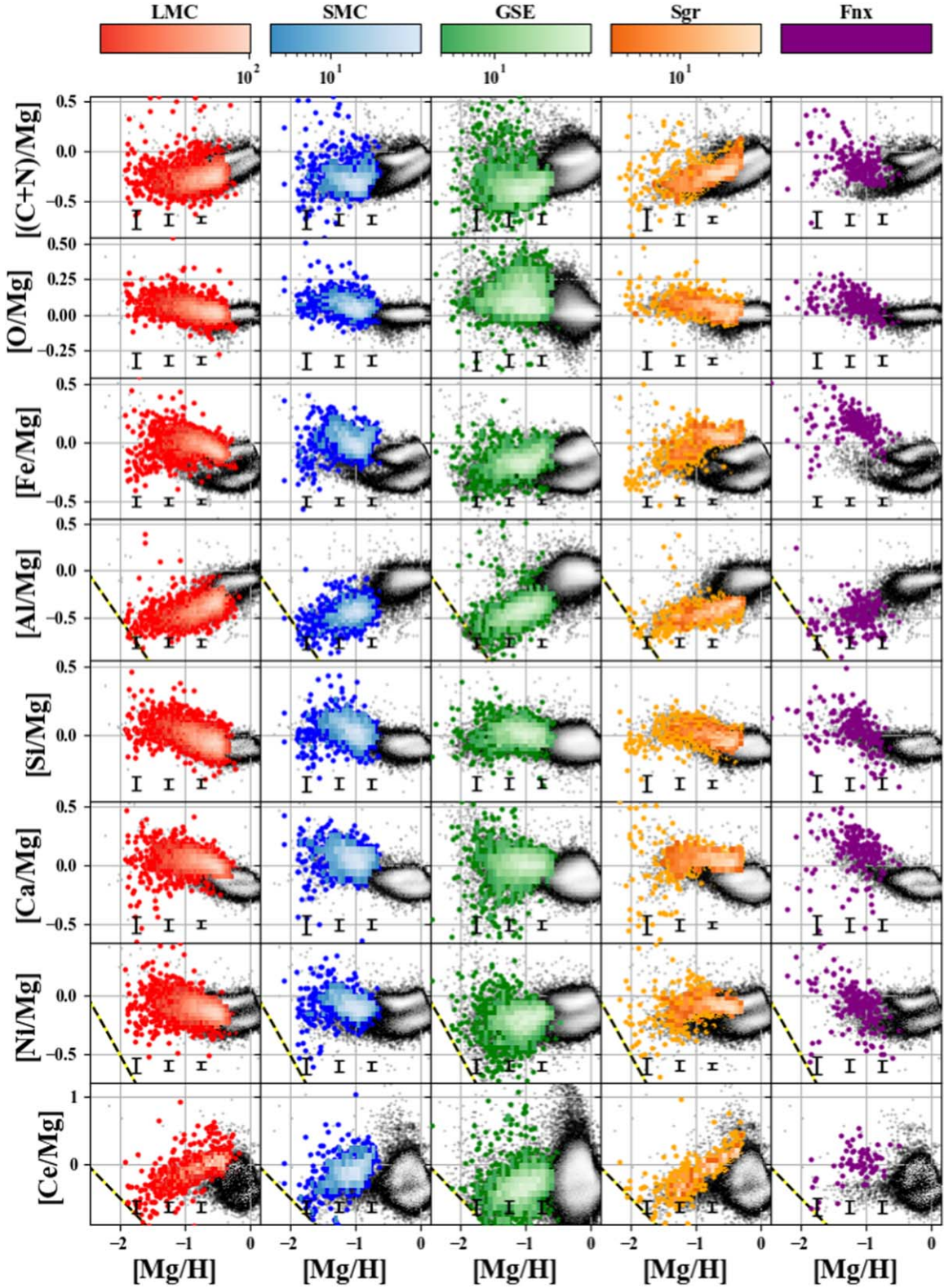
Figure 6. Same as in Figure 5, but using Mg as the reference element instead of Fe.

more systematic-free comparison. We also select a comparison MW sample to now only cover $3600\,\mathrm{K} < T_\mathrm{eff} < 4200\,\mathrm{K}$.

In the following subsections, we describe the chemical abundance patterns of each galaxy, regularly referring to Figures 5, 6, and 7.

4.1. LMC

The left columns of Figures 5 and 6 show the abundance patterns for the LMC. The APOGEE LMC sample contains stars across a wide range of metallicities, $-2.2 < [\mathrm{Fe/H}]$
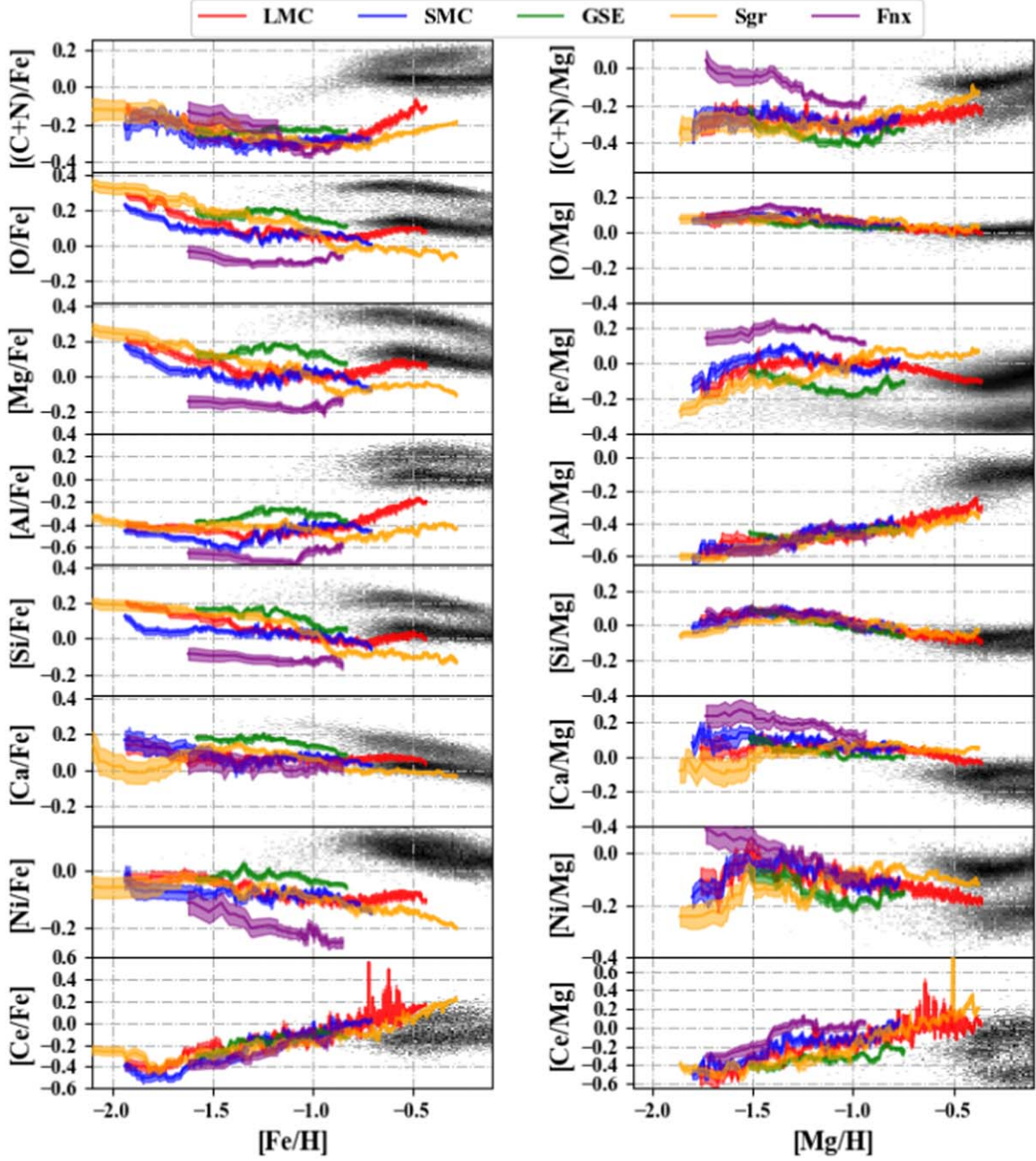
Figure 7. Median abundance tracks (solid colored lines) and associated $\pm 1\sigma$ uncertainties on the median track (colored shaded regions) for each galaxy in moving bins of 30 stars. The MW sample is plotted as a gray-scale density image. We have removed all GSE and MW stars with $T_{\rm eff} > 4200$ K to make for a relatively systematic-free comparison across all galaxies. Note that vertical axis ranges vary from panel to panel, but gray dotted–dashed horizontal lines are spaced at 0.20 dex in all panels so they can be used as a visual reference for comparing the strength of metallicity trends across elements.

< -0.3, making it currently one of the most metal-rich MW satellite galaxies (compare the median abundance tracks in Figure 7). Such a wide metallicity range implies an extended star formation history, the complexity of which is highlighted in the [X/Fe] and [X/Mg] abundance patterns, as described in detail below.

4.1.1. O, Mg, Si, and Ca

The α-elements, O, Mg, Si, and Ca, are primarily produced in massive stars and released to the ISM via Type II SNe, with Si and Ca having non-negligible contributions from Type Ia SNe in the MW disk (e.g., Weinberg et al. 2019). As already shown by Nidever et al. (2020), and again presented in the left columns of Figures 5 and 7, the APOGEE LMC sample exhibits an [α/Fe]–[Fe/H] abundance pattern that decreases over the metallicity range $-2.2 < [{\rm Fe/H}] < -1.2$ to subsolar [α/Fe] values, before increasing to intersect with the MW low-α disk trend. Nidever et al. (2020) interpreted this pattern as very weak (i.e., low efficiency) early star formation, followed by a strong burst in star formation that occurred in more recent

times, when many Type II SNe drove up the α-element abundance. This picture is qualitatively consistent with photometric studies of the LMC (e.g., Harris & Zaritsky 2009; Monteagudo et al. 2018; Ruiz-Lara et al. 2020b), but is only somewhat consistent with other spectroscopic studies. Many spectroscopic abundance studies (e.g., Smith et al. 2002; Lapenna et al. 2012; Van der Swaelmen et al. 2013) find that the more metal-poor LMC stars are deficient in the α-elements relative to the MW, but only the Mg abundances of Lapenna et al. (2012) show a flat or slightly increasing [Mg/Fe] abundance with metallicity at [Fe/H] >-1.5. We refer the reader to Nidever et al. (2020) for a more detailed discussion of the comparison samples, but note here that the APOGEE sample studied in this work is a factor of $\sim$40 larger than other high-resolution abundance studies. Moreover, the APOGEE random uncertainties of individual abundance measurements are about one-fourth of those presented in other studies.

While the pattern of low, early star formation (SF) followed by a major burst is seen across all α-elements, the extent to which the metal-rich LMC stars overlap the MW disk sample varies. The [O/Fe] and [Mg/Fe] abundance patterns reach the MW low-α disk trend, whereas the [Si/Fe] and [Ca/Fe] actually rise above the MW low-α disk trend (perhaps best seen in the left column of Figure 7). The [O/Mg], [Si/Mg], and [Ca/Mg] abundances all slightly decrease with increasing [Mg/H], with [Ca/Mg] remaining $\sim$0.05 dex above the MW trend at [Mg/H] $= -0.4$.

Compared to the other dwarf galaxies (Figure 7), only Sgr extends to as high metallicities as the LMC. However, the metal-poor LMC stars have lower [α/Fe] (by $\sim$0.05–0.1 dex) than the Sgr stars until [Fe/H] $= -1.0$, at which point the LMC increases its [α/Fe] abundance, whereas the [α/Fe]–[Fe/H] abundance track of Sgr continues to decrease before becoming mostly flat. Over the metallicity range $-1.5 <$ [Fe/H] < -1.0, the LMC is $\sim$0.2 dex deficient across all α-elements compared to GSE. Despite these differences in the [α/Fe]–[Fe/H] tracks, most galaxies show similar decreasing [α/Mg] abundances with increasing [Mg/H], the exception being Fnx in [Ca/Mg] (discussed more in Section 4.5).

4.1.2. Carbon and Nitrogen

Carbon and nitrogen are elements that are thought to be produced in great quantities in type II SNe, with nitrogen yields expected to have some dependence on progenitor metallicity (e.g., Kobayashi et al. 2006). Both elements are also thought to be produced in appreciable amounts by AGB stars (e.g., Nomoto et al. 2013; Karakas & Lattanzio 2014; Andrews et al. 2017; Rybizki et al. 2017). Throughout this work, we analyze the sum of these abundances, [(C+N)/Fe] and [(C+N)/Mg], as red giant stars undergo dredge-up processes that mix the surface abundances with material produced as a consequence of nuclear reactions deeper in the star. This mixing operates in a way such that the star's birth C+N abundance is largely conserved (e.g., Iben 1964; Gratton et al. 2000; Salaris et al. 2015; Vincenzo et al. 2021).

The [(C+N)/Fe] abundance pattern of the LMC shows a slight decrease from -0.1 to ~-0.3 dex over the range $-2.2 <$ [Fe/H] < -1.2. At [Fe/H] >-1.2, the [(C+N)/Fe] is flat at 0.3 dex below the MW abundance trend before rapidly increasing to almost intersect with the MW low-α "thin" disk trend at [Fe/H] $= -0.3$. In the [(C+N)/Mg]–[Mg/H] abundance plane shown in Figure 6 and in the right column of

Figure 7, both the LMC and the MW high-α "thick" disk stars show similar trends of slightly increasing [(C+N)/Mg] with [Mg/H] in their region of overlap, with the LMC pattern being enhanced by $\sim$0.1 dex. Over the wide metallicity range $(-1.7 <$ [Mg/H] $< -0.5)$ the LMC [(C+N)/Mg] trend is flat to within $\sim$0.05 dex, implying that (C+N) production tracks Mg production at these metallicities.

As shown in Figure 7, only Sgr appears to show a similar increase in [(C+N)/Fe] as the LMC at [Fe/H] >-0.7, although this increase is not as steep as the increase in the LMC. Most other galaxies show a similar slight decrease of [(C+N)/Fe] from [Fe/H] $= -2.0$ to [Fe/H] $= -1.0$, although both Fnx and GSE have enhanced [(C+N)/Fe] over this metallicity range as compared to the LMC by $\sim$0.15 dex. However, the [(C+N)/Mg]–[Mg/H] abundance patterns show that Fnx is enhanced as compared to the LMC, and GSE is actually slightly deficient.

4.1.3. Aluminum and Nickel

Aluminum is an element thought to be produced by massive stars and released to the ISM solely via Type II SNe with some dependence on progenitor metallicity (e.g., Weinberg et al. 2019), whereas nickel is an element produced in both Type II and Type Ia SNe. The [Al/Fe]–[Fe/H] abundance pattern of the LMC appears qualitatively consistent with the starburst scenario (flat, then increasing abundance at point of starburst). The [Al/Mg] plot shown in the left column of Figure 6 shows that the [Al/Mg] ratio is still about 0.2 dex below the MW trend at the same [Mg/H]. The [Al/Mg]–[Mg/H] abundance tracks are similar across all of the dwarf galaxies (right column of Figure 7), showing a steady rise from [Al/Mg] $\simeq -0.6$ at [Mg/H] $\simeq -1.7$ to [Al/Mg] $\simeq -0.25$ at [Mg/H]$\simeq$, which suggests that Type II Al yields increase steadily over this metallicity range.

The LMC Ni abundance trends for both [Ni/Fe] and [Ni/Mg] are similar to the α-element abundance trends, being most similar to [Si/Fe] and [Si/Mg]. However, [Ni/Fe] remains below the MW low-α disk trend whereas the α-elements reach the same level as the MW low-α disk trend at the highest LMC metallicities. The decline of [Ni/Mg] with increasing [Mg/H] is also steeper than that of [Si/Mg], probably because of a larger Type Ia SNe contribution. The [Ni/Mg] of the metal-rich LMC is slightly deficient as compared to the metal-rich Sgr stars, with the LMC stars lying in between the two MW sequences, and Sgr lying closer to the MW low-α sequence.

4.1.4. Cerium

The heavy s-process element cerium is one of the elements whose abundances are presented in DR17 and is based upon Ce II lines as described in Cunha et al. (2017). The astrophysical source of the s-process elements, such as Ce, is dominated by thermally pulsing (TP) AGB stars, with the probable neutron source being ^{13}C$(\alpha$,n)^{16}O (e.g., Karakas & Lugaro 2016; Prantzos et al. 2018; Kobayashi et al. 2020). This particular neutron source is important, as it takes place in the intershell region (between shell He-burning triple-α and shell H-burning via CN-cycle reactions) between thermal pulses (e.g., Karakas & Lattanzio 2014) and is a primary neutron source (i.e., independent of the star's birth metallicity), driven by the mixing of protons into ^{12}C-rich regions (from triple-alpha) resulting in ^{12}C$(p,\gamma)^{13}$N$(\beta^+,\nu)^{13}$C. Cerium is a sensitive

diagnostic of TP-AGB chemical enrichment, which continues to take place over relatively long timescales (of order several Gyr), and provides information on nucleosynthesis and chemical evolution that complements that provided by the α-elements (massive stars and Type II SNe), the Fe-peak (Type Ia SNe), or the r-process (merging neutron stars).

The LMC [Ce/Fe] pattern increases with [Fe/H] across nearly the entire metallicity range, with the most metal-rich MW stars having slightly enhanced [Ce/Fe] as compared to the MW disk. The rise of [Ce/Fe] with [Fe/H] is similar to what was found by Pompéia et al. (2008) in a sample of LMC red giants for the s-process element barium, which will behave similarly to Ce. There is also a small clump of stars at [Fe/H] $\simeq -0.7$ that are ~ 0.2 dex more enhanced than the rest of the LMC stars, which pulls the median up in Figure 7 to be slightly above the [Ce/Fe] abundance pattern of Sgr.

The LMC [Ce/Mg]–[Mg/H] abundance pattern also shows an increasing [Ce/Mg] with [Mg/H], however, the lower-left panel of Figure 6 and the lower-right panel of Figure 7 shows that the [Ce/Mg] increases more slowly with [Mg/H] at [Mg/H] > -1.0. In the regime of $-1.8 < [Mg/H] < -0.7$, the rise of [Ce/H] with [Mg/H] is well fit by a slope of 1.4, while in the range of $-0.7 < [Mg/H] < -0.2$ the slope drops to ~ 0.9. The different behavior from [Ce/Fe] arises because [Mg/Fe] itself is rising over this interval, probably because of a burst in star formation. This burst evidently boosts Mg more rapidly than Ce, which is as expected if Ce production is dominated by less massive stars. Such a change in slope is less evident in the [Ce/Mg]–[Mg/H] abundance patterns of Sgr, which has a flat [Mg/Fe] trend at high metallicity.

4.1.5. LMC Interpretations

The metal-poor α-element abundance patterns show that, compared to GSE, Sgr, and the MW, the LMC enriched to a much lower [Fe/H] before Type Ia SNe began to contribute to its enrichment, suggesting much lower early SFE. We interpret the increasing α-element abundance patterns at higher metallicity, along with the increases of both [(C+N)/Fe] and [Al/Fe] with increasing [Fe/H], as results of a major starburst in the LMC that occurred at [Fe/H] $\simeq -0.8$ (see Section 5.3 for quantitative modeling). The [Ni/Fe]–[Fe/H] abundance pattern of the LMC is qualitatively similar to the α-element abundance tracks (slight decrease at the metal-poor end followed by a slight increase from the burst), but [Ni/Fe] in the LMC remains below the MW trend at [Fe/H] > -0.7, whereas the α-elements all reach the MW low-α disk trend. Because the [Ni/Mg] ratio at this point in the LMC's evolution is closer to that of the high-α MW disk (e.g., the "pure" Type II SNe [Ni/Mg] abundance), the expectation is that the [Ni/Fe] should be closer to the abundance of the high-α MW disk. The [Ni/Fe] deficiency is therefore plausibly a result of the LMC lacking more metal-rich Type Ia SNe contributing to its chemical evolution, if the production of Ni in Type Ia SNe is indeed metallicity dependent (see, e.g., Woosley & Weaver 1995; Chieffi & Limongi 2004; Seitenzahl et al. 2013; Andrews et al. 2017; Rybizki et al. 2017).

While the trend of increasing [Al/Mg] with increasing [Mg/H] in all dwarf galaxies can be explained by metallicity-dependent Type II SNe yields, the slight deficiency in [Al/Mg] for the most metal-rich LMC and Sgr stars relative to MW stars is a bit difficult to explain given that Al and Mg are both pure type II SNe products (e.g., Weinberg et al. 2019). One plausible

explanation is that the low SFEs in the dwarfs cause a stronger "metallicity lookback" effect—e.g., when the metallicity of the ISM (and newly forming stars) is -0.5, the average metallicities of the stars that enriched the ISM is still significantly lower than -0.5, with consequently lower Al production. This could also be an explanation for the Ni abundance patterns if Ni production is metallicity dependent in both Type Ia and Type II SNe.

[O/Mg] and [Si/Mg] for the LMC, and other dwarf galaxies, slowly decrease (by about 0.1 dex) over the range $-1.3 < [Mg/H] < -0.5$, with both the LMC and Sgr joining the MW trends at [Mg/H] > -0.5. This is either a result of metallicity-dependent Type II SNe yields for these elements (e.g., more Si and O relative to the MW at low metallicity), or a result of a slowly increasing Type II/Type Ia SNe fraction, as star formation was extended after the initial SF epoch. The [Fe/Mg] suggests the latter scenario is plausible, at least from $-0.8 < [Mg/H] < -0.4$, over which the [Fe/Mg] ratio slowly decreases as more Type II SNe contribute. The slightly enhanced [Ca/Mg] for the LMC and Sgr at these metallicities as compared to the MW stars is a result of Type Ia contribution to Ca, which is still substantial even with the starburst injecting many more Type II SNe products than at lower metallicities. These results suggest that Ca has a higher contribution from Type Ia SNe than Si (see, e.g., Tsujimoto et al. 1995; Hayes et al. 2018).

We interpret the slightly increasing [(C+N)/Mg] with [Mg/H] as metallicity-dependent C+N yields in Type II SNe (since the MW high-α stars also show this trend), combined with some contribution of C+N from another source, such as AGB stars, which results in the LMC (and Sgr) trend being slightly elevated from the MW high-α sequence. However, this is a small effect, with [(C+N)/Mg] varying by only ± 0.05 dex over the metallicity range $-1.7 < [Mg/H] < -0.3$. The enhanced [Ce/Fe] and [Ce/Mg] both suggest that the LMC and Sgr experienced significant contributions to their evolution from the s-process (likely from AGB stars), with the most metal-rich stars enhancing to similar levels of [Ce/Mg] as the more metal-rich MW low-α sequence. The slight change in slope observed in the [Ce/Mg]–[Mg/H] abundance pattern of the LMC is likely due to the starburst polluting the ISM with much more Mg from Type II SNe.

4.2. SMC

The second column of Figures 5 and 6 show the abundance patterns of the SMC, and the median abundance tracks (blue) are compared to the other galaxies in Figure 7. The SMC only gets as metal-rich as [Fe/H] $\simeq -0.6$ and [Mg/H] $\simeq -0.7$, ~ 0.3–0.4 dex less than the LMC. This is an expectation from the established mass–metallicity relation in Local Group dwarf galaxies (e.g., Kirby et al. 2010), where the more massive galaxies tend to be more metal-rich. However, the most metal-rich stars of the SMC are still ~ 0.5 dex more metal-poor than the most metal-rich stars in Sgr.

4.2.1. O, Mg, Si, and Ca

The α-elements of the APOGEE SMC sample were first explored in Nidever et al. (2020), where it was noted that the SMC also experienced very weak (low efficiency) early SF. This is shown in the O, Mg, Si, and Ca panels of Figure 5, where the SMC shows a declining α-element abundance ratio

from $-2.2 < $[Fe/H]$ < -1.5$. The [$\alpha$/Fe] abundances for the SMC over this range are $\sim$0.05 dex lower than the LMC [α/Fe] abundances. When using Mg as a reference element, this slightly deficient [α/Fe]–[Fe/H] abundance pattern manifests as a slightly enhanced [Fe/Mg]–[Mg/H] abundance pattern from $-2.0 < $[Mg/H]$ < -1.0$.

The [Mg/Fe]–[Fe/H] abundance pattern is similar to the LMC in that there is a slight increase in [Mg/Fe] beginning at [Fe/H] $\simeq -1.3$, with a peak at [Fe/H] $\simeq -1.0$, followed by a slight decrease. The [O/Fe], [Si/Fe], and [Ca/Fe] abundance patterns are flat over this range. The [α/Mg]–[Mg/H] abundance patterns are nearly identical to the LMC, with the SMC only extending to [Mg/H] $\simeq -0.8$, $\sim$0.4 dex lower than the metal-rich extent of the LMC.

4.2.2. Carbon and Nitrogen

Both the [(C+N)/Fe]–[Fe/H] and [(C+N)/Mg]–[Mg/H] abundance patterns of the SMC are similar to those of the LMC. At [Fe/H] >-0.8, the LMC [(C+N)/Fe] abundance begins to increase with increasing [Fe/H] whereas the SMC appears to remain flat before ending $\sim$0.3–0.4 dex below the MW trend. Because the [(C+N)/Mg]–[Mg/H] abundance of the SMC follows that of the LMC, the slight difference at the metal-rich end of the [(C+N)/Fe]–[Fe/H] abundance pattern is likely due to different amount of Fe from Type Ia SNe between the two galaxies.

4.2.3. Aluminum and Nickel

The Al and Ni abundance patterns of the SMC again are very similar to those of the LMC. The SMC shows slight deficiencies in [Al/Fe] and [Ni/Fe] as compared to the LMC at [Fe/H] < -1.5, as well as at [Fe/H] >-0.8. However, the [Ni/Mg] and [Al/Mg] abundance patterns show that like for the other elements, this difference is driven by a difference in Fe.

4.2.4. Cerium

The [Ce/Fe]–[Fe/H] and [Ce/Mg]–[Mg/H] patterns of the SMC are similar to those of the LMC, including the apparent change in increase of [Ce/Mg] abundance. In the case of the SMC, the respective slopes of the [Ce/Mg] increases are 1.6 and 0.9, with the break in the slope occurring at [Mg/H] ~ -1.3.

4.2.5. SMC Interpretations

The similarities between the SMC and LMC abundance patterns show that they indeed had a similar chemical evolution history, with the LMC enriching to higher metallicities than the SMC by $\sim$0.4 dex, potentially a consequence of its larger mass. However, there are two subtle differences between the two. First, the SMC had slightly weaker early SFE, as shown by its slightly lower α-element abundance for the metal-poor stars (or enhanced [Fe/Mg]). Second, while the small rise of [Mg/Fe] at [Fe/H] $\simeq -1.0$, and the change in slope of the [Ce/Mg]–[Mg/H] abundance pattern all suggest the SMC experienced an increase of Type II SNe, this increase was weaker than that in the LMC. We quantify the relative strengths and timing of these star formation events in the galaxies in Section 5.3.

4.3. GSE

The middle columns of Figures 5 and 6 show the abundance pattern of GSE, and the median tracks are plotted in green in Figure 7. The abundance patterns of this dwarf were studied in detail before it was even confirmed to be a separate entity (e.g., Nissen & Schuster 2010; Schuster et al. 2012; Hawkins et al. 2015; Fernández-Alvar et al. 2018; Hayes et al. 2018). The characteristic abundance pattern of this galaxy is the declining [α/Fe] abundance pattern with increasing [Fe/H] that occurs at lower [Fe/H] values than the MW ($-1.2 \lesssim$ [Fe/H] $\lesssim -0.7$), resulting in a "separate" sequence from the MW disk sequences. There have been some recent works that have fit chemical evolution models to this abundance pattern, finding one major star formation epoch that was cut off some 10 Gyr ago, presumably by its infall onto the MW environment (e.g., Fernández-Alvar et al. 2018; Gallart et al. 2019; Vincenzo et al. 2019).

4.3.1. O, Mg, Si, and Ca

The α-element abundance patterns of the GSE look like a more metal-poor MW high-α disk track. The α-elements are relatively flat at [Fe/H] < -1.3, but decline at [Fe/H] >-1.2, with the most metal-rich GSE stars reaching solar [α/Fe] abundances. Compared to the other dwarf galaxies, GSE is enhanced in [α/Fe] over the metallicity range $-1.5 < $[Fe/H] < -0.7, but still $\sim$0.10–0.15 dex below the MW high-α sequence. The difference in Fe abundance at fixed [Mg/H] is highlighted in the [Fe/Mg]–[Mg/H] panel of Figure 7, where the GSE abundance pattern lies much closer to the MW high-α sequence (low-Fe) than that of the other dwarf galaxies.

The [O/Mg], [Si/Mg], and [Ca/Mg] abundances of GSE are all within $\sim$0.05 dex of solar over its full metallicity range, consistent with production by a population of massive stars that is similar to the MW's. Relative to the other dwarf galaxies, [O/Mg] and [Si/Mg] are nearly indistinguishable, but [Ca/Mg] is slightly depressed, perhaps because Ca has a larger Type Ia SNe contribution and the Type Ia enrichment of GSE is lower as shown by its depressed [Fe/Mg].

4.3.2. Carbon and Nitrogen

Unlike the MCs, the [(C+N)/Fe] abundances of the majority of GSE stars are flat across nearly the entire metallicity range, with some of the more metal-poor stars scattering to higher values of [(C+N)/Fe]. The [(C+N)/Mg]–[Mg/H] abundance pattern of GSE is a metal-poor extension of the MW high-α sequence (perhaps best seen in the upper-right panel of Figure 7), with the GSE abundance pattern perhaps being slightly enhanced by $\sim$0.05 dex, but still deficient as compared to the other dwarf galaxies.

4.3.3. Aluminum and Nickel

Aluminum is one of the elements that the literature has often used to select out what were then referred to as "accreted halo" stars from MW samples (e.g., Hawkins et al. 2015), and the [Al/Fe]–[Fe/H] abundance patterns of GSE presented here show that the GSE stars with [Fe/H] >-1.2 are $\sim$0.2–0.3 dex deficient from the MW. This deficiency is shared by the other dwarf galaxies, although the [Al/Fe]–[Fe/H] abundance patterns of the dwarf galaxies differ slightly in shape from each other. However, the [Al/Mg]–[Mg/H] abundance

patterns emphasize that the differences among the dwarfs are again driven by differences in Fe rather than differences in Al, as nearly all dwarf galaxies share the same [Al/Mg] abundance pattern. Their trends remain substantially below an extension of the MW [Al/Mg] trend.

Similar to the α-elements, the [Ni/Fe]–[Fe/H] abundance pattern is slightly deficient ($\sim$0.05 dex from the most metal-rich stars) as compared to the MW abundance pattern, but still enhanced as compared to the other dwarf galaxies ($\sim$0.05 dex). The [Ni/Mg] abundance of GSE is closer to the pure Type II abundance ratio of the MW high-α disk, slightly below that of the other dwarf galaxies.

4.3.4. Cerium

The [Ce/Fe]–[Fe/H] abundance pattern of GSE is similar to the other dwarf galaxies. However, the [Ce/Mg]–[Mg/H] abundance plots show that at fixed [Mg/H], GSE is slightly deficient in [Ce/Mg] ($\sim$0.10–0.15 dex) as compared to the other dwarf galaxies.

4.3.5. GSE Interpretations

The relatively simple α-element abundance patterns can be explained by Type II SNe dominating at low metallicities, before Type Ia SNe exploding after some time delay, diluting the α-elements as Fe is added to the ISM in large quantities (e.g., Tinsley 1979). Whatever extended star formation GSE might have had was cut off by its proximity to the MW. As such, we see no sign of flat or increasing α-element abundance patterns suggesting a starburst like the MCs, or any extended SFH. However, the fact that GSE was α-element enhanced until [Fe/H] ~ -1.2 shows that the early SF of this galaxy was much more efficient than the early SF of the MCs, which were α-element enhanced until [Fe/H] ~ -2.2. This difference in star formation history also results in slightly enhanced [Al/Fe]–[Fe/H] and [Ni/Fe]–[Fe/H] abundance patterns as compared to the other dwarf galaxies, but these differences are largely driven by the "extra" Fe from the increased relative contribution from Type Ia SNe in the other dwarf galaxies.

The slight deficiencies observed in [Ce/Mg] and [(C+N)/Mg] observed for GSE suggest that GSE had slightly lower contributions from AGB stars to its evolution as compared to these galaxies. This is expected if GSE only evolved over the course of 2–4 Gyr, before large amounts of AGB stars could contribute to its evolution.

4.4. Sgr

The chemistry of the Sgr dwarf has been studied by numerous authors (e.g., Chou et al. 2007; Sbordone et al. 2007; McWilliam et al. 2013; Hasselquist et al. 2017; Carlin et al. 2018; Hansen et al. 2018), with Hayes et al. (2020) analyzing the largest sample of main body and stream stars using APOGEE DR16. In general, these analyses all find the [X/Fe] abundances of the more metal-rich stars in the Sgr main body to be below the MW abundance trends. Interpretations of such subsolar abundance ratios range from high Type Ia/Type II SNe ratio to top-light IMF. Here we analyze a sample of stars that is essentially an expanded sample of Hayes et al. (2020).

While a detailed analysis of the spatial dependence of the chemical abundance patterns of Sgr is beyond the scope of this work, we find that the Sgr stream sample is $\sim$0.5 dex more metal-poor than the main body sample (see, e.g., Hayes et al. 2020).

However, we verify that stars with similar metallicities between the two samples have near-identical chemical abundance patterns (see Appendix A.3 for more details).

4.4.1. O, Mg, Si, and Ca

The α-elements in Sgr smoothly decline from $-2.5 <$ [Fe/H] < -0.9, going from the MW "halo" high-α plateau at the metal-poor end to below the MW low-α "thin" disk trend at [Fe/H] $= -0.9$. Sgr begins this decline at a slightly higher metallicity than the MCs, but a lower metallicity than GSE. At [Fe/H] >-0.9, the [O/Fe], [Si/Fe], and [Ca/Fe] abundances are nearly flat at solar or slightly subsolar values, but the [Mg/Fe] abundance shows a slight increase followed by a decrease, as also observed in the SMC. The [α/Fe] abundance of Sgr at [Fe/H] >-0.9 remains $\sim$0.1 dex below the LMC trend and MW low-α sequence.

While Sgr extends to slightly higher values of [Fe/H] than the LMC, both galaxies enriched to nearly the same level of [Mg/H], with the Sgr abundance trend being deficient in [Fe/Mg] as compared to the MCs at [Fe/H] >-1.0, but enhanced at [Fe/H] >-1.0. The Sgr stars with [Mg/H] >-0.5 are very slightly enhanced in [Ca/Mg] as compared to the LMC, but otherwise the [Ca/Mg], [O/Mg], and [Si/Mg] patterns are nearly identical to those of the LMC.

4.4.2. Carbon and Nitrogen

The [(C+N)/Fe]–[Fe/H] abundance pattern of Sgr is similar to that of the LMC. The increase in [(C+N)/Fe] occurs at [Fe/H] $\simeq -0.8$ for both galaxies, but the slope of the increase with [Fe/H] is shallower in Sgr than the LMC, so the sequences diverge at higher [Fe/H].

At [Mg/H] >-0.7, the Sgr [(C+N)/Mg] abundance trend is $\sim$0.05 dex above the LMC trend, with the most metal-rich Sgr stars intersecting the MW low-α trend, showing that at these metallicities, Sgr formed stars with an AGB/Type II SNe ratio that was closer to that of the MW low-α disk.

4.4.3. Aluminum and Nickel

The [Al/Fe] abundance pattern of Sgr is $\sim$0.4 dex below the MW trend at [Fe/H] >-0.8. This is even more deficient than the other galaxies mentioned thus far. However, as shown in the [Al/Mg] abundance plane in Figure 6 and in Figure 7, the Sgr [Al/Mg]–[Mg/H] abundance pattern is nearly indistinguishable from the other dwarf galaxies, with both the LMC and Sgr remaining noticeably deficient ($\sim$0.2 dex) compare to the MW in [Al/Mg] at [Mg/H] >-0.7.

The [Ni/Fe]–[Fe/H] pattern of Sgr largely follows that of the LMC, but it continues to decline at [Fe/H] >-0.9, at which point the LMC [Ni/Fe]–[Fe/H] abundance patterns becomes flat/slightly increasing. The [Ni/Mg]–[Mg/H] pattern of Sgr at [Mg/H] >-0.8 lies in between the MW low-α sequence and the LMC. The [Ni/Mg] differences follow the [Fe/Mg] differences, which suggests that they are driven by differing levels of Type Ia SNe enrichment.

4.4.4. Cerium

The [Ce/Fe]–[Fe/H] abundance pattern of Sgr is similar to those of the other galaxies, with the most metal-rich Sgr stars being enhanced in [Ce/Fe] as compared to the MW stars. The median tracks in Figure 7 show that the most metal-rich Sgr

stars are slightly enhanced in [Ce/Mg] as compared to the LMC, and moderately enhanced (∼0.2 dex) as compared to the MW.

4.4.5. Sgr Interpretations

The α-element abundance patterns show that early on in its evolution, Sgr experienced relatively weak star formation as compared to the MW and GSE, but stronger than the MCs and Fnx. Sgr then evolved to a much higher Type Ia/Type II SNe ratio than the other dwarf galaxies, with a [Fe/Mg] ratio that is enhanced over the MCs and MW low-α sequence at [Mg/H] > −1.0. Despite this clear difference in early SFE, Sgr and LMC enrich to nearly the same levels of [Fe/H], with Sgr extending to metallicities that are ∼0.2 dex higher than the LMC. The increased early SFE and enhanced enrichment are unexpected in the paradigm of the mass–metallicity relationship (Kirby et al. 2011), as the Sgr dwarf was thought to be much less massive than the LMC. However, the two galaxies do enrich to the same level of [Mg/H], implying the tension is somewhat reduced if [Mg/H] is used to track metallicity instead of [Fe/H]. To more accurately analyze where these two galaxies lie on the mass–metallicity relationship, we would need to better account for selection biases, which is beyond the scope of this work. Both the final metallicity and the early SFE seem to show Sgr behaving as though it were a fairly massive dwarf galaxy.

The flat, or near-flat in the case of Mg, [α/Fe]–[Fe/H] abundance patterns at [Fe/H] > −0.9 imply that Sgr did experience some extended SF, with an increase in Mg from Type II SNe preventing the [Fe/Mg] abundance from rising further. This extended star formation event could have been started as Sgr began falling into the MW. As shown in Hayes et al. (2020), the Sgr stream does not contain stars with [Fe/H] ≳ −0.50, but the Sgr [α/Fe] abundance becomes flat with increasing [Fe/H] at [Fe/H] ∼ −0.9. So the extended star formation occurred before some stars were stripped as well as after, plausibly corresponding with pericenter passages through the disk of the MW (see also Ruiz-Lara et al. 2020a).

The low [Ni/Fe] in Sgr was interpreted as evidence for a top-light IMF in some literature works (e.g., Hasselquist et al. 2017). However, analyses of MW median abundance trends imply that Type II SNe contribute a larger fraction of Ni than of Fe (Weinberg et al. 2019), so this deficiency could also arise from differences in the Type Ia/Type II SNe ratios. Both the [Ni/Fe] and [Al/Fe] abundance patterns can largely be attributed to Sgr evolving to a higher Ia/II ratio than the MW and MCs, increasing the amount of Fe in Sgr. However, Sgr shares the peculiar deficiency relative to the MW in [Al/Mg] at [Mg/H] > −0.5, which is plausibly explained by more metal-poor Type II SNe contributing to the enrichment than the metallicity of those SNe that contributed to the Al enrichment in Sgr, perhaps because of its lower SFE.

The [(C+N)/Mg] and [Ce/Mg] abundance patterns imply that Sgr had more contribution from AGB stars to its enrichment than the LMC and the MW. This is perhaps an expectation given the higher Type Ia/Type II SNe ratio in Sgr, as implied by the other abundance patterns, allowing for a stronger AGB contribution as well.

4.5. Fnx

The abundances of Fnx have been studied in a variety of literature studies, some of which are comparable in number to what we have in APOGEE. In general, these studies find that Fnx exhibits a relatively metal-poor α-element abundance "knee" (e.g., Hendricks et al. 2014), with sub-MW [α/Fe] abundance ratios at [Fe/H] > −1.5 (e.g., Letarte et al. 2010; Hendricks et al. 2014). These studies suggest Fnx underwent some extended SFH and formed stars from gas with a larger Type Ia/Type II SNe ratio than the MW at similar metallicity. The APOGEE data, shown in the right columns of Figures 5 and 6, contains Fnx stars with −2.2 < [Fe/H] < −0.5. However, because the Fnx sample is generally lower in S/N as compared to the other galaxies, most of our analysis is focused on the Fnx stars with [Fe/H] > −1.2, as the stars more metal-poor than this have larger abundance uncertainties. The APOGEE Fnx sample is also relatively sparse at low metallicity, consisting of ∼20 stars with −2.2 < [Fe/H] < −1.2.

4.5.1. O, Mg, Si, and Ca

While it is difficult to analyze the metal-poor "knee" of Fnx using this APOGEE sample, the α-element abundances decline from −2.2 < [Fe/H] < −1.2. This is a similar range of decrease as the MCs, although Fnx reaches a much more deficient [α/Fe] abundance at [Fe/H] = −1.2 than the MCs (∼0.2 dex deficient). At [Fe/H] > −1.2, there is a slight increase in the α-element abundances, with the most metal-rich Fnx stars reaching the same [α/Fe] abundance of the Sgr stars at [Fe/H] > −0.8.

The exceptionally low [Mg/Fe]–[Fe/H] manifests as an exceptionally enhanced [Fe/Mg]–[Mg/H] abundance pattern, where for fixed [Mg/H], Fnx is ∼0.2 dex enhanced in Fe from the MCs, ∼0.3 dex enhanced from GSE, and ∼0.4 dex enhanced over the MW high-α sequence. Fnx is also enhanced in [Ca/Mg] relative to the other galaxies at [Mg/H] < −1.0, but is nearly identical to the other galaxies in [O/Mg] and [Si/Mg].

4.5.2. Carbon and Nitrogen

Like the other galaxies, Fnx shows a slight increase in [(C+N)/Fe] with [Fe/H] at [Fe/H] > −1.0, but even the most metal-rich Fnx stars remain ∼0.3 dex below the MW trend. At fixed [Mg/H], Fnx is the most enhanced galaxy in [(C+N)/Mg], with an abundance that is ∼0.1 dex above the MCs and Sgr over the range −1.5 < [Mg/H] < −1.0.

4.5.3. Aluminum and Nickel

Despite having the most deficient [Al/Fe]–[Fe/H] pattern of all of the galaxies, the Fnx [Al/Mg] is nearly identical to the other dwarf galaxies. Fnx is also most deficient in [Ni/Fe], with [Ni/Fe] ≃ −0.1 dex across much of the metallicity range, ∼0.1 dex below the MCs and Sgr, although the most metal-rich Sgr stars reach nearly this low [Ni/Fe] abundance. The [Ni/Mg] abundance of Fnx is enhanced compared to GSE and the high-α MW sequence, but about the same as the MCs and Sgr, at least at [Mg/H] > −1.5.

4.5.4. Cerium

The [Ce/Fe]–[Fe/H] abundance pattern of Fnx largely traces those of the other galaxies, although Ce is only measurable for
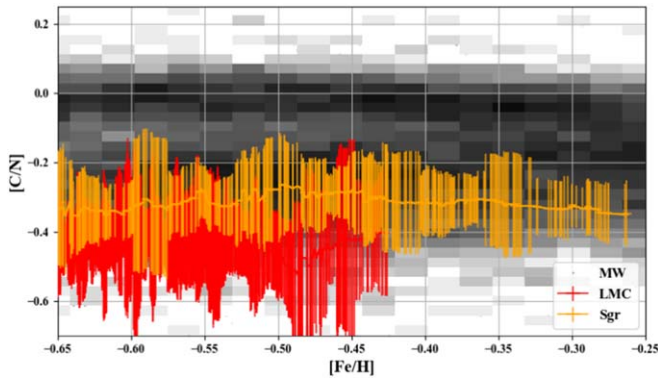
Figure 8. [C/N] as compared to the MW just for Sgr (orange) and LMC (red). Running medians of 30 stars per bin are shown for the dwarf galaxies, along with the standard deviation in each bin. The MW sample is plotted as a gray-scale density image.

$\sim$40% of the Fnx sample. At $-1.4 < [Mg/H] < -1.0$, Fnx is 0.2–0.4 dex enhanced in [Ce/Mg] relative to the other dwarf galaxies, and 0.5 dex enhanced relative to the MW high-α sequence. This level of enhancement in Fnx at $[Mg/H] = -1.0$ is similar to that of the MW low-α sequence at $[Mg/H] \sim -0.2$.

4.5.5. Fnx Interpretations

Fnx is the most striking outlier among the five dwarf galaxies, in [O/Fe], [Mg/Fe], [Si/Fe], [Ni/Fe], [(C+N)/Mg], [Ca/Mg], and to a lesser extend, [Ce/Mg]. Possibly these differences could imply different IMF-averaged yields from Fnx stars, e.g., Type II SNe that produced more Fe relative to α-elements. Another possibility is winds that preferentially ejected Type II SNe products. Or, Fnx could simply have an SFH that led to an exceptionally high ratio of Type Ia/Type II SNe enrichment. A high relative contribution of Type Ia SNe could explain most of these anomalies, and a similarly high contribution of AGB enrichment could explain high [(C+N)/Mg] and [Ce/Mg] ratios.

4.6. [C/N] as an Age Indicator

As has now been shown in many works (e.g., Masseron & Gilmore 2015; Martig et al. 2016; Ness et al. 2016; Hasselquist et al. 2019), we can use the APOGEE [C/N] abundance ratio as a mass/age indicator for APOGEE red giant stars. More massive stars mix a larger amount of CNO-processed material into their convective envelopes when ascending the RGB, which lowers their [C/N] abundance ratio because C is depleted and N is enhanced during CNO burning. However, the [C/N] abundance is only a reliable mass indicator at $[Fe/H] \gtrsim -0.6$, below which some extra mixing occurs to further alter the [C/N] abundance (see, e.g., Shetrone et al. 2019). We therefore limit the following [C/N]-age analysis to these metallicities, meaning that we only study the [C/N] abundance patterns of the more metal-rich LMC and Sgr stars.

In Figure 8 we show how the [C/N] abundance tracks of these two galaxies as compared to those of the MW, again selecting an MW comparison sample of $3600\,K < T_{\rm eff} < 4200\,K$ to remove the effects of potential $T_{\rm eff}$ systematic uncertainties on abundance determination. As was done in Figure 7, we calculate medians in bins of 30 stars, and plot those medians as well as the standard deviations.

From Figure 8 we see that the Sgr stars show a [C/N] abundance pattern that falls in the same region of this abundance space as the MW low-α or "thin" disk stars ([C/N] $\simeq -0.3$). This suggests a median age of the stars at these [Fe/H] of 3–6 Gyr (e.g., Bensby et al. 2014; Martig et al. 2016; Ness et al. 2016). This age estimate of the metal-rich Sgr stars is qualitatively consistent with the "intermediate age metal-rich population" described in Alfaro-Cuello et al. (2019), who found that the stars in their sample corresponding to metal-rich Sgr stars had a mean metallicity of $[Fe/H] = 0.29 \pm 0.16$ and mean age of 4.28 ± 1.16 Gyr. The LMC stars, on the other hand, have median [C/N] abundances that are below the Sgr trend by 0.2–0.3 dex across the entire metallicity range. This implies an age of these stars of <3 Gyr. However, the larger standard deviation in these bins implies an age range at fixed metallicity, one that is potentially spatially dependent.

While we do not explicitly map to age in this work, Hasselquist et al. (2020) derived ages for a few of these metal-rich stars and found a median age of the LMC stars of 2 Gyr, and a median age of the Sgr stars of 5 Gyr. Additionally, J. Povick et al. (2021, in preparation) derive ages for these stars and find that most stars with $[Fe/H] > -0.5$ are younger than 2 Gyr. This is consistent with the results of the α-element abundances presented above and in Nidever et al. (2020), which highlight that the metal-rich LMC stars likely formed in a recent burst of star formation. This picture is also consistent with literature studies of the SFH of the LMC (e.g., Harris & Zaritsky 2009; Weisz et al. 2013; Monteagudo et al. 2018; Ruiz-Lara et al. 2020b; Nidever et al. 2021). Our interpretation presumes that the birth [C/N] ratios of the metal-rich Sgr, LMC, and low-α MW sequence are similar such that these differences in [C/N] reflect differences in dredge-up materials that in turn reflect differences in stellar mass.

4.7. Chemical Abundance Summary

The α-elements, O, Mg, Si, and Ca, show that out of all these dwarf galaxies, GSE had the highest early SFE, followed by Sgr, then the MCs. Our Fnx sample does not contain enough metal-poor stars to precisely place its early SFE in comparison to the other galaxies, but we do find that Fnx evolved to the highest Type Ia/Type II SNe ratio, with a [Mg/Fe] abundance that is $\sim$0.15 dex below the MCs and Sgr at $[Fe/H] = -1.2$. All galaxies except for GSE show a flattening or even increase in their α-element abundance pattern ([α/Fe]), suggesting an extended star formation event that polluted the ISM with many more Type II SNe. The LMC had the strongest second star formation event, which actually slightly enhanced the [α/Fe] abundance patterns. The [C/N] abundance patterns suggest that this strong second star formation event occurred at more recent times than the second star formation epoch in Sgr.

All of the dwarf galaxies are deficient in [Ni/Fe] to some level as compared to the MW, with GSE being slightly deficient ($\sim$0.1 dex at most) and Fnx being the most deficient ($\sim$0.35 dex at most). However, the fact that the [Ni/Mg] abundances of these galaxies are below the MW low-α sequence suggests that there is some metallicity dependence on the production of Ni, since the enhanced Type Ia/Type II SNe ratio implied by the α-element abundance pattern does not result in an enhanced [Ni/Mg] abundance. Another plausible explanation of deficient [Ni/Fe] is the contribution of sub-Chandrasekhar Type Ia SNe to the chemical enrichment of a galaxy (e.g., McWilliam et al. 2018; Hill and Skúladóttir et al.

2019; Kirby et al. 2019), although Kirby et al. (2019) find minimal evidence for this in the dwarf galaxies that had extended SFHs (e.g., Fnx), favoring the metallicity-dependent production of Ni as the explanation for the abundance patterns presented here.

More metal-poor SNe is also a plausible explanation for the deficient [Al/Mg] abundances of the dwarf galaxies, with the stars forming at [Mg/H] > -0.7 forming from gas that was polluted preferentially by lower metallicity SNe than the MW sequences, which evolved much quicker.

The [(C+N)/Mg] and [Ce/Mg] abundance patterns show that all dwarf galaxies had higher contributions to their evolution from AGB stars than the MW high-α sequence. Compared to each other over the metallicity range -1.5, $< [Mg/H] < -1.0$, GSE had the weakest contribution from AGB stars, followed by Sgr, then the MCs, and finally Fnx. Only the LMC and Sgr evolved substantially past [Mg/H] $= -1.0$, at which point the relative AGB contribution to their chemical enrichment diverged, with the LMC experiencing an increase in Mg from the strong starburst.

From these chemical abundance comparisons, we find evidence that galaxies in denser environments undergo high-efficiency formation events early on in their histories. Conversely, more isolated galaxies have very low-efficiency star formation events early on, and form apparently large fractions of their stars as a result of interactions: Sgr with the MW (e.g., Ruiz-Lara et al. 2020a), MCs interacting with each other, and Fnx with a small merger (e.g., Coleman et al. 2005; Leung et al. 2020).

5. Chemical Evolution Modeling

In this section, we implement chemical evolution models to infer the physical parameters of the SFHs of these galaxies. Note that we are using these tools to estimate the SFHs of these galaxies using the APOGEE chemistry alone. This allows us to quantify the relative strengths of the starbursts of the LMC and SMC, for example. While we do compare these SFHs to photometric studies in Section 6.2, a much more quantitative and robust analysis of these data can be done in which the photometry is combined with the spectroscopic abundance data, resulting in much tighter constraints of the SFHs. This analysis is beyond the scope of this work.

To extract parameters of the SFHs of each galaxy, we adopt two chemical evolution codes: flexCE (Andrews et al. 2017) and the model described in Lian et al. (2018) and Lian et al. (2020b), hereafter referred to as "the Lian model".

While the models are similar at a fundamental level, there are several distinct differences (explained in detail in Appendix B) that make the inclusion of both of them valuable. First, the flexCE model was tuned in its yields and fiducial parameters to match the APOGEE [O/Fe]–[Fe/H] abundance pattern (which tracks very closely to [Si/Fe]; see Andrews et al. 2017). O is an α-element with nucleosynthetic yields that are thought to be well understood (e.g., Kobayashi et al. 2006). However, the APOGEE O abundances are not as well measured across the Hertzsprung–Russell diagram as Si abundances are. Therefore, we only fit flexCE model tracks to [Si/Fe]–[Fe/H] abundances. The Lian model, on the other hand, has been tuned to fit the APOGEE [Mg/Fe]–[Fe/H] abundance plane.

The model codes are also parameterized differently, which we describe both below and in Appendix B. Results of the modeled SFHs are shown and discussed in Section 5.3. In all

Table 3
FlexCE Fixed Parameters (Section 5.1 and Appendix B)

System Name	Initial Gas Mass M_0 ($M_\odot$)	Inflow Mass Scale M_i ($M_\odot$)	Inflow Timescale τ_i (Gyr)	Burst Duration σ_b (Gyr)	Burst Strength F_b
LMC	3×10^9	6×10^{10}	2	0.75	⋯
SMC	3×10^9	6×10^{10}	2	0.75	⋯
Sgr	3×10^9	6×10^{10}	1	⋯	0.01
GSE	3×10^9	6×10^{10}	2.5	⋯	⋯
Fnx	3×10^9	6×10^{10}	1	⋯	0.01

cases where we consider bursts of star formation, we implement them as time-localized changes to the SFE, with a smooth gas accretion history. The effects of efficiency-driven starbursts and accretion-driven starbursts on chemical evolution are somewhat different (see, e.g., Johnson & Weinberg 2020). For satellite galaxies, efficiency-driven bursts caused by dynamical interactions seem the somewhat more natural choice, as the smaller gravitational potential of lower-mass satellite galaxies reduces their chance of accretion-driven starbursts.

5.1. FlexCE Modeling

FlexCE is a one-zone, open-box chemical evolution modeling code that is broadly described in Andrews et al. (2017), which also provides a fiducial model designed to fit the MW's [O/Fe]–[Fe/H] chemical abundance pattern for stars in the solar neighborhood. Naturally, dwarf galaxies are expected to have different SFHs than the MW, so many of these parameters must be changed to produce appropriate dwarf galaxy chemical evolution models. However, we have kept some of the fiducial parameters, because they are thought to vary less from galaxy to galaxy or to be driven by stellar evolution rather than galactic evolution.

For example, we retain the fiducial parameters for the chemical abundance yields, Type Ia supernova delay-time distribution (which appears to be constant across massive galaxies at least, Walcher et al. 2016), and the IMF. Andrews et al. (2017) use a Kroupa IMF (Kroupa 2001) for their MW model. While some past studies have speculated that individual dwarf galaxies may have had a more top-light IMF (e.g., Carlin et al. 2018), other studies have refuted these claims when observing lower metallicity stars (Hansen et al. 2018). Any parameters not mentioned below or given in Tables 3 and 4 use the fiducial values from Andrews et al. (2017).

There are two general modifications we make to the fiducial flexCE model. (1) We use a delayed-τ model for the gas inflow of our chemical evolution models (motivated by cosmological simulation; e.g., Simha et al. 2014), allowing the gas inflow to ramp up at early times in the universe before peaking and falling off at later times. (2) We add a formulation for a time variable SFE to flexCE, that scales the SFE up or down in a Gaussian-shaped deviation from a constant SFE. This addition allows us to temporarily cut off star formation or produce a burst of star formation in our models. More information about these modifications and how they were implemented can be found in Appendix B.1 and B.2 for the inflow and SFE, respectively.

With these modifications we model the chemical abundances of our five galaxies. Because there are many parameters that

Table 4
FlexCE Variable Parameters' Model Grid Ranges (Section 5.1 and Appendix B)

System Name	SFE (Gyr^{-1})	Outflow η_{wind}	Burst Time τ_{b} (Gyr)	Burst Duration σ_{b} (Gyr)	Burst Strength F_{b}
Model Grid					
LMC	0.01−0.03	2–10	8–12	⋯	4–8
	($\Delta = 0.005$)	($\Delta = 2$)	($\Delta = 1$)		($\Delta = 1$)
SMC	0.006–0.01	5–25	6–11	⋯	2–10
	($\Delta = 0.001$)	($\Delta = 5$)	($\Delta = 1$)		($\Delta = 2$)
Sgr	0.02–0.06	12.5–22.5	4–8	0.25–1.25	⋯
	($\Delta = 0.01$)	($\Delta = 2.5$)	($\Delta = 1$)	($\Delta = 0.25$)	
GSE	0.08–0.2	1–11	⋯	⋯	⋯
	($\Delta = 0.01$)	($\Delta = 1$)			
Fornax	0.01–0.05	20–120	2–8	1–6	⋯
	($\Delta = 0.01$)	($\Delta = 20$)	($\Delta = 1$)	($\Delta = 1$)	
Best Fit					
LMC	0.015	2	11	⋯	6
SMC	0.008	10	7	⋯	4
Sgr	0.03	17.5	5	0.5	⋯
GSE	0.14	6	⋯	⋯	⋯
Fornax	0.03	100	6	5	⋯

can produce variation in chemical evolution models, we have chosen to vary only the parameters that most strongly impact the chemistry (other than yields), and we use slightly different strategies for different galaxies. For simplicity of modeling each system we limit the number of variable parameters to four and fix the remaining parameters at the values shown in Table 3.

For each system we allow the SFE and outflow mass loading factor to differ, which control much of the global chemical abundance patterns that are produced. The flexCE outflow parameterization assumes that enriched ISM gas is ejected proportionally to the star formation rate, with the mass loading factor, η, as the constant of proportionality (Andrews et al. 2017). This is a relatively simple form for outflow, but allows the model to generally track gas outflows due to stellar sources, such as stellar winds, supernovae, stellar radiation pressure, etc. In addition to these parameters we add a time variable SFE for all galaxies except GSE, since we do not see any complex features in its chemistry.

For the LMC and SMC, because we see a bump or rise in the chemical abundance patterns that we believe is due to a recent burst of star formation, we fit these systems by adding an increase in star formation that has a variable timing and strength, with a fixed duration of $\sigma_b = 750$ Myr, roughly the duration of the increase in SFR modeled for the LMC in Nidever et al. (2020).

Some literature works found that Sgr and Fnx have had a generally bursty star formation history, with periods of star formation broken up by periods where there is very little star formation (see, e.g., Siegel et al. 2011 for Sgr and e.g., Hendricks et al. 2014 for Fnx). To reproduce this type of variable star formation we model these systems with a decrease in SFE to 1% of its baseline value, with the time and duration of this decrease as free parameters.

For all five galaxies we fix the initial gas mass and inflow mass scale and use the same values across all galaxies. While these galaxies do not have the same masses, the overall mass

scale (i.e., total mass) does not impact the chemistry, and only the ratio of initial-to-inflow mass impacts the chemistry. However, the initial gas mass has a minor effect that is largely degenerate with other parameters we vary, so we have held this ratio constant for all galaxies.

We also fix the inflow timescale of each galaxy's model, which has some impact on the chemistry, particularly the shape of the α-knee, but we consider this a secondary effect, and defer it to future study. For GSE, the SMC, and the LMC, the timescale has been fixed to a value that roughly fits the shape of the α-knee and is early enough so that most of the accretion happens before the range of starburst timings probed in the SMC and LMC. Similarly for Sgr and Fnx we use a slightly earlier inflow timescale so that most gas is accreted before the range of timescales for the stalls in star formation that we fit.

Then for each galaxy, we produce a grid of chemical evolution models with the variable parameters mentioned above. We initially test a broad range of parameters before narrowing them to the final grids used here. At a minimum we require five grid steps in each dimension, but have expanded the initial grids in dimensions where the best-fit value lay near a grid edge to confirm the validity of the best-fit results. The values of the grid points and their spacings are listed in Table 4, and parameters that are not varied are marked by "⋯" with values listed in Table 3.

To fit our models, we compute the χ^2 of each model's resulting [Si/Fe]–[Fe/H] track relative to the data for each system. As previously mentioned, Si is used for this fitting, because it is both precisely measured by APOGEE (Jönsson et al. 2020) and has well understood nucleosynthetic yields that can match MW chemical abundance patterns (Andrews et al. 2017). To obtain the χ^2 of each model we first calculate the model χ^2 using the distance of each observed star from the model track in [Si/Fe]–[Fe/H] space and the magnitude of the star's [Si/Fe] and [Fe/H] uncertainties in that direction. We then also penalize models that evolve past the maximum metallicity of each system with an extra term to the model χ^2 that is the distance of each model time step from the high-metallicity end of each galaxy scaled by the typical abundance uncertainties at those metallicities. We only turn off this penalization for GSE because we know that its star formation was cut off after some time (which we use as a check on our chemical evolution model for GSE), and for the last 1 Gyr of evolution in the remaining galaxies, because we would not expect to observe RGB stars of such young age.

To find the optimal solution for each of our fit parameters, we then take the model with the minimum χ^2 as our best fit. The best-fit values of each parameter can be found in Table 4 for our five galaxies.

5.2. Lian Modeling

The Lian chemical evolution model is a one-zone, open-box model that considers the metal production and depletion by star formation, gas accretion, and galactic winds. The star formation rate is determined from the gas mass following the form of the Kennicutt–Schmidt star formation law (SFL; Kennicutt 1998), assuming a Kroupa IMF (Kroupa 2001). The SFE is thus regulated by the coefficient of the SFL; we assume a constant coefficient (C_{initial}) unless a starburst event occurs. A different version of this model with more flexible gas accretion and SFHs has been successfully applied to interpret the stellar chemistry observations in various components of the MW,

Table 5
Lian Variable Parameters' Model Grid Ranges (Section 5.2 and Appendix B.4)

System Name	Gas Inflow		Outflow	Starburst		
	τ_{acc}	$C_{initial}$	λ_{wind}	τ_{burst}	t_{start}	Δt
Grid						
	2, 10	$0.001 - 0.1 (\Delta \log = 0.5)$	$0 - 20 (\Delta = 5)$	-0.5 to $-8 (\Delta \log = 0.3)$	$4 - 12 (\Delta = 2)$	$1 - 6 (\Delta = 1)$
Best Fit						
LMC	10	0.01	15	-2	10	3
SMC	10	0.01	20	-1	8	1
Sgr	2	0.01	10	-4	6	4
GSE	2	0.01	5	-2	…	2
Fornax	2	0.032	20	-1	6	1

including the bulge (Lian et al. 2020c), inner disk (Lian et al. 2020a), and outer disk (Lian et al. 2020b). For more details about the nucleosynthesis prescription and development of the basic model, we refer the reader to Lian et al. (2018) and Lian et al. (2020b).

We include here two major modifications of the Lian et al. (2018) and Lian et al. (2020b) models. First, the gas inflow parameterization is simpler, with our approach assuming gas accretion to decline exponentially (compare to Section 5.1): $A(t) = A_{initial} e^{-t/\tau_{acc}}$, where $A_{initial}$ is the initial gas accretion rate and τ_{acc} is the declining timescale. In this way, the burst event is described by three parameters: the timescale (τ_{burst}), start time (t_{start}) and duration (Δt) of the SFE increase. After the burst, the coefficient of the SFL is set to decrease exponentially. Since this paper mainly focuses on the burst event, for simplicity, we fix this decreasing timescale to be 0.2 Gyr.

The outflow is characterized as in flexCE, with the strength regulated by the mass loading factor, λ. As stronger outflows remove more gas from the galaxy, to keep the present-day stellar mass predicted by various models fixed, we set the initial gas accretion rate to scale with the outflow strength, i.e., $A_{initial} \propto (1 + \lambda)$.

We have six free parameters in total: two parameters characterizing the initial gas accretion and SFHs (τ_{acc} and $C_{initial}$), three parameters describing the starburst event (τ_{burst}, t_{start}, and Δt), and one parameter determining the strength of gas outflow (λ), shown in Table 5.

We build a grid of models with each chemical evolution code and find the best-fit model through chi-squared minimization. As in flexCE, we fit only to the chemical evolution tracks and not to the density.

5.3. Chemical Evolution Modeling Results

Chemical evolution modeling results are shown in Figure 9 for flexCE and Figure 10 for the Lian model. As before, each column shows a different dwarf galaxy. The top row shows the best-fit model chemical track through the abundance pattern, the middle row shows the star formation history of that chemical track, and the bottom row shows the metallicity evolution as a function of time. We describe the results in the following subsections, and compare and contrast the model results in Section 5.4. Because the models are only parameterized with a single burst in SF after the initial SF epoch, the models are likely fitting to the most significant "burst" in a galaxy's SFH that provided the most stars with the ages that we probe with APOGEE.

5.3.1. Magellanic Clouds

The flexCE results show that strong bursts are favored to match the abundance patterns of both the LMC and SMC, although the burst in the SMC is somewhat weaker, and occurred ∼4 Gyr earlier than the burst in the LMC. The burst results in quick metallicity evolution, with the LMC enriching from [Fe/H] ≃ −0.8 to [Fe/H] ≃ −0.3 in the last 2–3 Gyr. The SMC experienced similar swift enrichment, but over a period of 5–8 Gyr ago, with the evolution much slower in the last 2–3 Gyr.

The Lian results also favor bursts in the MCs, although the bursts are more similar in relative strength between the two galaxies than the flexCE results. The Lian models also predict a "dip" in star formation that reached a minimum at 10 Gyr for the LMC and at 8 Gyr for the SMC, and show that the duration of the burst is shorter for the SMC than the LMC. Like the flexCE results, the Lian model results favor a scenario in which the SMC experienced a peak starburst ∼4 Gyr before the LMC. Also, like the flexCE models, the Lian models show that the bursts result in rapid metallicity evolution, although the metallicity evolution is more rapid than the flexCE results, and begins at [Fe/H] = −1.3 rather than at [Fe/H] = −0.8. This is at least partially due to the difference in how the two models are parameterized.

The flexCE models predict that all LMC stars with [Fe/H] ≳ −0.7 should be younger than 3–4 Gyr, and the Lian models predict the same age for stars with [Fe/H] ≳ −1.2. The [C/N] results in Section 4.6 suggest that the LMC stars at [Fe/H] > −0.6 are significantly younger than the MW thin-disk stars at the same metallicity, which is qualitatively consistent with these predictions.

5.3.2. GSE

Both models find an SFH for GSE that peaks at early times and declines. Because the gas inflow is treated differently in the two models, the flexCE models show a broader SF peak located at a slightly later time, than the Lian model. While the model tracks extend to the present day, GSE reaches [Fe/H] = −0.5 (maximum observed metallicity) ∼5 Gyr into its evolution in the flexCE models and 8–9 Gyr into its evolution in the Lian models, although the Lian models show very slow GSE metallicity enrichment beginning at ∼5 Gyr into its evolution. This is consistent with the picture that GSE merged with the MW some 8–10 Gyr ago, thus cutting off this late evolution. Our results prefer a merger some 7–9 Gyr ago.
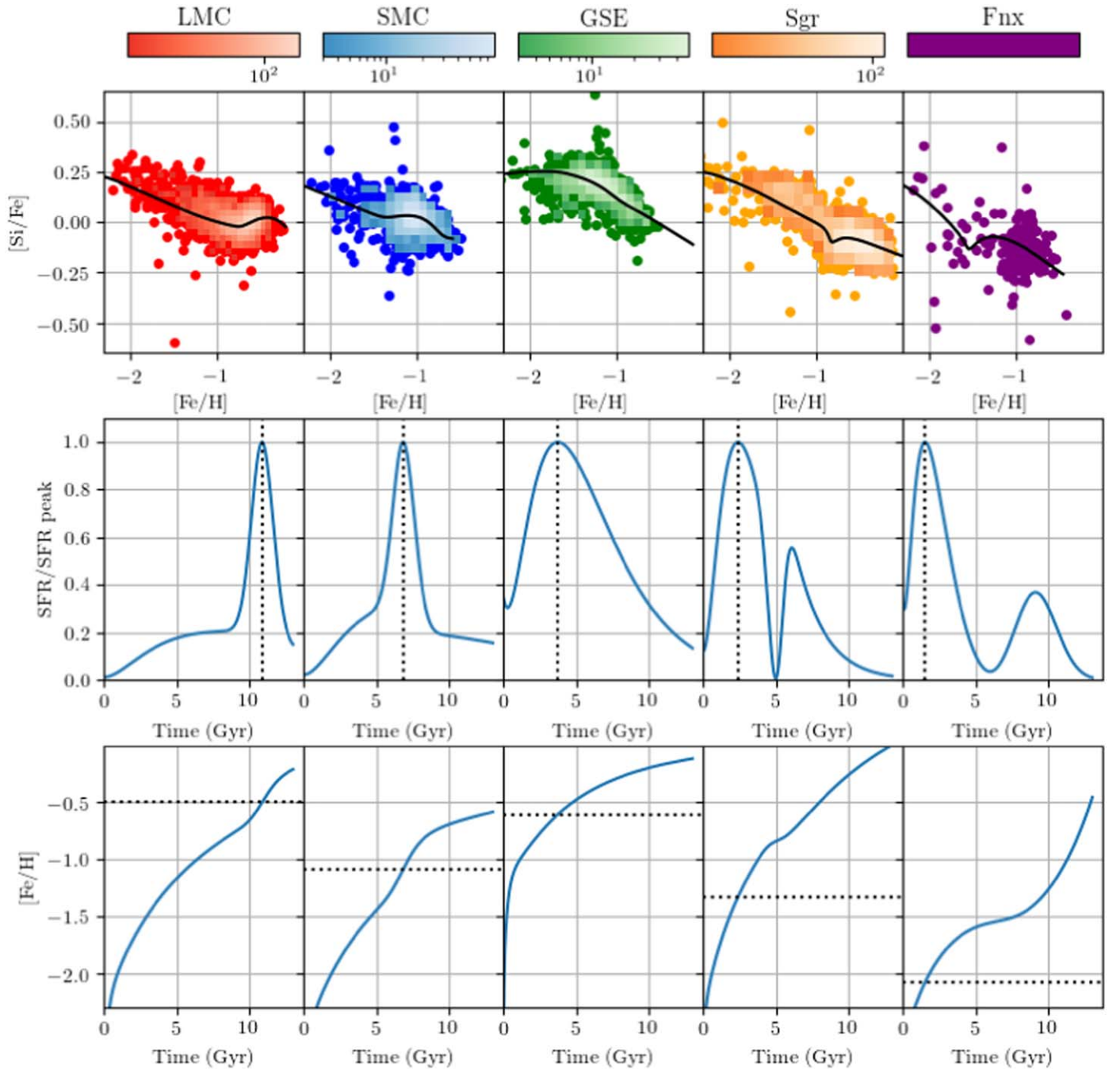
Figure 9. Top row: [Si/Fe]–[Fe/H] abundance space for each of the five dwarf galaxies, along with their best-fit chemical evolution track as inferred from the flexCE code (Andrews et al. 2017) overplotted in black. Middle row: star formation histories of each galaxy, normalized by the peak star formation rate. Vertical dotted lines indicate the time of peak SF. Bottom row: metallicity evolution with time for each dwarf galaxy. Horizontal dotted lines indicate the [Fe/H] at the peak of the SFH.

In the flexCE models, we adopt similar inflow timescales for GSE and the MCs (2.5 Gyr versus 2 Gyr), and the fit leads to a much higher (factor 10–20) SFE and thus to an SFH that peaks at much earlier times. This result is driven by the higher metallicity of the "knee" in the [Si/Fe]–[Fe/H] diagram. According to the flexCE SFH, by 5 Gyr into its evolution, GSE achieved [Fe/H] = −0.5, as compared to −1.2 and −1.5 for the LMC and SMC, respectively. The Lian models show a similar result, with GSE enriching to [Fe/H] = −0.8 5 Gyr into its evolution as compared to −1.4 and −1.55 for the LMC and SMC, respectively. Here the SFE is similar between the MCs and GSE, and the strong early SF peak in GSE arises from a

short inflow timescale. In the flexCE model, it took the LMC 10 Gyr to enrich to [Fe/H] = −0.7, which is about where GSE enriched to before merging with the MW. In the Lian model, the LMC only attained GSE metallicities at recent times, although GSE took ∼6 Gyr to reach [Fe/H] = −0.7 instead of ∼4 Gyr in the flexCE model.

5.3.3. Sgr

As described in Section 5.3, the relatively flat α-element abundance patterns at [Fe/H] > −0.8 suggest some kind of extended SFH. Both models find that a second star formation
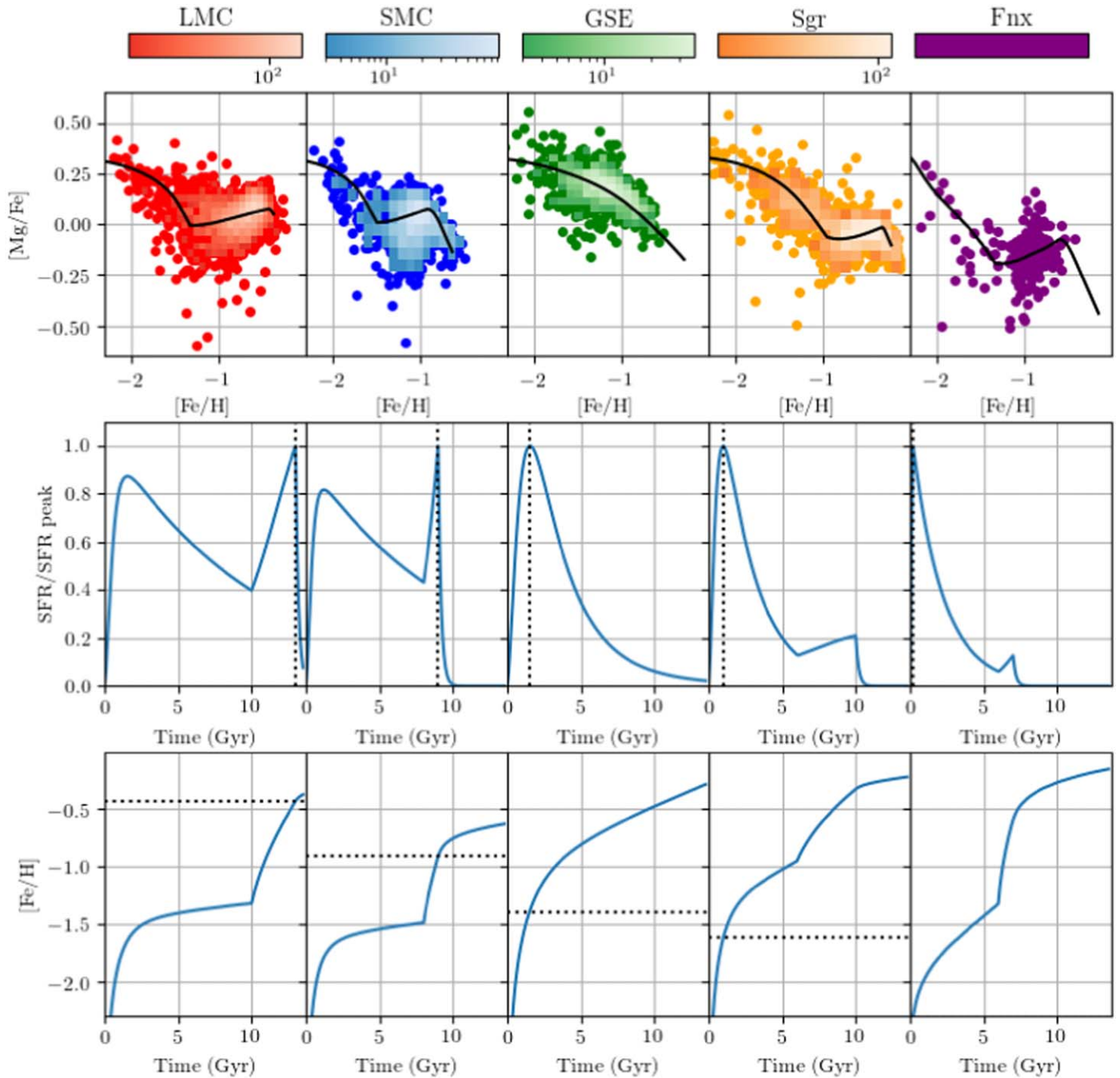
Figure 10. Same as in Figure 9, but with the Lian models that are fit to [Mg/Fe]–[Fe/H] instead of [Si/Fe]–[Fe/H].

epoch, beginning some 5–6 Gyr into its evolution and rising above the declining trend from earlier times, is required in Sgr to produce the flatter or "hooked" abundance α-element abundance pattern. Without such a secondary peak, the chemical evolution tracks show monotonically decreasing [Si/Fe] or [Mg/Fe] with increasing [Fe/H], rather than the slight flattening of the observations. In the flexCE model, the sharp minimum of star formation at 5 Gyr produces the kink in the [Si/Fe]–[Fe/H] abundance track, slightly improving the fit to the data. In both models, this second SF epoch is not as strong relative to the earlier epoch, in contrast to the MCs, and as such, the [α/Fe] ratio is not enhanced like it is in the MCs.

The early chemical enrichment of Sgr was in between GSE and the MCs in both models (e.g., intermediate SFE), with Sgr enriching to [Fe/H] = −0.7 and −1.0 5 Gyr into its evolution for the flexCE model and the Lian model, respectively. After this point, the flexCE model favors a shorter, stronger burst, compared to a more sustained, weaker burst for the Lian model. In both models, Sgr effectively stops forming stars 10 Gyr into its evolution, which is consistent with observations of Sgr that show few or no young (age < 2–3 Gyr) stars (e.g., Siegel et al. 2007), as well as the [C/N] inferences shown in Section 4.6.
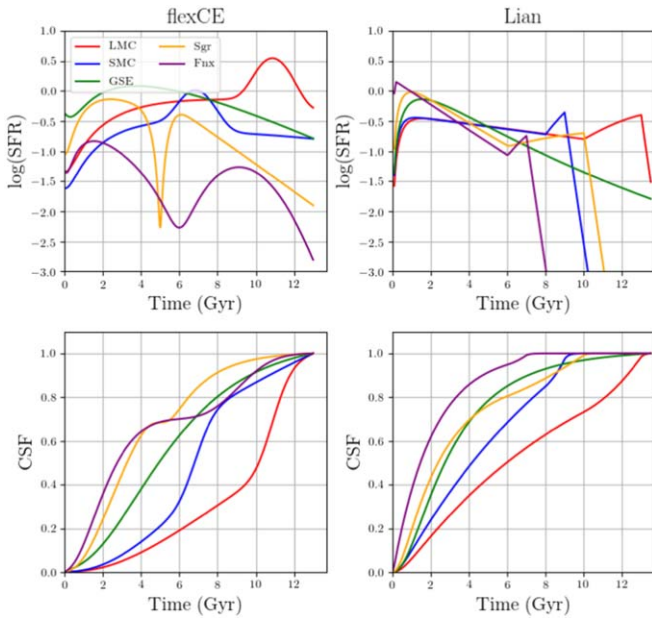
Figure 11. Comparison of the derived SFHs for the two different model sets, flexCE on the left and Lian on the right. The top rows show the SFR as a function of time, and the bottom rows show the cumulative star formation over time.

5.3.4. Fnx

As was the case for Sgr, both the flexCE and Lian models find support for a second epoch of star formation in Fnx, although this second "burst" was much weaker than the initial SF peak (~3 times weaker for the flexCE results and ~9 times weaker for the Lian model results). Even though Fnx has a much lower stellar mass than the other galaxies, both models suggest that Fnx enriched to nearly the same [Fe/H] as the SMC 5 Gyr into its evolution.

Like the MCs, Fnx is one of the galaxies where the [Mg/Fe]–[Fe/H] and [Si/Fe]–[Fe/H] patterns differ most strongly from each other, which is likely a source of at least some of the differences in results between the two chemical evolution codes.

5.4. Summary and Model Comparison

In Figure 11 we show the SFHs of each galaxy for the flexCE results and Lian model results, comparing the SFR (top row) and the cumulative star formation (bottom row). The top row of Figure 11 is useful to compare the relative shapes of the SFHs of the galaxies, but because the mass scale of the models has not been adjusted such that the final stellar mass of the model matches the observed stellar masses of each galaxy (see Section 5.1), the normalization/scaling of the SFR of each galaxy is inaccurate.

The final stellar mass of each system in the flexCE models, for example, do match the mass ordering that observations suggest, with the final stellar masses of $7.3 \times 10^9\,M_\odot$ for the LMC, $2.3 \times 10^9\,M_\odot$ for the SMC, and $3.7 \times 10^8\,M_\odot$ for Fnx. The final stellar masses of the flexCE models for Sgr, $2.0 \times 10^9\,M_\odot$, and GSE, $2.9 \times 10^9\,M_\odot$ after 5 Gyr of evolution, are also consistent in suggesting that Sgr and GSE may have been similar in mass to the SMC prior to their respective disruption (see the discussion in Section 6.1). Nonetheless we remark that the resulting final stellar masses are ~5–10 times too high compared to observational estimates (see Section 6.1 for

observed masses; but note again as mentioned in Section 5.1, the total mass scale does not impact the final chemical tracks). Therefore, a better way to compare SFHs across galaxies from the models is to use the cumulative star formation histories (CSFHs), shown in the bottom row of Figure 11.

Both sets of models show weaker early SFH for the MCs as compared to the other galaxies, and both models show that the MCs experienced peaks in SF that occurred much later than the SF peaks in the other galaxies, with the most significant period of enhanced SF in the SMC occurring ~4 Gyr before the LMC.

The model SFHs differ in the relative strengths of the bursts, with the SMC, Sgr, and Fnx all showing weaker bursts in the Lian results than the flexCE results. The Lian models also imply that GSE and Sgr each formed about 70% of their stars in the first 4 Gyr of evolution, whereas the flexCE models show Sgr forming 60% of its stars prior to this point, and GSE 40%. However, both models predict GSE evolution continuing beyond the observed tracks, and stopping them at the maximum observed [Fe/H] $\simeq -0.5$ implies truncating star formation at $t \simeq 5$ Gyr in the flexCE model and $t \simeq 10$ Gyr in the Lian model, a plausible result of disruption or ram pressure stripping by the MW. The substantially weaker burst for Fnx in the Lian models also results in nearly all stars in Fnx forming by 6 Gyr into its evolution, whereas the flexCE models find only 70% of the stars to have formed at this point.

6. Discussion

In the following section we discuss what these SFHs mean in the greater context of galaxy formation and evolution. We also compare our SFH results from chemistry alone to those derived in the literature primarily through photometry, as well as discuss future prospects.

6.1. Mass and Environmental Effects on Galaxy Evolution

The chemical abundance patterns and inferred SFHs highlight the importance of galaxy environment for chemical evolution. McConnachie (2012) and references therein tabulate the following stellar masses for the galaxies in our sample: LMC = $1.5 \times 10^9 M_\odot$, SMC = $4.6 \times 10^8 M_\odot$, Sgr (main body) = $2.1 \times 10^7 M_\odot$, and Fnx = $2.0 \times 10^7 M_\odot$. Sgr was much more massive in the past, with some studies finding masses as high as $6.4 \times 10^8 M_\odot$ (e.g., Niederste-Ostholt et al. 2010). Estimates for the stellar mass of GSE are generally in the range 3–$10 \times 10^8 M_\odot$ (e.g., Mackereth et al. 2019).

The LMC, GSE, SMC, and Sgr span about an order of magnitude in stellar mass, with the LMC being the most massive. Fnx is at least another order of magnitude less massive even than the SMC/GSE/Sgr. Despite its relatively low present-day mass compared to the other galaxies, Sgr is the most enriched dwarf galaxy, reaching slightly higher metallicities than the LMC. The SMC, GSE, and Fnx have all enriched to nearly the same metallicity, despite their vastly different stellar masses. What is very different across these dwarfs is the environments in which they formed and evolved.

Currently, these galaxies are all well inside the MW environment or have already been accreted by the MW. However, GSE is thought to have formed close to the MW and was accreted at early times (e.g., Gallart et al. 2019; Mackereth et al. 2019), Sgr and Fnx at more intermediate times (e.g., Rocha et al. 2012; Fillingham et al. 2019), and the MCs are only falling in recently, having likely evolved in near isolation

until now (e.g., Besla et al. 2016). In the paradigm of Gallart et al. (2015), in which dwarfs galaxies are assigned to two groups according to their SFH, we could consider the MCs to be "slow dwarfs," forming the bulk of their stars more recently, as compared to the "fast dwarfs" (e.g., Sgr, GSE, and Fnx) that started their evolution with a dominant early star formation event (see, e.g., Shi et al. 2020 for similar simulation results). However, even the MCs became "faster" dwarfs when they began to interact with each other driving up the α-element abundances. This suggests that proximity to any galaxy, not just a more massive MW, can be an important driver in star formation history. Had the MCs not interacted with each other, they would likely still have a lot of gas but contain far fewer stars. The inferred SFH presented here suggests that without the interactions between them, the MCs would have enriched to [Fe/H] $\simeq -0.7$ for the LMC and [Fe/H] $\simeq -1.5$ for the SMC.

There is good agreement in the literature that the MW and M31 environments have strong effects on the quenching times of infalling satellite galaxies, with many low-mass galaxies ($M_* < 10^8 M_\odot$) quenching within ~ 2 Gyr of passing through the virial radii of the host galaxies (e.g., Rocha et al. 2012; Slater & Bell 2014; Fillingham et al. 2015; Weisz et al. 2015; Wetzel et al. 2015; Akins et al. 2021). This is likely a consequence of ram pressure stripping effectively removing gas from these galaxies, preventing further star formation (see, e.g., Hester 2006; Bekki 2014; Fillingham et al. 2016). Sgr was likely just massive enough to avoid fast quenching from ram pressure stripping (e.g., Niederste-Ostholt et al. 2010), but the mass of Fnx is low enough ($M_* \sim 10^7 M_\odot$, e.g., McConnachie 2012) such that it should have been quickly quenched when entering the environment of the MW. However, the extended SFH of Fnx inferred from both the APOGEE data presented here and other literature studies can be reconciled with its low mass if the environmental quenching timescale also depends on satellite orbit. Recent studies have found that not all of these low-mass dwarfs are quenched, with the galaxies on more circular orbits and larger pericenter passages (such as Fnx) having much longer quenching timescales (e.g., Fillingham et al. 2019). Such "fortuitous" orbits have been found to enhance star formation in some simulations (e.g., Di Cintio et al. 2021), and observational evidence exists of Sgr and the MW undergoing enhanced SF epochs, coincident with Sgr pericenter passages (Ruiz-Lara et al. 2020a).

In addition to environment, the mass of a galaxy can also play an important role in its evolution. The less massive dwarf spheroidal galaxies, such as Sculptor, Draco, and Ursa Minor, have formed very few stars in recent times, and have only enriched to [Fe/H] ~ -1.0 or lower. Moreover, there is an established mass-mean metallicity relationship in the literature described in Kirby et al. (2011), with more massive galaxies enriching to a higher mean metallicity, plausibly because they are able to retain some of their gas that is ejected from SNe. Because of APOGEE selection biases, it is difficult to use the APOGEE mean metallicities to accurately place these galaxies on the mass–metallicity relationship. However, Sgr likely has a much higher metallicity for its present-day mass as compared to the SMC, and maybe even as compared to the LMC. Fnx also likely has a mean metallicity that is closer to the SMC than perhaps it should be for its mass. Conversely, another way to view the discrepancy is that the MCs, having evolved in relative isolation until recent times, are too metal-poor for their large stellar masses. While works such as Reichert et al. (2020)

and Hendricks et al. (2014) have shown that Local Group galaxies tend to exhibit correlations between their α-element enrichment and luminosity, the MCs would also be an exception to this correlation (see also Nidever et al. 2020).

Geha et al. (2012) find that nearly all field galaxies with a stellar mass$<10^9 M_\odot$ are still forming stars today. Perhaps mass is the primary fundamental driver for how enriched a given galaxy is, but galaxy–galaxy interactions can push galaxies off of this relation, either by merging and increasing the mass without too much extra star formation, or by falling into the potential of a massive galaxy, where star formation is momentarily kick-started before the galaxy is disrupted or quenched.

## 6.2. Comparison to Photometric Star Formation Histories

This work is far from the first to derive SFHs for these galaxies. However, this is among the first works to derive/ estimate SFHs from the chemical abundance patterns of multiple galaxies, applying the same model frameworks to observations from nearly identical setups. In the following section we compare the SFHs we measure above to those measured in the literature. Throughout this section we use "photometric SFHs" to refer to SFHs derived from CMDs. As described in greater detail below, these photometric SFHs can vary in precision depending on whether or not the photometry is deep enough to reach the old main-sequence turnoff (oMST; e.g., Ruiz-Lara et al. 2018). Moreover, most of the literature photometric studies for these galaxies are small, pencil-beam patches of the galaxies (typically the central regions) as compared to our samples, which cover large fractions of the entire spatial extent of these galaxies.

6.2.1. The Magellanic Clouds

There have been many photometric studies of the SFHs of the MCs. In this section we compare the MC chemical SFHs to the photometric studies of Weisz (Weisz et al. 2013, 2014; Figure 12), Harris and Zartitsky (HZ; Harris & Zaritsky 2004, 2009, Figure 13), and more recent SFHs derived from the Survey of the MAgellanic Stellar History (SMASH; Nidever et al. 2017, 2021, Figure 13). The HZ work is ground based, so is typically shallower photometry but covers much of the same spatial regions of the MCs as our data. The Weisz work is much deeper photometry from HST, but is of the central regions of the MCs. The SMASH work is both deep and covers large spatial regions of the MCs.

We find reasonable agreement between the various photometric SFHs of the LMC and what we infer from the chemical evolution models fit to the APOGEE data. In the upper-left panel of Figure 12, we find that the Weisz cumulative SFH falls between what is derived for the two models from this work for the LMC at older ages, but all three results are in agreement with the LMC forming $\sim 20\%$ of its stars in the last 2 Gyr. This is similar to the SFHs from HZ and SMASH (shown in the left panel of Figure 12), although the SMASH SFHs suggest that the LMC formed $\sim 40\%$ of its stars by 4 Gyr into its evolution, which is slightly higher than Weisz, and much higher than the $\sim 10\%$ found in the HZ work. This discrepancy is possibly due to the fact that the HZ work was not deep enough to capture the oMST, resulting in more uncertain SFRs at early times. The Lian model agrees well with the SMASH LMC SFH, and the
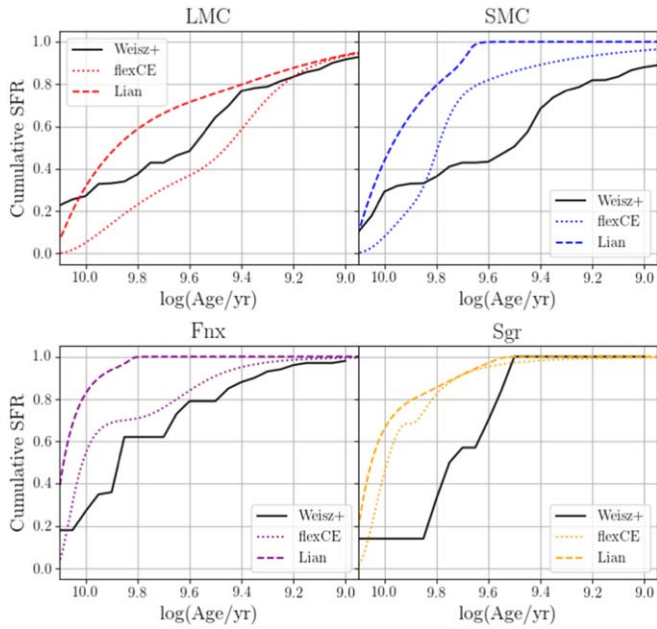
Figure 12. Comparison between the SFHs derived in this work and the SFHs derived in Weisz et al. (2013) (LMC and SMC, top row) and Weisz et al. (2014) (Fnx and Sgr, bottom row).
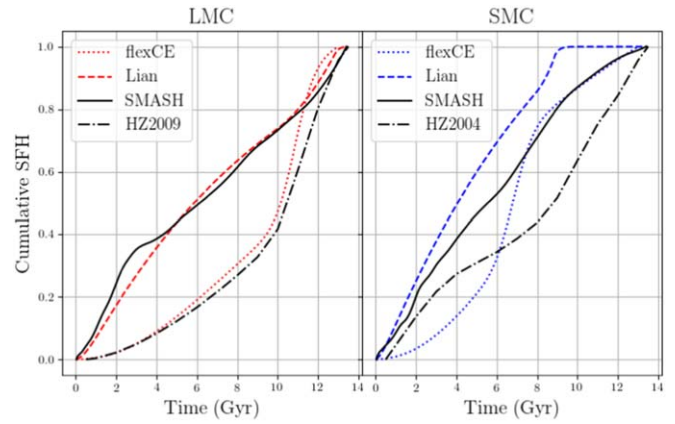

Figure 13. Comparison of our inferred cumulative SFHs to those of Harris & Zaritsky (2009, 2004), and SMASH (Nidever et al. 2021) for the LMC (left) and SMC (right).

flexCE agrees well with the Harris & Zaritsky (2009) LMC SFH.

The SFH results for the LMC derived by Monteagudo et al. (2018) are qualitatively similar to what is shown here. They find some spatial dependence of the SFH, with the bar region of the LMC forming a higher fraction of total stars at more recent times than the disk. Specifically, they find that the disk regions of the LMC formed half of their stars 7–8 Gyr into its evolution, whereas the bar had not formed half of their stars until 9–10 Gyr into the galaxy's evolution. Meschin et al. (2014) find similar results, and also that the trend of a larger fraction of stars formed at earlier times extends to the outer regions of the LMC. A detailed comparison of the spatial dependence of the SFH is beyond the scope of this work.

For the SMC, we find worse agreement in our inferred SFHs compared to the Weisz SFH than we do for the LMC (upper-right panel of Figure 12). Specifically, both models find a much larger fraction of SMC stars forming at earlier times than the Weisz et al. (2013) work. This could be in part due to the difference in spatial coverage, which is why there is a slightly better agreement with the SMASH work shown in the right panel of Figure 13, where the flexCE, Lian, and SMASH CSFHs all show that the SMC formed ~70%–80% of its stars in the first 8 Gyr of its evolution. A recent study by Rubele et al. (2018) suggests significant enhancement of SF took place in the SMC beginning 100 Myr ago. Our sample selection cuts nearly all of these stars out (see Appendix A.1), but these stars still represent a small fraction of the total stars formed in the SMC. Future analysis confirming the reliability of results for massive supergiants in APOGEE will allow for a chemical exploration of these more massive, younger stars.

6.2.2. Sgr and Fnx

We compare the Weisz Sgr and Fnx SFHs to those that we infer in the bottom row of Figure 12. The flexCE Fnx model reproduces a CSFH that is very much like what is derived in Weisz et al. (2014), with Fnx forming 20% of its stars in the last ~4 Gyr. The Lian model, with the much weaker secondary SF epoch, implies Fnx formed the vast majority of its stars by 6 Gyr ago. Support for a recent burst in Fnx can be found throughout the literature, including the recent work of Rusakov et al. (2021), who find that Fnx underwent a strong starburst some 4–5 Gyr ago, one that was close to or even exceeded the strength of the early SF event. This is more consistent with our flexCE results, which shows a nearly equal strength second burst in Fnx that peaked 4–5 Gyr ago. Hendricks et al. (2014) find chemical evidence for a starburst in Fnx, as we do here in this work, but they suggest the burst occurred at much earlier times than either the flexCE or Lian models suggest. The more spatially extended SFH work of de Boer et al. (2012) shows Fnx underwent a more gradual enrichment from 3–8 Gyr ago, enriching from $[Fe/H] = -1.5$ to $[Fe/H] = -0.5$, which is an enrichment rate that is more consistent with the flexCE results.

The Sgr comparison is shown in the bottom-right panel of Figure 12. Neither model matches well with the Weisz et al. (2014) SFH of Sgr, though they agree well with each other. This could be due to the fact that our Sgr sample contains many stream stars, whereas Weisz et al. (2014) was looking at the main body of the galaxy, where the tidal interactions have preferentially removed many metal-poor stars, including into the streams. However, all of the SFHs agree that Sgr formed nearly all of its stars by 3–4 Gyr ago. This is mostly in line with other photometric SFH studies, such as Siegel et al. (2007), although we do not find the metal-rich youngest populations that they find in the innermost regions. de Boer et al. (2015) find that the Sgr stream stars exhibit a tight age–metallicity relation, enriching to $[Fe/H] = -0.7$ by 5–7 Gyr ago, again consistent with the results of both models (see the bottom row of Figures 9 and 10). Our SFH here also qualitatively agrees with recent work by Garro et al. (2021), who analyzed the ages and metallicities of the globular cluster population of Sgr, including 12 new clusters discovered by Minniti et al. (2021). They find that Sgr formed its metal-rich ($-0.9 < [Fe/H] < -0.3$) globular clusters some 6–8 Gyr ago.

6.3. Future Prospects

We have restricted the parameter space of our chemical evolution models in part for computational practicality in this exploratory study, but also because we are constraining them

with a single observable, the [Si/Fe]–[Fe/H] or [Mg/Fe]–[Fe/H] track. In future work, we can allow greater model flexibility by simultaneously employing these observables (including more than just two chemical elements) and the photometric SFHs illustrated in Figures 12 and 13, and we can test or further constrain these models using metallicity distribution functions (MDFs). Computing MDFs from the metallicity distribution of observed APOGEE stars requires correcting for selection biases; alternatively, one can incorporate selection effects into the model and directly predict the observed distributions. For completeness, we show and discuss the uncorrected MDFs in Appendix C.

One natural route for such an investigation is to take the photometrically inferred SFHs as a starting point, then derive the gas accretion history that produces this star formation for given assumptions about SFE. Fitting the evolutionary tracks will restrict the model parameters, and model variations that predict different enrichment versus time will predict different MDFs. As our exploratory results already suggest, chemical evolution constraints may make it possible to detect bursts or other variations in the star formation history. Joint modeling can test the need for more radical differences among the galaxies being considered, such as different IMFs, different Type Ia SNe populations, different AGB yields that could arise from systematic differences in stellar rotation, or differences in outflow physics such as preferential ejection of Type II SNe products relative to Type Ia SNe or AGB products.

7. Conclusions

We have presented the APOGEE chemical abundance patterns for five MW dwarf galaxies that span a range in mass and evolution environments. Our major conclusions are summarized as follows:

1. The chemical abundance patterns of these five dwarf galaxies show very different early SFEs, with GSE having had the strongest, followed by Sgr, then the MCs. Fnx plausibly had an early SFE similar to Sgr, but exhibits the lowest α-element abundance at [Fe/H] $= -1.2$, suggesting either a rapidly declining SFH or outflows that preferentially ejected Type II SNe products.

2. All dwarf galaxies except for GSE show chemical signs of extended star formation periods after the initial star formation epochs, with the LMC showing an increasing [α/Fe]–[Fe/H] abundance pattern, suggestive of a more intense starburst compared to the other galaxies. The lower [C/N] abundances of the metal-rich LMC stars suggest that they were formed at more recent times than the Sgr and MW low-α sequence stars at the same metallicity.

3. In median abundance trends, [X/Fe]–[Fe/H] and [X/Mg]–[Mg/H], Fnx is the strongest outlier among these five dwarfs, followed by GSE. Tracks for the MCs and Sgr are fairly similar except for low-metallicity [α/Fe] differences driven by SFE, and high-metallicity [α/Fe] differences driven by late star formation.

4. The C+N and Ce abundance patterns show that all galaxies had a greater contribution of AGB enrichment (relative to SNe contributions) to their evolution as compared to the MW high-α sequence, with Fnx showing the highest relative contributions and GSE showing the lowest at [Mg/H]<-0.8. However, the most metal-rich Sgr stars have the highest [Ce/Mg] abundances of any galaxy, and therefore have had the largest relative contribution of AGB stars to their enrichment.

5. The deficient [Al/Mg] abundances of the dwarf galaxies relative to the MW is plausibly a result of the overall lower metallicity Type II SNe that occurred in the dwarf galaxies as compared to the MW. Lower SFE may lead to a great "lag" between the metallicity of the ISM and the metallicity of the stars that enriched the ISM.

6. The deficient [Ni/Fe] abundances of the dwarf galaxies relative to both MW sequences combined with the deficient [Ni/Mg] relative to the MW low-α sequence can be explained if the production of Ni is dependent on the metallicity of the supernova progenitor.

We also use chemical evolution models to quantify some aspects of these chemical abundance patterns, finding that the SMC also experienced a recent enhancement of star formation, but this enhancement was weaker than the burst in the LMC by a factor of $\sim$2–3, and occurring 2–4 Gyr before the burst in the LMC. While not found to be coincident in the chemical evolution models, it is likely that the increased star formation epochs in both galaxies are the result of their mutual interactions.

From the models, we infer similar extended star formation events occurring in Sgr and Fnx some 3–6 Gyr ago, but these increases in star formation are small compared to the initial bursts. Future works that are able to properly account for selection biases can combine the photometric constraints on the SFHs with the chemical abundance patterns and MDFs to investigate further details of the SFHs of these galaxies (e.g., IMF variation, different AGB yields, etc.).

This comparative chemical abundance analysis highlights the role that galactic environment has in shaping a galaxy's chemical evolution. The most isolated galaxies, the MCs, had the weakest early SFE whereas Sgr and GSE enriched to much higher metallicities before Type Ia SNe began to significantly contribute to their chemical enrichment histories, likely due to their proximity to the MW. The less massive Sgr was able to continue forming stars upon beginning its merger with the MW whereas the evolution of GSE was likely cut short as it merged, perhaps because of its larger mass and more radial infall trajectory. The MCs evolved slowly in isolation, before interacting with each other at more recent times to drive up their star formation. Fnx was apparently not quenched when it fell into the MW environment, showing chemical signatures of a star formation history that was extended by either a merger or a pericenter passage around the MW.

This research made use of Astropy[43] a community-developed core Python package for Astronomy (Astropy Collaboration et al. 2013; Price-Whelan et al. 2018), SciPy (Virtanen et al. 2020), NumPy (Oliphant 2006), and Matplotlib (Hunter 2007).

Appendix A
Target Selection Supplemental

A.1. Magellanic Clouds

The Magellanic Clouds (MCs) have been targeted through multiple programs in APOGEE, some targeting the young, massive stars in the clouds, and others sampling the giant branches (see Zasowski et al. 2017; Nidever et al. 2020, and Santana et al. 2021 for all details). In this work we focus on

---

[43] http://www.astropy.org
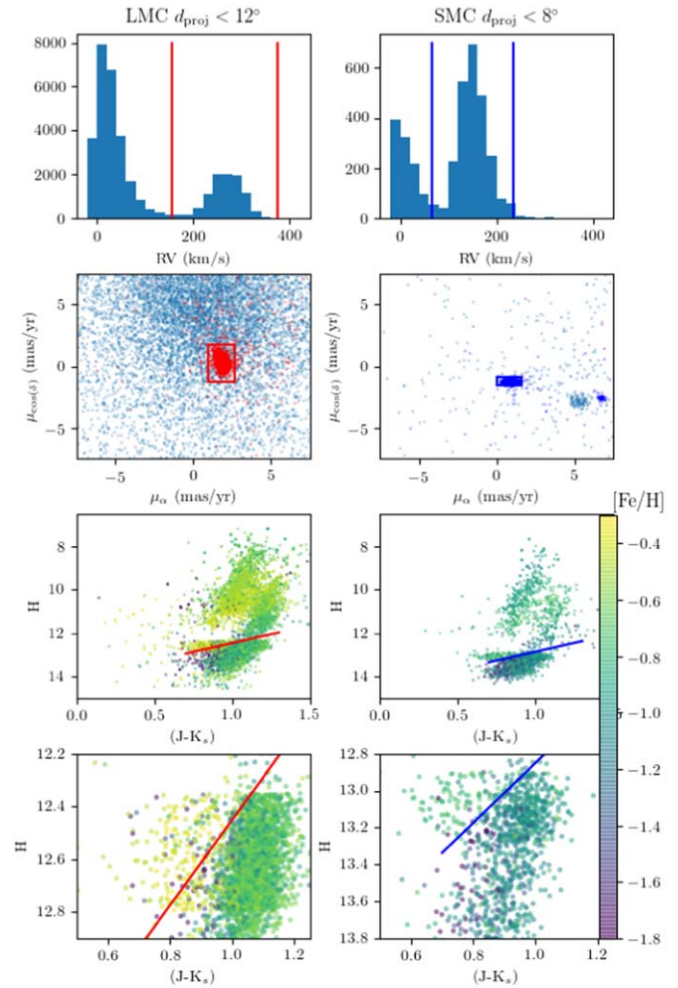
Figure 14. Top row: radial velocity distribution for stars that fall within 12° of the LMC center (left) and within 8° of the SMC center (right). Red and blue vertical lines mark the RVs that are $\pm3\sigma$ from the median RV of the LMC and SMC, respectively, used as cuts to select potential members. Second Row: the proper motion (PM) distributions for the LMC (left) and SMC (right) are colored by whether or not the stars fall within the RV cuts indicated in the top row. The red and blue boxes indicate the PM cuts applied to select the final MC members. Third Row: CMD for the stars that pass the RV and proper motion cuts. Stars are colored according to their APOGEE metallicity, as indicated by the color bar at the right. Red and blue lines indicate the photometric cuts used to remove obvious massive stars above the lines. Fourth Row: same as the third row, but zoomed in to illustrate where the RSGs are as bright as the tip of the RGB.

only the RGB stars for which we know APOGEE is able to derive reliable abundances (Jönsson et al. 2020). To select our MC sample, we first make spatial cuts, selecting all stars with a projected spherical distance within 12° and 8° of the centers of the LMC and SMC, respectively. The centers we adopt are (80°.893860, −69°.756126) for the LMC and (13°.18667, −72°.8286) for the SMC (α, δ). To remove obvious MW foreground contamination, we remove stars that are $\pm3\sigma$ from the median APOGEE-measured RV of each galaxy, as shown in the top row of Figure 14. We then make similar $\pm3\sigma$ cuts in each proper motion dimension from Gaia EDR3 to further remove MW contamination (second row of Figure 14).

As shown in the third row of Figure 14, these cuts result in a mixture of upper RGB stars, AGB stars, luminous AGB-O stars, RSG stars, massive blue main-sequence stars, and even
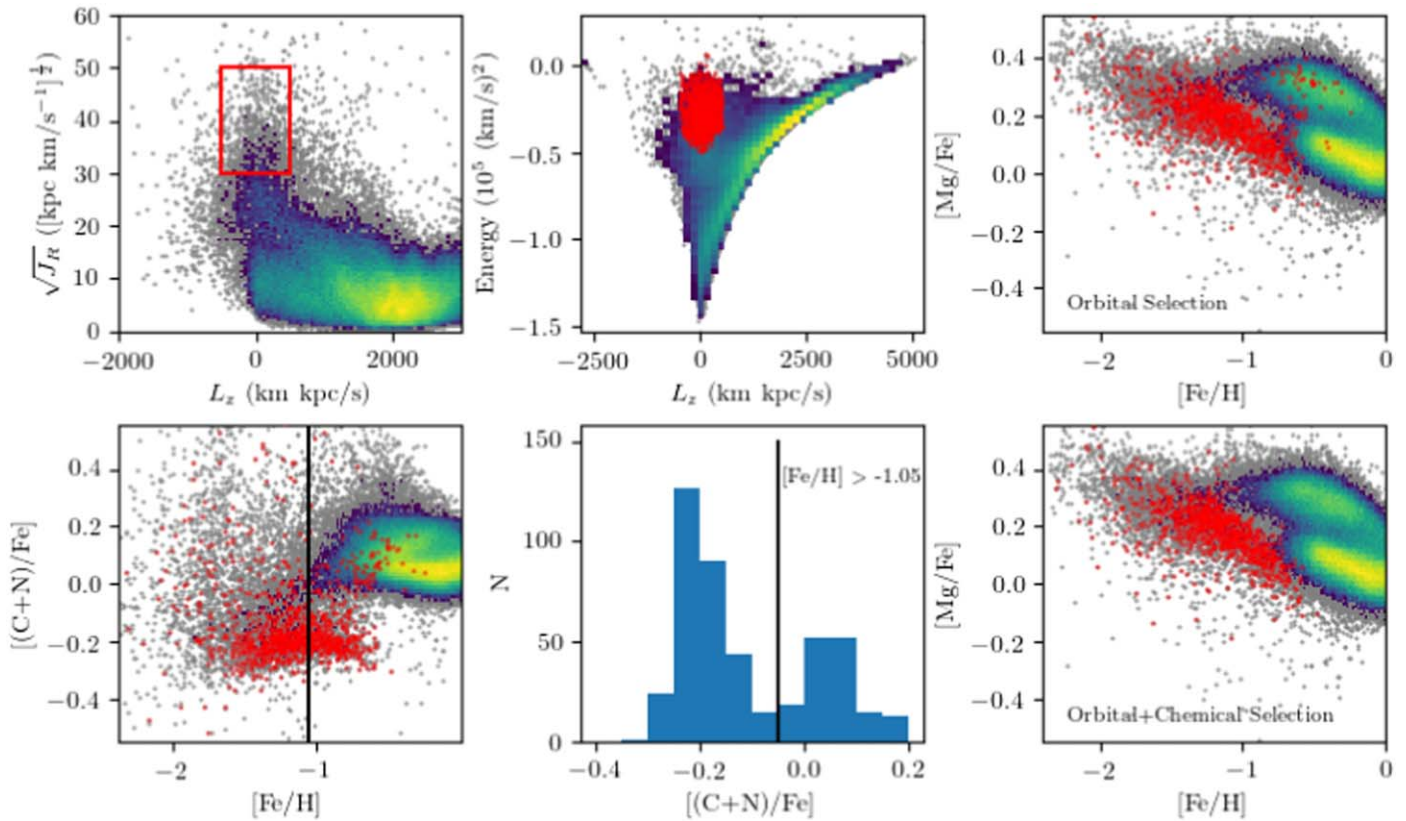
Figure 15. Plots that highlight the dynamical and chemical selections used to select GSE stars. Red points indicate GSE candidates and the "viridis" density map shows the MW parent sample from which they are selected. Upper left: L_z–$\sqrt{J_R}$ plane where the initial dynamical selection is made. Upper middle: Energy-Lz plane to highlight where these candidates lie. Upper right: [Mg/Fe]–[Fe/H] abundance distribution of the candidates. Bottom row: additional chemical cuts applied in [(C+N)/Fe]–[Fe/H] space to remove MW high-α disk contamination.

some objects around the instability strip. Because many of these types of objects are stars for which we do not know if the APOGEE abundance pipeline produces reliable results, we employ further cuts to select a sample of largely RGB stars. To do this, we first select stars below the tip of the RGB, as measured and defined by Hoyt et al. (2018):

$$H < (18.49 - 5.94 - 1.62 \times [(J - K_s) - 1.00]).$$

We make the cut 0.1 mag brighter to account for the varying depth of field across the galaxy. For the SMC, we use the same functional form, but account for the 0.5 difference in distance modulus. These selections are illustrated in the bottom four panels of Figure 14 as the red and blue lines for the LMC and SMC, respectively. We also exclude stars from both galaxies with $(J - K_s) > 1.3$ to avoid obvious carbon stars.

While these photometric cuts remove most of the massive evolved stars ($M \gtrsim 3 M_\odot$), the bottom-left panel of Figure 14 shows that some of the faintest RSGs in the LMC still make it into the photometric selection. We remove those by requiring that all stars with $(J - K_s) < 1.0$ and H<12.8 have [Fe/H]< -0.55. Note that this photometric selection means that our sample is biased against the youngest stars (Age $\lesssim 1$ Gyr).

A.2. GSE

To select the GSE sample, we start with the initial quality cuts described in Section 3 and remove stars belonging to known globular clusters, also avoiding regions of the sky containing the MCs. Specifically, we do not include stars that have a projected distance of 12° from the LMC and 8° from the

SMC. Then, considering only stars with [Fe/H]<0.0, we make kinematic cuts using the orbital angular momenta (L_z) and the square root of radial orbital action ($\sqrt{J_R}$), adopting the orbital properties computed with astroNN (Leung & Bovy 2019). We follow the work of Feuillet et al. (2020) and select stars with $|L_z| < 500$ km kpc s^{-1} and $\sqrt{J_R} = 30$–50 (kpc km s$^{-1})^{1/2}$, as shown by the red selection box in the upper-left panel of Figure 15. The upper-middle panel of Figure 15 shows where these stars lie in the Energy–L_z plane, which many other studies use to select GSE stars (e.g., Myeong et al. 2018; Horta et al. 2021; Naidu et al. 2021).

While this sample largely follows the expected [Mg/Fe]–[Fe/H] abundance pattern of GSE (e.g., Hayes et al. 2018; Haywood et al. 2018) that is shown in the top-right panel of Figure 15, there is clear contamination by the MW high-α "thick disk" stars. Therefore, we apply an additional [(C+N)/ Fe] cut for stars with [Fe/H] >-1.05, as demonstrated in the bottom row of Figure 15 and motivated by Hayes et al. (2018).

We find no obvious metallicity trend of our GSE members with L_z, suggesting we are not heavily biased in our sample. However, as mentioned in the text, should there be an undiscovered remnant of GSE that we are not observing here, then our comparison of GSE to the other galaxies is not complete.

A.3. Sgr

To select Sgr members, we follow a method similar to that described in Hayes et al. (2020). This work exploited the fact that the Sgr orbital plane is nearly perpendicular to the MW
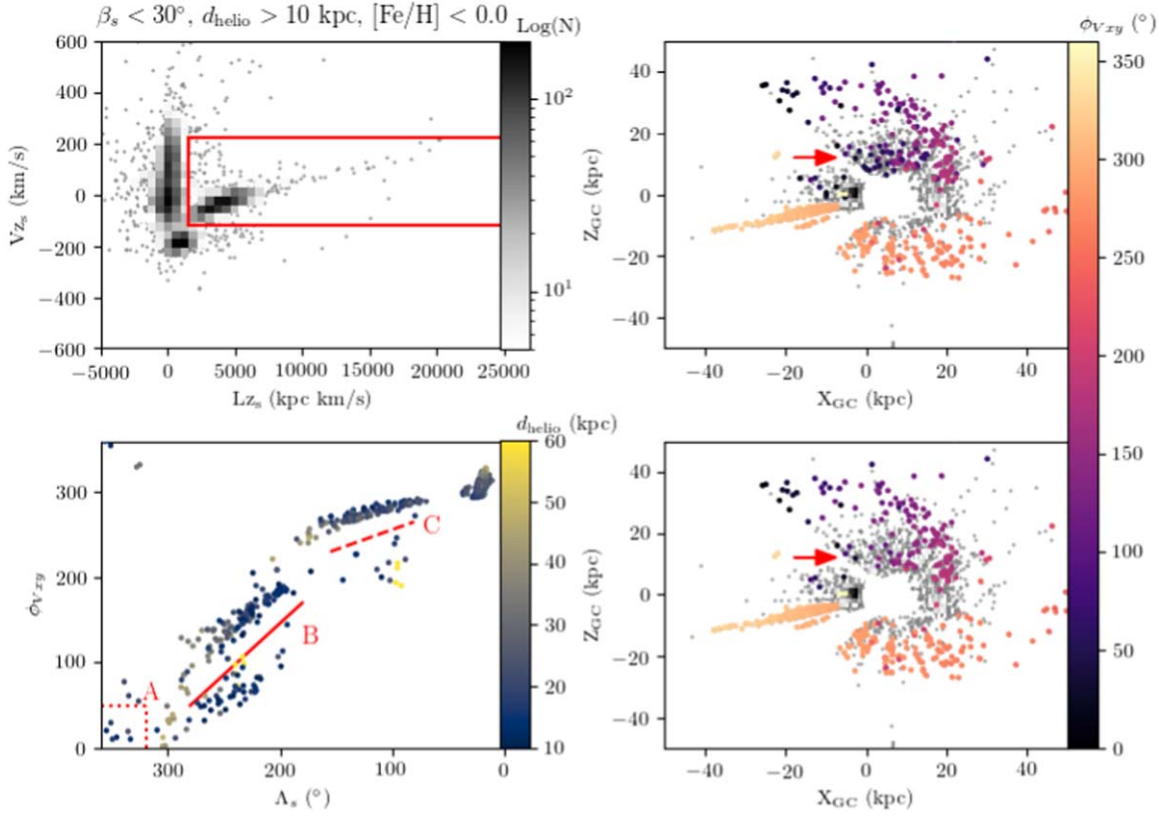
Figure 16. Top left: V_{zs}–L_{zs} plane showing the initial selection box, similar to what was done for Hayes et al. (2020). Top right: Galactic Z_{GC}–X_{GC} plane of all stars in the top-left panel, with the selected stars colored by $\phi_{\mathrm{vel,\,s}}$, the velocity direction in the V_{xs} and V_{ys} velocities. Bottom left: $\phi_{\mathrm{vel,\,s}}$ plotted as a function of longitude along the Sgr stream (Λ_s). The red A, B, and C regions indicate additional cuts placed on the sample as described in the text. Points are colored by heliocentric distance. Bottom right: same as the top-right panel with the additional contamination removed.

disk, making it easy to identify stars belonging to the Sgr main body and stream. As demonstrated in Hasselquist et al. (2019) and Hayes et al. (2020), the APOGEE survey has observed hundreds of Sgr stream stars strewn across much of the sky.

We first transform the APOGEE sample into the Sgr coordinate system described in Majewski et al. (2003). We then make initial cuts of:

1. $|\beta_s| < 30°$ to remove stars out of the Sgr orbital plane.
2. $d_{\mathrm{helio}} > 10$ kpc to remove stars that are too close to be Sgr stream members.
3. [Fe/H] < 0.0 to remove distant MW stars in and behind the bulge that are too metal-rich to be Sgr stream members.

From these cuts, we then analyze the resulting distribution in the V_{zs}–L_{zs} plane, which is the velocity in the z direction of the Sgr coordinate system plotted against the angular momenta in the Sgr system, shown in the upper-left panel of Figure 16. In principle, Sgr stars should have a V_{zs} velocity distribution centered around zero, and angular momenta consistent with the galactocentric distance of Sgr multiplied by its orbital velocity (i.e., $18\,\mathrm{kpc} \times 270\,\mathrm{km\,s^{-1}} \simeq 5000\,\mathrm{kpc\,km\,s^{-1}}$). In practice, the distance uncertainties result in a structure where the two quantities are correlated. Still, we use the density map to select stars with $L_{zs} > 1500\,\mathrm{kpc\,km\,s^{-1}}$, and $-120\,\mathrm{km\,s^{-1}} < V_{zs} < 220\,\mathrm{km\,s^{-1}}$.

These cuts result in a spatially coherent core and trailing/leading arm structures, shown in the upper-right panel of Figure 16. The points are colored by $\phi_{\mathrm{vel,s}}$, the direction of the velocity vector in the Sgr X and Y coordinates. Stars that are colored the same are stars that are moving in the same

direction. From this plot, we see some stars at $Z_{GC} \sim 18$ kpc and $-10\,\mathrm{kpc} < X_{GC} < 10$ kpc that are moving perpendicular to the stream stars found at slightly larger distances. These are likely halo contamination.

We remove these stars by looking more closely at the $\phi_{\mathrm{vel,s}}$ distribution as a function of Sgr longitude (Λ_s), as was also done in Hayes et al. (2020). In the lower-left panel of Figure 16 we define three regions (A, B, and C) where there is likely contamination, removed according to the following prescriptions:

1. A: Stars that are moving perpendicular to the expected stream at these latitudes, and in direction of the bulge, therefore likely to be MW contamination.
2. B: Stars that fall below the B line and have a distance < 30 kpc are likely not stream stars, as they are roughly the same distance as the stream, but moving perpendicularly. However, we do include the small handful of stars that fall below this line, but are at $d_{\mathrm{helio}} > 60$ kpc, as these could be more distant Sgr stream structures.
3. C: Stars that fall below the dashed C line, but are at $d_{\mathrm{helio}} > 50$ kpc.

Note that there are ~ 50 stars removed in total this way across the three regions, which constitutes only 5% of the sample. We have confirmed that the inclusion or removal of these stars does not change our results. The lower-right panel of Figure 16 shows the final spatial distribution of our Sgr sample. While our Sgr sample consists of stars across much of the sky, about two-thirds of our Sgr sample comes from the Sgr "main body" region, defined here as stars that are at a projected
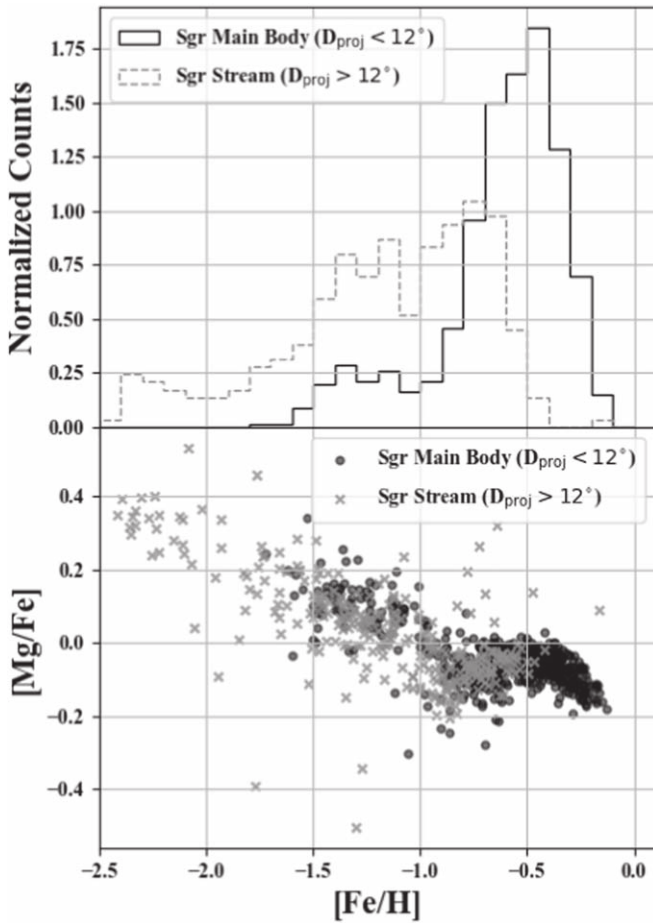
Figure 17. Top: metallicity distribution functions (MDFs) of the Sgr "main body" sample (solid black line) and the Sgr "stream" sample (dashed gray line). Bottom: [Mg/Fe]–[Fe/H] abundance plane with the Sgr main body sample plotted as black circles and the Sgr Stream sample plotted as gray Xs.

distance less than 12° from the center of Sgr. This main body region is shown in the inset figure of Figure 1. While we do find that the MDFs of the main body and stream regions differ substantially (see also Hayes et al. 2020), we show in the bottom panel of Figure 17 that the [Mg/Fe]–[Fe/H] abundance tracks for the two regions do not differ significantly where they overlap in [Fe/H].

A.4. Fnx

The Fnx selection is shown in Figure 18. APOGEE's Fnx field was specifically designed to target as many known members (based on previous radial velocity studies and Gaia proper motions) as possible, along with additional targets that were likely members by photometry only. We therefore clean the sample in a similar manner to the MCs (Section 3.1). First, we only include stars that belong to the "FORNAX" APOGEE field. We then remove stars $>\pm3\sigma$ from the median APOGEE RV, and then make a second selection on the Gaia EDR3 proper motions $(0.17<\mu_\alpha<0.60$ and $-0.71<\mu_\delta<-0.05)$, as shown in the top two panels of Figure 18. These RV and PM cuts only remove some 12 stars from the Fornax plate.

Because Fnx is a distant galaxy, the S/N of these stars are generally much lower than those in the other galaxies. This means that the Fnx chemical abundances are more uncertain, as
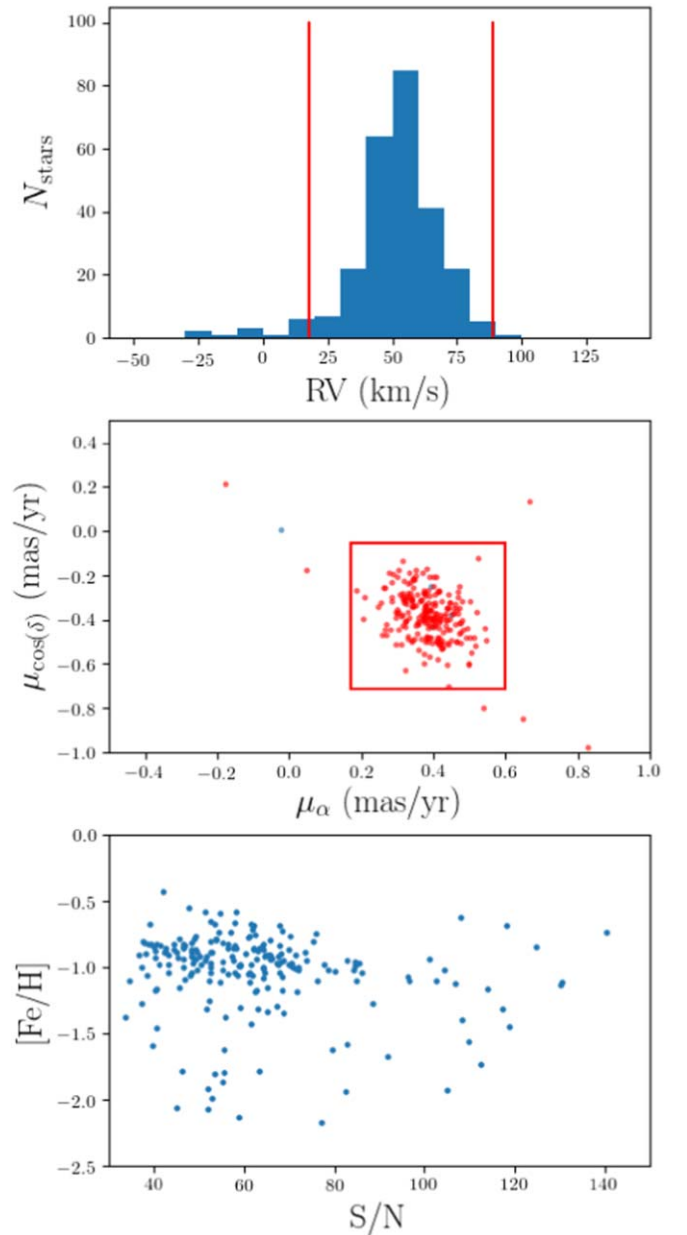
Figure 18. Top panel: radial velocity distribution of the APOGEE "FORNAX" field. The red vertical lines indicate $\pm3\sigma$ from the median radial velocity of the field. Middle panel: Gaia EDR3 proper motions of the same stars. A selection box of $\pm3\sigma$ in each direction of proper motion is used to remove potential contamination. Bottom panel: [Fe/H] vs. S/N for the sample.

indicated by the error bars in Section 4 and Figures 5 and 6. The lower panel of Figure 18 shows that our adopted lower S/N threshold of S/N >40, Section 3, does not obviously bias our Fnx result in any way, but the chemical abundance patterns overall for Fnx are more uncertain than the other galaxies.

Appendix B
Chemical Evolution Modeling Details

As mentioned in the text, we use the two chemical evolution models as a tool to quantify various features in the abundance patterns of these galaxies. There are many uncertainties and degeneracies associated with these models, especially when only fitting median abundance tracks rather than median

abundance tracks combined with abundance space density. In this section we provide more detail on some of the parameterization discussed in the text and explore the model parameter space to show how well constrained the parameters we derive actually are.

B.1. FlexCE Gas Inflow

One key change we make is that we use a different parameterization of gas inflow than used in the fiducial flexCE model of the MW (Andrews et al. 2017). We use a delayed-τ model for the inflow in each of our models, following the form:

$$\dot{M}_{\mathrm{in}} = \left(\frac{M_i}{\tau_i}\right)\left(\frac{t}{\tau_i}\right)e^{-t/\tau_i}$$

where $\dot{M}_{\mathrm{in}}$ is the gas mass inflow rate, M_i is the inflow mass scale (with M_i being the total mass that would be accreted as $t \to \infty$), τ_i is the inflow timescale, i.e., the time at which inflow is maximal (although note that this is not necessarily the time at which the star formation rate is maximal), and t is time.

This form of inflow is motivated by cosmological simulations (e.g., Simha et al. 2014) and is preferred over the fiducial, exponential model of inflow, because the delayed-τ model allows for a ramp-up of inflow (due to gas accretion earlier in the age of the universe), which later cuts off as a Galaxy stops growing through gas accretion and instead would grow through mergers. Additionally this parameterization of the gas inflow allows us to better reproduce the chemical abundance patterns seen in our sample of dwarf galaxies than when using the fiducial, exponential gas inflow because it allows for a slower enrichment at earlier times/lower metallicities that helps retain gas for later star formation and enrichment. In particular, while we do not fit the MDFs of these galaxies or the density of stars in the abundance planes, a slower initial enrichment may be needed to reproduce these quantities once they have been controlled for selection effects.

B.2. FlexCE Star Formation Efficiency

To turn this gas mass into stars, flexCE natively uses a constant SFE, such that the star formation rate (SFR) is defined as $\mathrm{SFR} = \mathrm{SFE} \times M_{gas}$. Here we modify flexCE to include a parameterization of SFE that is a time variable in order to be able to simulate a sustained burst of star formation as done in Nidever et al. (2020), which we employ to fit the chemical abundance profile of the LMC and SMC, as discussed below. Our formulation is to modify the constant SFE used by flexCE to add an increase in SFE following a Gaussian profile (for simplicity and so that the subsequent SFR change is continuous rather than having jumps or breaks). Formally, for our burst models, we use a time variable SFE that follows the form:

$$\mathrm{SFE}(t) = \mathrm{SFE} \times \left[1 + (F_b - 1)\exp\left(-0.5\left(\frac{(t - \tau_b)}{\sigma_b}\right)^2\right)\right]$$

where SFE is the constant base SFE, F_b is the burst strength, i.e., the peak factor of increase of SFE during the burst, τ_b is the time at which the peak increase in SFE occurs, and σ_b is the scale factor for the duration of the burst.

Of particular note on this parameterization of changing SFE, is that it is not an explicit parameterization of the SFR. Because the SFR is a function of gas mass and SFE, as the SFE rises, a galaxy can begin to exhaust its gas reservoir and the SFR may begin to fall, even if SFE continues to rise. Therefore changing the burst strength, timing, and duration may have somewhat unintuitive effects on the resulting SFR. For instance, each of these parameters can affect the timing of the SFR burst, because a stronger burst can exhaust gas more quickly and lead to an earlier peak in SFR, as could a longer burst, which may exhaust the model's gas before reaching peak SFE in addition to simply changing the timing of the peak SFE increase. Unfortunately, the chemical abundance patterns of galaxies are most sensitive to the SFR of the galaxy, not the underlying SFE, and there are degeneracies among these parameters when it comes to recreating a given SFH, hence we fix two of the three burst parameters when performing our chemical evolution modeling.

B.3. FlexCE Model Sensitivities

The flexCE modeling has four free parameters that we fit to the median abundance trends. While a detailed χ^2 mapping and deriving of actual SFH uncertainties is beyond the scope of this work, we show the effects of varying certain model parameters in Figure 19. The best-fit LMC model from above is shown in gold, and then models are generated holding all best-fit parameters fixed except for SFE (upper left), outflow strength (upper right), burst strength (lower left), and time of burst (lower right).

The upper-right panel of Figure 19 shows that while the model prefers a low outflow strength, the model with outflow set to 0 can still reproduce the data fairly well. The strength of the burst, shown in the lower-left panel, suggests that a stronger burst is not necessarily ruled out by our data, but does make predictions that the youngest LMC stars should have [Fe/H] =0.0. The lower-right panel shows that the time of burst is reasonably constrained, with an earlier or later burst, resulting in a track that does not match the data as well.

B.4. Lian Gas Inflow

The gas accretion is assumed to decline exponentially, $A(t) = A_{\mathrm{initial}}e^{-t/\tau_{\mathrm{acc}}}$, where A_{initial} is the initial gas accretion rate and τ_{acc} is the declining timescale. The major difference between this treatment of the gas inflow and the flexCE treatment is that the Lian model results in stars forming very quickly after the time starts, as much of the gas that will form stars is already present in the galaxy. The flexCE treatment results in a slight delay, as gas must be accreted to push up the star formation rate. This difference in gas inflow could explain some of the differences in SFHs between the two models. Future studies that are able to account for observational biases will be able to use the density of stars in this abundance plane as an additional constraint, perhaps better informing the gas inflow.

B.5. Lian Star Formation Efficiency

The star formation rate is determined from the gas mass following the form of the Kennicutt–Schmidt star formation law (SFL; Kennicutt 1998), assuming a Kroupa IMF (Kroupa 2001). The SFE is thus regulated by the coefficient of the SFL. We assume a constant coefficient (C_{initial}) unless a starburst event occurs. The starburst in the Lian model is characterized by an exponential increase in the coefficient of the SFL. In this way, the burst event is described by three
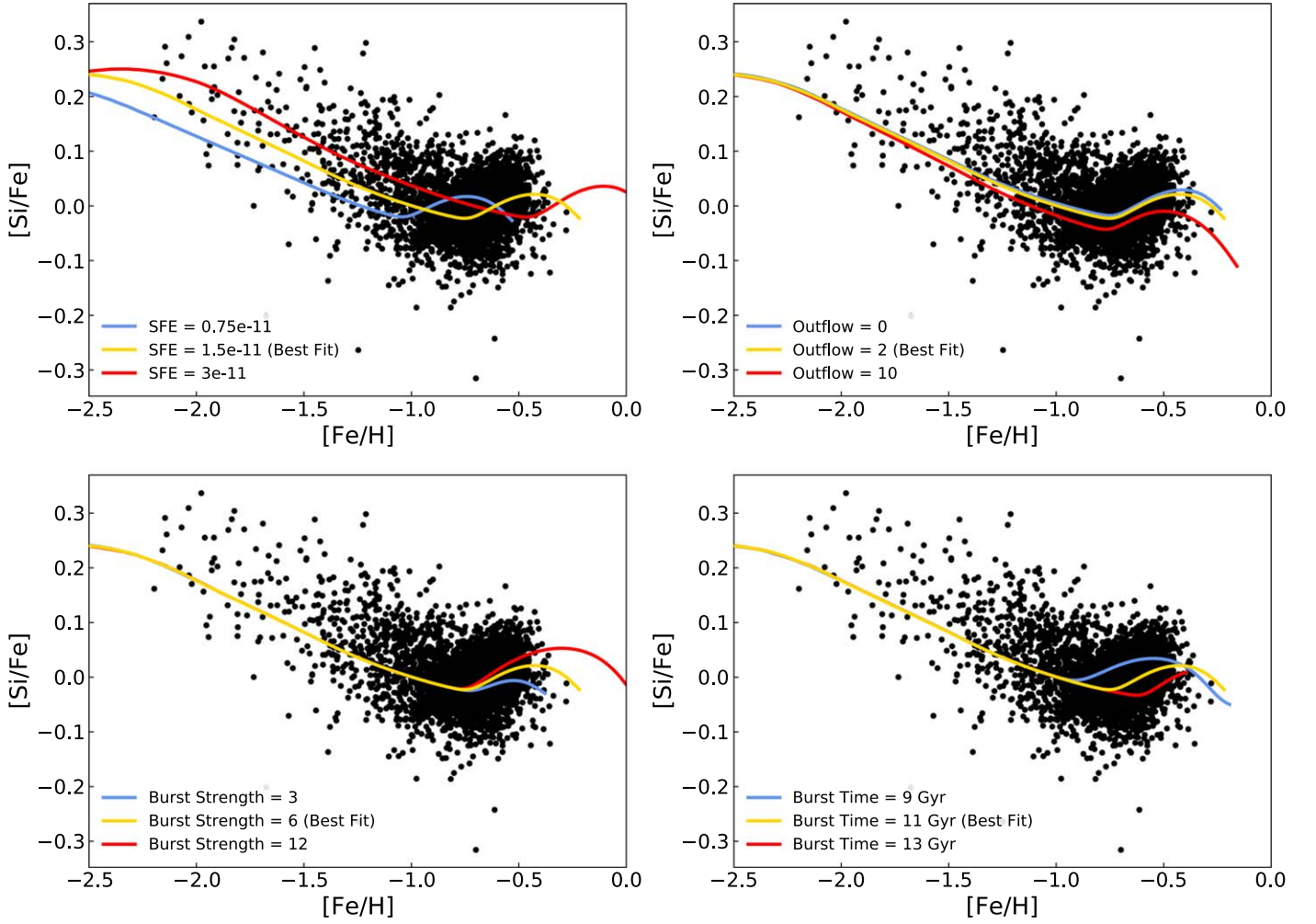
Figure 19. The [Si/Fe]–[Fe/H] abundance plane for the LMC stars fit with various flexCE models, where the gold model is the best-fit model presented in Section 5.3. Top left: initial SFE is varied. Top right: outflow parameter is varied. Bottom left: burst strength is varied. Bottom right: time of burst is varied.
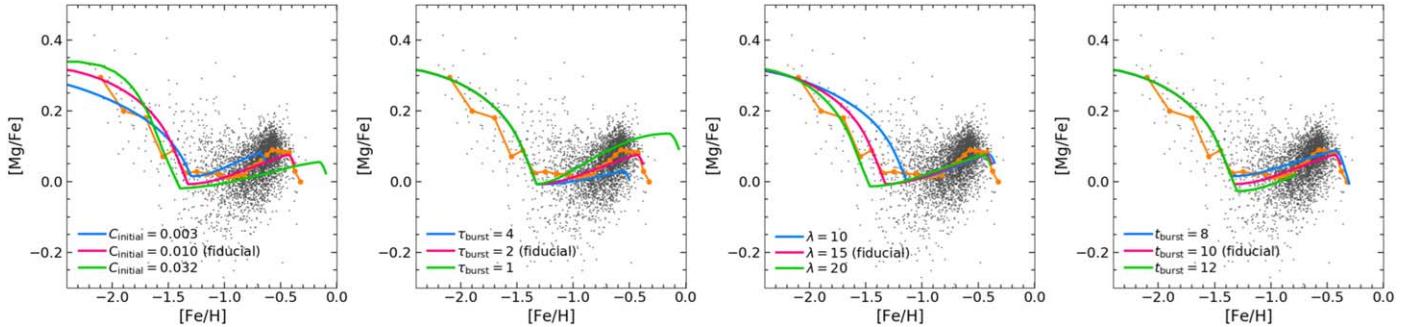
Figure 20. The [Mg/Fe]–[Fe/H] abundance plane for the LMC stars fit with various Lian models, where the pink model is the best-fit model presented in Section 5.3. Top left: initial SFE is varied. Top right: outflow parameter is varied. Bottom left: burst strength is varied. Bottom right: time of burst is varied.

parameters, the timescale (τ_{burst}), start time (t_{start}), and duration (Δt) of the SFE increase. After the burst, the coefficient of the SFL is set to decrease exponentially. Since this paper mainly focuses on the burst event, for simplicity, we fix this decreasing timescale to be 0.2 Gyr.

B.6. Lian Model Sensitivities

Figure 20 shows the results of adjusting various model parameters for the best-fit LMC model. Like the flexCE

parameterization discussed above, the Lian model is less sensitive to outflow strength (third panel), but is quite sensitive to the strength of the burst, with stronger or weaker bursts not matching the data (second panel).

Appendix C
Metallicity Distribution Functions

As discussed in Section 6.3, one could use the MDFs to constraint the chemical evolution models. In Figure 21 we
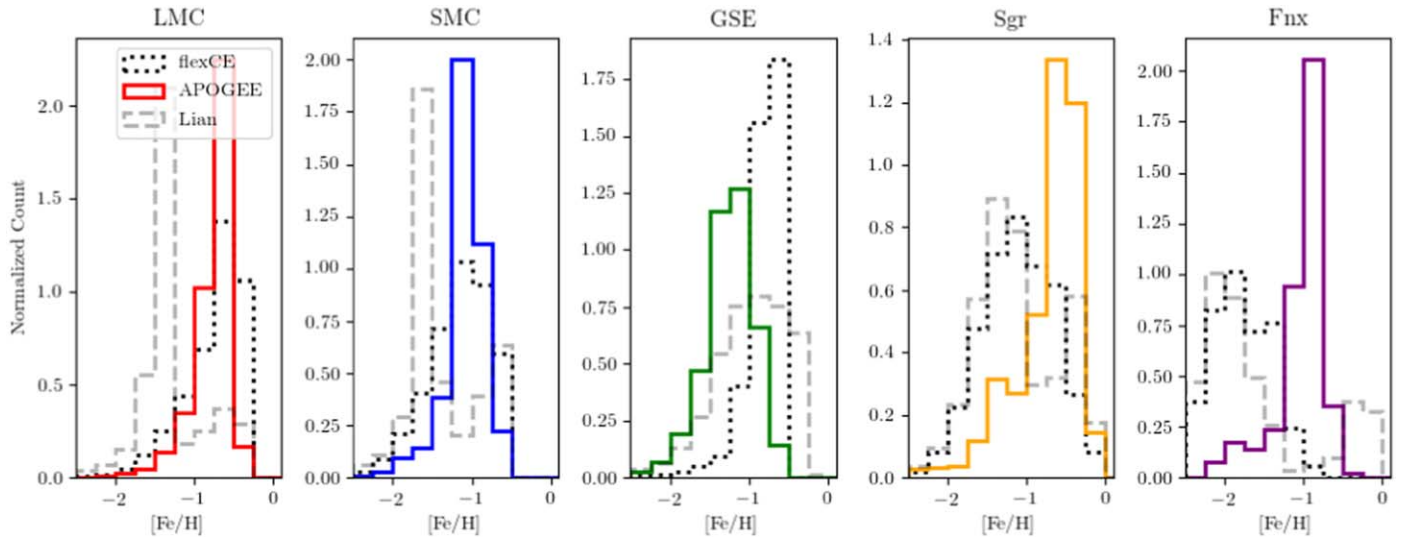
Figure 21. Metallicity distribution functions (MDF) of each of the dwarf galaxies along with predicted MDFs from the best-fit chemical evolution models. The flexCE models are denoted by dashed histograms and the Lian models are denoted by dotted histograms.

show the MDFs of the APOGEE data compared to MDFs predicted from the flexCE and Lian best-fit chemical evolution models to illustrate how such comparisons might inform future models. The flexCE-predicted MDFs agree reasonably well with the MC data, whereas the Lian models underpredict the number of metal-poor stars, implying that either the Lian models need to have stronger secondary star formation epochs for the clouds, or that we are biased against observing and/or deriving chemical abundances for the metal-poor stars in the APOGEE sample.

Neither models match well to Sgr or GSE, the two galaxies with the most complicated selection functions. Both models overpredict the number of metal-rich stars in GSE, most likely because they do not truncate star formation at late times. They underpredict the number of metal-rich stars in Sgr, although the Sgr model MDFs agree reasonably well with each other. For some of the APOGEE Sgr main body fields, stars were selected as previously known RV members from Frinchaboy et al. (2012), who specifically targeted M giants in the direction of Sgr. Therefore, it is expected that the APOGEE Sgr sample is somewhat biased against metal-poor stars, perhaps explaining this discrepancy. Both models under-predict the amount of metal-rich stars in Fnx, although the Lian model does predict a relatively larger fraction of metal-rich stars.

ORCID iDs

Sten Hasselquist ● https://orcid.org/0000-0001-5388-0994
Christian R. Hayes ● https://orcid.org/0000-0003-2969-2445
Jianhui Lian ● https://orcid.org/0000-0001-5258-1466
David H. Weinberg ● https://orcid.org/0000-0001-7775-7261
Gail Zasowski ● https://orcid.org/0000-0001-6761-9359
Rachael Beaton ● https://orcid.org/0000-0002-1691-8217
Diane K. Feuillet ● https://orcid.org/0000-0002-3101-5921
Carme Gallart ● https://orcid.org/0000-0001-6728-806X
Jon A. Holtzman ● https://orcid.org/0000-0002-9771-9622
Dante Minniti ● https://orcid.org/0000-0002-7064-099X
Ivan Lacerna ● https://orcid.org/0000-0002-7802-7356
Matthew Shetrone ● https://orcid.org/0000-0003-0509-2656
Henrik Jönsson ● https://orcid.org/0000-0002-4912-8609

Maria-Rosa L. Cioni ● https://orcid.org/0000-0002-6797-696X
Sean P. Fillingham ● https://orcid.org/0000-0002-8425-0351
Katia Cunha ● https://orcid.org/0000-0001-6476-0576
Ricardo Schiavon ● https://orcid.org/0000-0002-2244-0897
Borja Anguiano ● https://orcid.org/0000-0001-5261-4336
Timothy C. Beers ● https://orcid.org/0000-0003-4573-6233
Dmitry Bizyaev ● https://orcid.org/0000-0002-3601-133X
Joel R. Brownstein ● https://orcid.org/0000-0002-8725-1069
Roger E. Cohen ● https://orcid.org/0000-0002-2970-7435
Peter Frinchaboy ● https://orcid.org/0000-0002-0740-8346
D. A. García-Hernández ● https://orcid.org/0000-0002-1693-2721
Doug Geisler ● https://orcid.org/0000-0002-3900-8208
Steven R. Majewski ● https://orcid.org/0000-0003-2025-3147
David L. Nidever ● https://orcid.org/0000-0002-1793-3689
Christian Nitschelm ● https://orcid.org/0000-0003-4752-4365
Joshua Povick ● https://orcid.org/0000-0002-6553-7082
Adrian Price-Whelan ● https://orcid.org/0000-0003-0872-7098
Alexandre Roman-Lopes ● https://orcid.org/0000-0002-1379-4204
Jennifer Sobeck ● https://orcid.org/0000-0002-4989-0353
Guy Stringfellow ● https://orcid.org/0000-0003-1479-3059
Fiorenzo Vincenzo ● https://orcid.org/0000-0002-0743-9994

References

Akins, H. B., Christensen, C. R., Brooks, A. M., et al. 2021, ApJ, 909, 139
Alfaro-Cuello, M., Kacharov, N., Neumayer, N., et al. 2019, ApJ, 886, 57
Allende Prieto, C., Beers, T. C., Wilhelm, R., et al. 2006, AJ, 636, 804
Amorisco, N. C., & Evans, N. W. 2012, ApJL, 756, L2
Andrews, B. H., Weinberg, D. H., Schönrich, R., & Johnson, J. A. 2017, ApJ, 835, 224
Astropy Collaboration, Price-Whelan, A. M., Sipőcz, B. M., et al. 2018, AJ, 156, 123
Astropy Collaboration, Robitaille, T. P., Tollerud, E., et al. 2013, A&A, 558, A33
Beaton, R. L., Oelkers, R. J., Hayes, C. R., et al. 2021, arXiv:2108.11907
Bekki, K. 2014, MNRAS, 438, 444
Belokurov, V., Erkal, D., Evans, N. W., Koposov, S. E., & Deason, A. J. 2018, MNRAS, 478, 611

Belokurov, V., Zucker, D. B., Evans, N. W., et al. 2006, ApJL, 642, L137
Bensby, T., Feltzing, S., & Oey, M. S. 2014, A&A, 562, A71
Besla, G., Kallivayalil, N., Hernquist, L., et al. 2007, ApJ, 668, 949
Besla, G., Martínez-Delgado, D., van der Marel, R. P., et al. 2016, ApJ, 825, 20
Blanton, M. R., Bershady, M. A., Abolfathi, B., et al. 2017, AJ, 154, 28
Bonifacio, P., Hill, V., Molaro, P., et al. 2000, A&A, 359, 663
Bowen, I. S., & Vaughan, A. H. 1973, ApOpt, 12, 1430
Carlin, J. L., Sheffield, A. A., Cunha, K., & Smith, V. V. 2018, ApJL, 859, L10
Chieffi, A., & Limongi, M. 2004, ApJ, 608, 405
Chou, M.-Y., Majewski, S. R., Cunha, K., et al. 2007, ApJ, 670, 346
Coleman, M. G., Da Costa, G. S., Bland-Hawthorn, J., & Freeman, K. C. 2005, AJ, 129, 1443
Cunha, K., Smith, V. V., Hasselquist, S., et al. 2017, ApJ, 844, 145
de Boer, T. J. L., Belokurov, V., Beers, T. C., & Lee, Y. S. 2014, MNRAS, 443, 658
de Boer, T. J. L., Belokurov, V., & Koposov, S. 2015, MNRAS, 451, 3489
de Boer, T. J. L., Tolstoy, E., Hill, V., et al. 2012, A&A, 544, A73
Deason, A. J., Belokurov, V., Koposov, S. E., & Lancaster, L. 2018, ApJL, 862, L1
del Pino, A., Aparicio, A., & Hidalgo, S. L. 2015, MNRAS, 454, 3996
del Pino, A., Aparicio, A., Hidalgo, S. L., & Łokas, E. L. 2017, MNRAS, 465, 3708
Di Cintio, A., Mostoghiu, R., Knebe, A., & Navarro, J. 2021, MNRAS, 506, 531
Eisenstein, D. J., Weinberg, D. H., Agol, E., et al. 2011, AJ, 142, 72
Escala, I., Wetzel, A., Kirby, E. N., et al. 2018, MNRAS, 474, 2194
Fernández-Alvar, E., Carigi, L., Schuster, W. J., et al. 2018, ApJ, 852, 50
Fernández-Trincado, J. G., Beers, T. C., Minniti, D., et al. 2020, ApJL, 903, L17
Feuillet, D. K., Feltzing, S., Sahlholdt, C. L., & Casagrande, L. 2020, MNRAS, 497, 109
Fillingham, S. P., Cooper, M. C., Kelley, T., et al. 2019, arXiv:1906.04180
Fillingham, S. P., Cooper, M. C., Pace, A. B., et al. 2016, MNRAS, 463, 1916
Fillingham, S. P., Cooper, M. C., Wheeler, C., et al. 2015, MNRAS, 454, 2039
Frinchaboy, P. M., Majewski, S. R., Muñoz, R. R., et al. 2012, ApJ, 756, 74
Gallart, C., Bernard, E. J., Brook, C. B., et al. 2019, NatAs, 3, 932
Gallart, C., Monelli, M., Mayer, L., et al. 2015, ApJL, 811, L18
García Pérez, A. E., Allende Prieto, C., Holtzman, J. A., et al. 2016, AJ, 151, 144
Garro, E. R., Minniti, D., Gómez, M., & Alonso-García, J. 2021, A&A, 654, A23
Geha, M., Blanton, M. R., Yan, R., & Tinker, J. L. 2012, ApJ, 757, 85
Gratton, R. G., Sneden, C., Carretta, E., & Bragaglia, A. 2000, A&A, 354, 169
Grebel, E. K. 1999, in IAU Symp. 192, The Stellar Content of Local Group Galaxies, ed. P. Whitelock & R. Cannon (Cambridge: Cambridge Univ. Press), 17
Griffith, E., Weinberg, D. H., Johnson, J. A., et al. 2021, ApJ, 909, 77
Gunn, J. E., Siegmund, W. A., Mannery, E. J., et al. 2006, AJ, 131, 2332
Hansen, C. J., El-Souri, M., Monaco, L., et al. 2018, ApJ, 855, 83
Harris, J., & Zaritsky, D. 2004, AJ, 127, 1531
Harris, J., & Zaritsky, D. 2009, AJ, 138, 1243
Hasselquist, S., Carlin, J. L., Holtzman, J. A., et al. 2019, ApJ, 872, 58
Hasselquist, S., Shetrone, M., Smith, V., et al. 2017, ApJ, 845, 162
Hasselquist, S., Zasowski, G., Feuillet, D. K., et al. 2020, ApJ, 901, 109
Hawkins, K., Jofré, P., Masseron, T., & Gilmore, G. 2015, MNRAS, 453, 758
Hayes, C. R., Majewski, S. R., Hasselquist, S., et al. 2020, ApJ, 889, 63
Hayes, C. R., Majewski, S. R., Shetrone, M., et al. 2018, ApJ, 852, 49
Haywood, M., Di Matteo, P., Lehnert, M., et al. 2018, A&A, 618, A78
Helmi, A., Babusiaux, C., Koppelman, H. H., et al. 2018, Natur, 563, 85
Hendricks, B., Koch, A., Lanfranchi, G. A., et al. 2014, ApJ, 785, 102
Hester, J. A. 2006, ApJ, 647, 910
Hill, V., Skúladóttir, Á., Tolstoy, E., et al. 2019, A&A, 626, A15
Hodge, P. 1989, ARA&A, 27, 139
Hodge, P. W. 1971, ARA&A, 9, 35
Horta, D., Schiavon, R. P., Mackereth, J. T., et al. 2021, MNRAS, 500, 1385
Hoyt, T. J., Freedman, W. L., Madore, B. F., et al. 2018, ApJ, 858, 12
Hunter, J. D. 2007, CSE, 9, 90
Ibata, R., Irwin, M., Lewis, G. F., & Stolte, A. 2001, ApJL, 547, L133
Ibata, R., Lewis, G. F., Martin, N. F., Bellazzini, M., & Correnti, M. 2013, ApJL, 765, L15
Iben, I., Jr. 1964, ApJ, 140, 1631
Johnson, J. W., & Weinberg, D. H. 2020, MNRAS, 498, 1364
Jönsson, H., Allende Prieto, C., Holtzman, J. A., et al. 2018, AJ, 156, 126
Jönsson, H., Holtzman, J. A., Allende Prieto, C., et al. 2020, AJ, 160, 120
Kallivayalil, N., van der Marel, R. P., Besla, G., Anderson, J., & Alcock, C. 2013, ApJ, 764, 161

Karakas, A. I., & Lattanzio, J. C. 2014, PASA, 31, e030
Karakas, A. I., & Lugaro, M. 2016, ApJ, 825, 26
Kennicutt, R. C. J. 1998, ApJ, 498, 541
Kirby, E. N., Cohen, J. G., Guhathakurta, P., et al. 2013, ApJ, 779, 102
Kirby, E. N., Cohen, J. G., Smith, G. H., et al. 2011, ApJ, 727, 79
Kirby, E. N., Gilbert, K. M., Escala, I., et al. 2020, AJ, 159, 46
Kirby, E. N., Guhathakurta, P., Simon, J. D., et al. 2010, ApJS, 191, 352
Kirby, E. N., Xie, J. L., Guo, R., et al. 2019, ApJ, 881, 45
Kobayashi, C., Karakas, A. I., & Lugaro, M. 2020, ApJ, 900, 179
Kobayashi, C., Umeda, H., Nomoto, K., Tominaga, N., & Ohkubo, T. 2006, ApJ, 653, 1145
Kroupa, P. 2001, MNRAS, 322, 231
Lapenna, E., Mucciarelli, A., Origlia, L., & Ferraro, F. R. 2012, ApJ, 761, 33
Letarte, B., Hill, V., Tolstoy, E., et al. 2010, A&A, 523, A17
Leung, G. Y. C., Leaman, R., van de Ven, G., & Battaglia, G. 2020, MNRAS, 493, 320
Leung, H. W., & Bovy, J. 2019, MNRAS, 483, 3255
Lian, J., Thomas, D., Maraston, C., et al. 2018, MNRAS, 474, 1143
Lian, J., Thomas, D., Maraston, C., et al. 2020a, MNRAS, 497, 2371
Lian, J., Thomas, D., Maraston, C., et al. 2020b, MNRAS, 494, 2561
Lian, J., Zasowski, G., Hasselquist, S., et al. 2020c, MNRAS, 497, 3557
Mackereth, J. T., Schiavon, R. P., Pfeffer, J., et al. 2019, MNRAS, 482, 3426
Majewski, S. R., Schiavon, R. P., Frinchaboy, P. M., et al. 2017, AJ, 154, 94
Majewski, S. R., Skrutskie, M. F., Weinberg, M. D., & Ostheimer, J. C. 2003, ApJ, 599, 1082
Martig, M., Fouesneau, M., Rix, H.-W., et al. 2016, MNRAS, 456, 3655
Masseron, T., & Gilmore, G. 2015, MNRAS, 453, 1855
Mateo, M. L. 1998, ARA&A, 36, 435
McConnachie, A. W. 2012, AJ, 144, 4
McWilliam, A., Piro, A. L., Badenes, C., & Bravo, E. 2018, ApJ, 857, 97
McWilliam, A., Wallerstein, G., & Mottini, M. 2013, ApJ, 778, 149
Meschin, I., Gallart, C., Aparicio, A., et al. 2014, MNRAS, 438, 1067
Minniti, D., Ripepi, V., Fernández-Trincado, J. G., et al. 2021, A&A, 647, L4
Miyoshi, T., & Chiba, M. 2020, ApJ, 905, 109
Monteagudo, L., Gallart, C., Monelli, M., Bernard, E. J., & Stetson, P. B. 2018, MNRAS, 473, L16
Myeong, G. C., Evans, N. W., Belokurov, V., Sanders, J. L., & Koposov, S. E. 2018, ApJL, 863, L28
Naidu, R. P., Conroy, C., Bonaca, A., et al. 2021, arXiv:2103.03251
Ness, M., Hogg, D. W., Rix, H.-W., et al. 2016, ApJ, 823, 114
Nidever, D. L., Bovy, J., Bird, J. C., et al. 2014, ApJ, 796, 38
Nidever, D. L., Hasselquist, S., Hayes, C. R., et al. 2020, ApJ, 895, 88
Nidever, D. L., Holtzman, J. A., Allende Prieto, C., et al. 2015, AJ, 150, 173
Nidever, D. L., Majewski, S. R., Butler Burton, W., & Nigra, L. 2010, ApJ, 723, 1618
Nidever, D. L., Olsen, K., Choi, Y., et al. 2021, AJ, 161, 74
Nidever, D. L., Olsen, K., Walker, A. R., et al. 2017, AJ, 154, 199
Niederste-Ostholt, M., Belokurov, V., Evans, N. W., & Peñarrubia, J. 2010, ApJ, 712, 516
Nissen, P. E., & Schuster, W. J. 2010, A&A, 511, L10
Nomoto, K., Kobayashi, C., & Tominaga, N. 2013, ARA&A, 51, 457
Oliphant, T. 2006, NumPy: A guide to NumPy (USA: Trelgol Publishing)
Osorio, Y., Allende Prieto, C., Hubeny, I., Mészáros, S., & Shetrone, M. 2020, A&A, 637, A80
Pompéia, L., Hill, V., Spite, M., et al. 2008, A&A, 480, 379
Prantzos, N., Abia, C., Limongi, M., Chieffi, A., & Cristallo, S. 2018, MNRAS, 476, 3432
Reichert, M., Hansen, C. J., Hanke, M., et al. 2020, A&A, 641, A127
Revaz, Y., & Jablonka, P. 2018, A&A, 616, A96
Rocha, M., Peter, A. H. G., & Bullock, J. 2012, MNRAS, 425, 231
Rubele, S., Pastorelli, G., Girardi, L., et al. 2018, MNRAS, 478, 5017
Ruiz-Lara, T., Gallart, C., Beasley, M., et al. 2018, A&A, 617, A18
Ruiz-Lara, T., Gallart, C., Bernard, E. J., & Cassisi, S. 2020a, NatAs, 4, 965
Ruiz-Lara, T., Gallart, C., Monelli, M., et al. 2020b, A&A, 639, L3
Rusakov, V., Monelli, M., Gallart, C., et al. 2021, MNRAS, 502, 642
Rybizki, J., Just, A., & Rix, H.-W. 2017, A&A, 605, A59
Salaris, M., Pietrinferni, A., Piersimoni, A. M., & Cassisi, S. 2015, A&A, 583, A87
Santana, F. A., Beaton, R. L., Covey, K. R., et al. 2021, arXiv:2108.11908
Santana, F. A., Muñoz, R. R., de Boer, T. J. L., et al. 2016, ApJ, 829, 86
Sbordone, L., Bonifacio, P., Buonanno, R., et al. 2007, A&A, 465, 815
Schuster, W. J., Moreno, E., Nissen, P. E., & Pichardo, B. 2012, A&A, 538, A21
Seitenzahl, I. R., Ciaraldi-Schoolmann, F., Röpke, F. K., et al. 2013, MNRAS, 429, 1156
Shetrone, M., Tayar, J., Johnson, J. A., et al. 2019, ApJ, 872, 137

Shetrone, M., Venn, K. A., Tolstoy, E., et al. 2003, AJ, 125, 684
Shi, J., Wang, H., Mo, H., et al. 2020, ApJ, 893, 139
Siegel, M. H., Dotter, A., Majewski, S. R., et al. 2007, ApJL, 667, L57
Siegel, M. H., Majewski, S. R., Law, D. R., et al. 2011, ApJ, 743, 20
Simha, V., Weinberg, D. H., Conroy, C., et al. 2014, arXiv:1404.0402
Simon, J. D. 2019, ARA&A, 57, 375
Skúladóttir, Á., Hansen, C. J., Salvadori, S., & Choplin, A. 2019, A&A, 631, A171
Slater, C. T., & Bell, E. F. 2014, ApJ, 792, 141
Smith, V. V., Hinkle, K. H., Cunha, K., et al. 2002, AJ, 124, 3241
Soszynski, I., Poleski, R., Udalski, A., et al. 2008, AcA, 58, 163
Tinsley, B. M. 1979, ApJ, 229, 1046
Tolstoy, E., Hill, V., & Tosi, M. 2009, ARA&A, 47, 371
Tsujimoto, T., Nomoto, K., Yoshii, Y., et al. 1995, MNRAS, 277, 945
Van der Swaelmen, M., Hill, V., Primas, F., & Cole, A. A. 2013, A&A, 560, A44
Venn, K. A., Irwin, M., Shetrone, M. D., et al. 2004, AJ, 128, 1177
Vincenzo, F., Spitoni, E., Calura, F., et al. 2019, MNRAS, 487, L47

Vincenzo, F., Weinberg, D. H., Montalbán, J., et al. 2021, arXiv:2106.03912
Virtanen, P., Gommers, R., Oliphant, T. E., et al. 2020, NatMe, 17, 261
Walcher, C. J., Yates, R. M., Minchev, I., et al. 2016, A&A, 594, A61
Weinberg, D. H., Andrews, B. H., & Freudenburg, J. 2017, ApJ, 837, 183
Weinberg, D. H., Holtzman, J. A., Hasselquist, S., et al. 2019, ApJ, 874, 102
Weisz, D. R., Dolphin, A. E., Skillman, E. D., et al. 2013, MNRAS, 431, 364
Weisz, D. R., Dolphin, A. E., Skillman, E. D., et al. 2014, ApJ, 789, 147
Weisz, D. R., Dolphin, A. E., Skillman, E. D., et al. 2015, ApJ, 804, 136
Wetzel, A. R., Hopkins, P. F., Kim, J.-H., et al. 2016, ApJL, 827, L23
Wetzel, A. R., Tollerud, E. J., & Weisz, D. R. 2015, ApJL, 808, L27
Wheeler, C., Hopkins, P. F., Pace, A. B., et al. 2019, MNRAS, 490, 4447
Wilson, J. C., Hearty, F. R., Skrutskie, M. F., et al. 2019, PASP, 131, 055001
Woosley, S. E., & Weaver, T. A. 1995, ApJS, 101, 181
Zamora, O., García-Hernández, D. A., Allende Prieto, C., et al. 2015, AJ, 149, 181
Zasowski, G., Cohen, R. E., Chojnowski, S. D., et al. 2017, AJ, 154, 198
Zasowski, G., Johnson, J. A., Frinchaboy, P. M., et al. 2013, AJ, 146, 81